รายงานวิจัยฉบับสมบูรณ์

โครงการ การประดิษฐ์และสมบัติทางไฟฟ้าเคมีของโครงสร้างนาโนคอมโพสิท แอคทิเวทคาร์บอน/แมงกานิสเฟร์ไรต์สำหรับอุปกรณ์กักเก็บพลังงาน

โดย
สุกัญญา นิลม่วง

กันยายน 2561

สัญญาเลขที่ TRG5980001

รายงานวิจัยฉบับสมบูรณ์

โครงการ การประดิษฐ์และสมบัติทางไฟฟ้าเคมีของโครงสร้างนาโนคอมโพสิท แอคทิเวทคาร์บอน/แมงกานิสเฟร์ไรต์สำหรับอุปกรณ์กักเก็บพลังงาน

สุกัญญา นิลม่วง
มหาวิทยาลัยเทคโนโลยีราชมงคลอีสาน

สนับสนุนโดยสถาบันวิจัยแสงซินโครตรอน (องค์การมหาชน) และ
สำนักงานกองทุนสนับสนุนการวิจัย (สกว.)

Executive Summary

With the increasing demand of the world energy consumption, supercapacitors and lithium-ion batteries are the most two devices that have very competitive choices for applications due to their clean and promising power source. In field of energy storage electrode materials, high surface area, electrical conductivity, and surface functionalities are the parameters that play important roles for supported its electrochemical performance. Iron based oxides are one of electrode materials that have attracted the attention of many research groups due to their high specific capacitance and conductivity making them easier to construct high-energy and high-power densities. $MnFe_2O_4$ is an iron based oxides material that has received a great attention in various applications (magnetic storage device, electronic device, drug delivery, etc.). Typically, bare $MnFe_2O_4$ exhibits low conductivity making its impractical for use in stationary energy storage devices. Nevertheless, materials scientist tries to improve these material's properties with various method including synthesizing particle in nano-scale size and doping 2+ or 3+ valence state metal. Moreover, the literature revealed that, the making carbon-based composite is a way to enhance the electrical conductivity. The principal investigator has been reported the electrochemical properties of C/MFe_2O_4 (M=Co, Ni, Cu) composite nanofibers. The energy density for prepared C/MFe_2O_4 is improved after adding the MFe_2O_4 (M=Co, Ni, Cu) into CNF matrix. However, the specific capacitance for all C/MFe_2O_4 (<100 F/g) still low and needed to improve. Low capacitance of such samples is possibly due to of low surface area of non-activated CNF and low conductivity of ferrite nanoparticles.

Herein, two groups of composite materials: (i) carbon nanofibers (CNF) composite with manganese ferrite ($MnFe_2O_4$), and (ii) activated carbon nanofibers (ACNFs) composite with Cu doped manganese ferrite [$Cu_xMn_{1-x}Fe_2O_4$] nanostructures with a variety conditions are fabricated by electrospinning following by carbonization and activation process. Activated carbon is made by charring a precursor, then oxidizing the charred body using carbon dioxide to create nanoscopic pores. ACNFs are used due to their high specific surface area, possess EDLC, provided high power density and long life cycle, while $MnFe_2O_4$ and $Cu_xMn_{1-x}Fe_2O_4$ are metal oxide that possess pseudocapacitance. Therefore, composite these metal oxides into carbon fiber matrix is a promising approach to develop and optimize the structures and properties of electrode material for enhancing their performance for supercapacitors. Moreover, the adding activation process to improve surface area of CNF and the doping of copper metal into manganese to increase the electrical conductivity are also the important routes to improve the electrochemical cell performance in our work.

บทคัดย่อ

รหัสโครงการ: TRG5980001
ชื่อโครงการ: การประดิษฐ์และสมบัติทางไฟฟ้าเคมีของโครงสร้างนาโนคอมโพสิทแอคทิเวทคาร์บอน/แมงกานิสเฟร์ไรต์สำหรับอุปกรณ์กักเก็บพลังงาน
ชื่อนักวิจัย: สุกัญญา นิลม่วง
มหาวิทยาลัยเทคโนโลยีราชมงคลอีสาน
E-mail Address: sukanya.ni@rmuti.ac.th
ระยะเวลาโครงการ : 2 ปี

ในงานวิจัยนี้ได้ทำการประดิษฐ์ ศึกษาคุณลักษณะ และสมบัติทางไฟฟ้าเคมีของเส้นใยนาโนคาร์บอนคอมโพสิตกับอนุภาคเฟร์ไรต์ จำนวน 2 กลุ่มคือ (1) เส้นใยนาโนคาร์บอนคอมโพสิตกับแมงกานีสเฟร์ไรต์ (CNF/$MnFe_2O_4$) และ (2) เส้นใยคาร์บอนรูพรุนคอมโพสิตกับคอปเปอร์แมงกานีสเฟร์ไรต์ (ACNF/$Cu_xMn_{1-x}Fe_2O_4$ โดยกระบวนการประดิษฐ์ใช้เทคนิคการปั่นเส้นใยด้วยไฟฟ้าสถิตร่วมกับการคาร์บอไนเซชัน ในสารกลุ่มที่ 1 และเพิ่มกระบวนการแอคทิเวชันเพื่อให้เกิดรูพรุนในสารกลุ่มที่ 2 สารตัวอย่างที่ได้ถูกนำไปศึกษาคุณลักษณะโดยเทคนิค XRD, FE-SEM, BET, TGA, XPS และ XAS สมบัติทางไฟฟ้าเคมีถูกศึกษาโดยใช้เทคนิค CV, GCD และ EIS ผลการศึกษาพบว่า สำหรับสารตัวอย่างกลุ่มที่ 1 เมื่อทำการเปลี่ยนอุณหภูมิการคาร์บอไนเซชันตั้งแต่ 500 ไปจนถึง 700 องศาเซลเซียส $MnFe_2O_4$ มีโครงสร้างเป็น อินเวอร์สสปริเนลเฟร์ไรต์ โดยเหล็กและแมงกานีสแสดงเลขออกซิเดชัน 3^+ และ 2^+ ตามลำดับ ขนาดของผลึก พื้นที่ผิว ปริมาณคงเหลือของ $MnFe_2O_4$ และอัตราส่วนของ Mn ions ใน tetrahedral site เพิ่มขึ้นตามอุณหภูมิคาร์บอไนเซชัน โดยตัวอย่างที่มีพื้นที่ผิวสูงที่สุด มีขนาดของผลึกใหญ่ที่สุด มีปริมาณคงเหลือของ $MnFe_2O_4$ มากสุด และมีสัดส่วนของ Mn^{2+} ใน tetrahedral site มากที่สุด มีการกักเก็บประจุได้มากที่สุด จากการทดลองพบว่า ค่าการความจุเฉพาะสูงสุดจากเทคนิค CV คือ 345 Fg^{-1} ที่อัตราการแสกน 2 mVs^{-1} และค่าสูงสุดจากเทคนิค GCD คือ 291.87 Fg^{-1} ที่ความหนาแน่นกระแส 5 Ag^{-1} สำหรับสารตัวอย่างในกลุ่มที่สอง ได้ศึกษาพฤติกรรมทางไฟฟ้าเคมีโดยทำการเปลี่ยนแปลงปริมาณของ ‘x’ (0.0, 0.2, 0.4, 0.6, 0.8) พบว่าค่าความจุเฉพาะสูงสุดจากเทคนิค CV คือ 384 F/g ที่ 2 mV/s และจากเทคนิค GCD คือ 314 F/g ที่ 2 A/g ถูกพบในขั้วไฟฟ้าเคมีที่ $x = 0.2$ ส่วนค่ารองลงมาคือ 235 F/g ที่ 2 mV/s จากเทคนิค CV และ 172 F/g ที่ 2 A/g จากเทคนิค GCD ถูกพบในขั้วไฟฟ้า $x = 0.8$. โดยมีค่าความหนาแน่นพลังงานที่สอดคล้องกันคือ 74 และ 41 Wh/kg ตามลำดับ นอกจากนี้ยังพบว่า ความเสถียรของตัวอย่างที่เตรียมได้ขึ้นอย่างมากกับปริมาณของคาร์บอน ในขณะที่ค่าความจุเฉพาะเพิ่มสูงขึ้นในตัวอย่างที่มีปริมาณคาร์บอนกับคอปเปอร์แมงกานีสเฟร์ไรต์ใกล้เคียงกัน น่าจะเนื่องจาก synergetic effect ระหว่าง $CuMnFe_2O_4$ และ ACNF พฤติกรรมทางไฟฟ้าเคมีของสารตัวอย่างทั้งสองกลุ่มที่เตรียมได้ดังกล่าว บ่งชี้ถึงศักยภาพในการนำวัสดุคอมโพสิตระหว่างเส้นใยนาโนคาร์บอนกับแมงกานีสเฟไรต์ไปประยุกต์ใช้ทำเป็นวัสดุขั้วสำหรับอุปกรณ์กักเก็บพลังงาน

คำหลัก : เส้นใยนาโนคาร์บอนคอมโพสิต แมงกานิสเฟไรต์ คอปเปอร์แมงกานีสเฟร์ไรต์ อิเล็กโตรสปินนิง ตัวเก็บประจุไฟฟ้ายิ่งยวด

Abstract

Project Code: TRG5980001

Project Title: Fabrication and electrochemical properties of activated CNF/$MnFe_2O_4$ composite nanostructures for energy storage devices

Investigator: Sukanya Nilmoung
Rajamangala University of Technology Isan

E-mail Address: sukanya.ni@rmuti.ac.th

Project Period: 2 years

This work reports the fabrication, characterization and electrochemical properties of two groups of materials (i) carbon nanofibers composited with manganese ferrite (CNF/$MnFe_2O_4$) and (ii) activated carbon nanofbers composited with copper manganese ferrite (ACNF/$Cu_xMn_{1-x}Fe_2O_4$: x = 0.0, 0.2, 0.4, 0.6, 0.8) nanostructures. The obtained samples were characterized by means of X-ray diffraction (XRD), field emission scanning electron microscopy (FE-SEM), Brunauer-Emmett-Teller analyzer (BET), thermal gravimetric analysis (TGA), X-ray photoemission spectroscopy (XPS) and X-ray absorption spectroscopy (XAS). The electrochemical properties were investigated using cyclic voltammetry (CV), galvanostatic charge-discharge (GCD), and electrochemical impedance spectroscopy (EIS). For the first group of prepared materials: the local structure of $MnFe_2O_4$ was found to be partial inverted spinel ferrite with oxidation state of Fe^{3+} and Mn^{2+} after increased the carbonization temperature from 500 to 700. The crystallite size, surface area, residual content of $MnFe_2O_4$, and fraction of Mn ions in tetrahedral site increased with increasing of carbonization temperature. The benefits of sample with maximum surface area, largest crystallite size, highest residual content of $MnFe_2O_4$ and high fraction of Mn^{2+} in tetrahedral site leading to enhanced energy storage. The maximum specific capacitance of 345 Fg^{-1} at 2 mVs^{-1} (using CV) and 291.87 Fg^{-1} at 5 Ag^{-1} (using GCD) were observed. For the second groups of prepared samples, the supercapacitive behavior of the electrodes is observed at various values of ‘x’ (0.0, 0.2, 0.4, 0.6, 0.8). The highest specific capacitance of 384 F/g at 2 mV/s using CV and 314 F/g at 2 A/g using GCD are obtained for the x = 0.2 electrode. The second one of 235 F/g at 2 mV/s using CV and 172 F/g at 2 A/g using GCD are observed for x = 0.8 electrode. The corresponding energy densities are 74 and 41 Wh/kg, respectively. It is observed that the cyclic stability of the prepared samples strongly depend on the amount of carbon, while the specific capacitance was enhanced by the sample with nearly proportional amount between carbon and $CuMnFe_2O_4$. Such results may arise from the synergetic effect between $CuMnFe_2O_4$ and ACNF. The fascinating electrochemical properties of all prepared sample make their potential a candidate for high performance energy storage devices.

Keywords: carbon nanofibers composite, manganese ferrite, copper-manganese ferrite, electrospinning, superconductor

1. Introduction

With the increasing demand of the world energy consumption, supercapacitor and lithium-ion batteries are the most two devices that have very competitive choices for applications due to their clean and promising power source. Lithium ion batteries have become the ubiquitous power sources for portable devices, electronic device and upcoming electric vehicles, because of their excellent energy densities [1-2]. Supercapacitors are suitable device for electric vehicles, digital communication devices, electrical tools due to their high specific power and long cycle life [3-4]. Typically, supercapacitors have higher energy density than conventional capacitors and higher power density than batteries [5-6]. Normally, the energy density of these devices is proportional to its capacitance, while the power density is depends on the internal resistance. Therefore, developing electrode materials with high capacitance and/or high conductivity should be the key approaches in energy storage device research and development. According to the charge storage mechanism, supercapacitors are classified into electrical double layer capacitors (EDLCs) and pseudo-capacitors. Typically, a pseudo-capacitors (based on metal oxide or conducting polymers) exhibit greater capacitance value than EDLCs (based on carbon materials) due to their charge storage occurs through surface redox reaction, while EDLCs store energy by accumulating electrostatic charge at the electrode/electrolyte interface.

In field of energy storage electrode materials, high surface area, porosity, electrical conductivity, surface functionalities etc., are the parameters that play important roles for supported its electrochemical performance. To date, a variety of transition metal oxides such as RuO_2 [7], MnO_2 [8], NiO [9], CuO [10], Fe_3O_4 [11] have been used as electrode materials due to their pseudo-capacitances. Spinel ferrite material (MFe_2O_4: M is divalent transition metal) is metal oxide with spinel structure that also have been studied extensively. The unit cell of MFe_2O_4 is formed by 56 atoms with the 32 oxygen anions distributed in a cubic close packed structure. The 24 cations occupying 8 of the 64 available tetrahedral sites and 16 of the 32 available octahedral sites [12]. Iron based oxides are one of electrode materials that have attracted the attention of many research groups due to their high specific capacitance and conductivity making them easier to construct high-energy and high-power densities [13-14]. $MnFe_2O_4$ is an iron based oxides material with a cubic spinel ferrite structure that has received a great attention in various applications (magnetic storage device [15], electronic device [16], drug delivery [17], etc.). A variety of nanostructures (nanorods/nanowires [18], nanosphere [19], nanotube [20], etc.) have been successfully synthesized by using various synthetic techniques, such as ball milling [21-22] sol-gel method [23], hydrothermal [24], co-precipitation [25], electrochemical synthesis [26], etc. $MnFe_2O_4$ is a material that stability in electrochemical [27] and the favors electrochemical reactions very positively [28]. However, bare $MnFe_2O_4$ exhibits low conductivity making its impractical for use in stationary energy storage devices and electric vehicles. Nevertheless, materials scientist tries to improve these material's properties with various method including synthesizing particle in nano-scale size, doping 2+ or 3+ valence state metal or coating the particle surface with carbon materials. Moreover, the literature revealed that, the making carbon-based composite is a way to enhance the electrical conductivity [13].

2. Objectives

The aim of this research is to contribute to the collective knowledge in the fabrication, characterization, and electrochemical properties of carbon nanofibers composite with manganese ferrite nanostructures for application in supercapacitors. In overall, the major scientific and technical objectives of the research involve

2.1 To fabricate carbon nanofibers composite with manganese ferrite by electrospinning followed by heat treatment process. Two groups of composite materials were prepared including (i) carbon nanofibers composited with manganese ferrite (CNF/$MnFe_2O_4$) and (ii) activated carbon nanofbers composited with copper manganese ferrite (ACNF/$Cu_xMn_{1-x}Fe_2O_4$: x = 0.0, 0.2, 0.4, 0.6, 0.8) nanostructures

2.2 To characterize the effect of carbonization temperature (for CNF/$MnFe_2O_4$) and the composition of materials (for ACNF/$Cu_xMn_{1-x}Fe_2O_4$: x = 0.0, 0.2, 0.4, 0.6, 0.8) on the morphologies, crystal structure, local structure and surface area of prepared samples

2.3 To study the electrochemical properties of CNF/$MnFe_2O_4$ and ACNF/$Cu_xMn_{1-x}Fe_2O_4$ (x = 0.0, 0.2, 0.4, 0.6, 0.8) composite nanostructures

3. Methodology

3.1 materials

In this study, Polyacrylonitrile (C_3H_3N), N, N-dimethylformamide anhydrous (C_3H_7NO), Iron (III) nitrate enneahydrate ($Fe(NO_3)_2 \bullet 9H_2O$), Manganese(II) nitrate hydrate ($Mn(NO_3)_2 \bullet xH_2O$), copper (II) nitrate trihydrate ($Cu(NO_3)_2 \bullet 3H_2O$), and Aluminum nitrate nonahydrate ($Al(NO_3)_3 \bullet 9H_2O$) were used as the starting materials. All of analytical grade and used without further purification.

3.2 Synthesis

3.2.1 Synthesis of CNF/$MnFe_2O_4$ composite nanostructure

The precursor solution for electrospun PAN/$MnFe_2O_4$ were prepared by using mixed of polymer and metal sources solution. The polymer source was prepared by mixing of PAN in DMF solvent, whereas the metal source was obtained by mixing manganese nitrate with Iron nitrate in DMF solvent (the molar ratio of Mn: Fe was fixed as 1:2). PAN was used as matrix for the synthesis of metal oxide nanoparticle due to it can prevent of agglomeration of the nanoparticles, control of the growth of the nanoparticles, and produce the uniform distribution of nanoparticles.The polymer source was stirred at room temperature followed by ultrasonication, while the metal source was stirred at room temperature. After that, both solutions will be mixed together under magnetic stirring to obtain homogeneously distributed solution. No other chemicals were added to the solution. The obtained PAN/$MnFe_2O_4$ composite solution was electrospun in an ambient air atmosphere at room temperature using our home-made electrospinning system under an applied voltage of 10 kV, a feeding rate of 0.35 ml/h, a distance from syringe nozzle to collector of 10 cm, and drum rotating at 500 rpm. The obtained electrospun nanofibers will be dried at 60 ^{o}C for 48 h before stabilization and carbonization, respectively. Stabilization is the process used to convert the linear polymer into a ladder structure and crosslink the chain molecules, thus can prevent the fibers from melting or fusing during higher temperature heat treatment. This step was carried out at 250 °C for 4 h in air atmosphere which breaks many of the hydrogen bonds and oxidizes the material. To obtain the CNF/$MnFe_2O_4$ composite nanostructures, the stabilized samples were carbonized at 500, 600, 700 and 800 ^{o}C under flowing of mixed air and argon atmosphere. Carbonization is a heat treatment process to remove non-carbon elements. During carbonization, PAN is converted into carbon, while the binary metal precursors were decomposed to $MnFe_2O_4$. Note that a slightly air adding due to the oxidation with air oxygen is needed to form those metal oxides. The final products are designated as CNF/$MnFe_2O_4$_500, 600, 700, and 800^{o}C, respectively.

3.2.2 Synthesis of ACNF/$Cu_xMn_{1-x}Fe_2O_4$ composite nanostructures

The precursor solution for electrospun ACNF/$Cu_xMn_{1-x}Fe_2O_4$ composite nanostructures were prepared by using a mixed homogenous solution of polymer and metal sources. The polymer source was prepared by dissolving PAN 1.8 g in 25 ml of DMF solvent, whereas the metal source was obtained by mixing Cu, Mn and Fe nitrates (with molar ratio of x : 1-x : 2, x = 0.0, 0.2, 0.4, 0.6 and 0.8) in DMF solvent. Both sources were mixed thoroughly with magnetic stirrer for 2h, followed by sonication for 1h. The precursor solution was turned to nanofibers by using our home-made electrospinning system under an applied voltage of 10 kV, a feeding rate of 0.35 ml/h, a distance from syringe nozzle to collector of 10 cm, and drum rotating at 500 rpm. After dried at 60 ^{o}C for 48 h, the as-spun fibers were stabilized at 250 ^{o}C for 4 h in air atmosphere to form a ladder structure by the dehydrogenation and cyclization process [29]. To get the CNF/$CuMnFe_2O_4$ composite nanostructures, the stabilized samples were carbonized at 750 ^{o}C for 1 h under flowing of mixed air and argon atmosphere (30:300 ml/min). In this process, the heteroatoms like nitrogen are eliminated and the aromatic structure grows [30]. After that, ACNF/$CuMnFe_2O_4$ samples were obtained via activation process at 800 ^{o}C for 30 minutes under CO_2 atmosphere (160 ml/min). In this process CO_2 reacts with carbon according to $C+CO_2 \longrightarrow 2CO$, remove some carbon from the fibers, develops porosity and thus enlarge surface area. The final products are designated as ACNF/$Cu_xMn_{1-x}Fe_2O_4$ (x=0.0, 0.2, 0.4, 0.6, and 0.8), respectively.

3.3 Material characterization

To understand the main features of the prepared samples, explaining their properties and determining areas for their potential applications, several characterization techniques will be used as followed: The structural elucidation was carried out using X-ray diffraction technique (XRD, Bruker D2 advance) with a Cu-Kα radiation source (λ = 0.15406 nm). The morphologies were observed by field emission scanning electron microscopy (FE-SEM, Carl Zeiss, Auriga). The oxidation state of metal atoms was conducted at X-ray photoemission spectroscopy and X-ray absorption spectroscopy station (XPS and XAS, BL5.2, 1.2 GeV, bending magnet) at SLRI, Thailand. The surface area was obtained by using the Brunauer-Emmett-Teller analyzer (BEL SORP MINI II, JAPAN). To estimate the weight percentage of residual carbon and $CuMnFe_2O_4$ in the composite nanostructure, the thermal gravimetric analyzer (TGA/DSC, NETZSCH STA 449F3, Germany) was used.

3.4 Electrochemical measurements

The electrochemical measurement is the measuring of electrical quantities (current, potential, or charge) and their relationship to chemical parameter. The electrochemical performance was performed using cyclic voltammetry (CV), galvanic static charge discharge (GCD) and electrochemical impedance spectroscopy (EIS) techniques on a PGSTAT 302N (Auto lab, The Netherlands). Three electrodes configuration consisting of working electrode (WE), counter electrode (CE) and reference electrode (RE) was used in 2.0 M KOH aqueous solution. The WE electrode was prepared by mixing an active sample with acetylene black (conductive agent) and polyvinylidene difluoride (binder) with a weight ratio of 8:1:1 in DMF solvent. The mixed precursor in a slurry produced by sonicating for 60 min was dropped onto the 1 cm^2 Ni foam and then dried at 70 ^{o}C on a hot plate. A platinum (Pt) wire and silver/silver chloride (Ag/AgCl) were used as CE and RE electrodes, respectively. The CV measurements were carried out at different scan rates ranging from 2 to 200 mV/s. The charge/discharge between the selected potential windows was measured with current density of 2 and 5 A/g. While, EIS spectra was taken over a frequency range of 100 kHz to 0.01 Hz.

According to cyclic voltammetry (CV) technique, the specific capacitance for the variation of voltage with time is given by

$$C(F/g) = \frac{\int IdV}{mv\Delta U}, \tag{1}$$

where term $\int IdV$ refers to the area surround the CV curve, m is the weight of the active material within the electrode, v is the scan rate and ΔU is the voltage window. The corresponding energy and the power density are given as equation (2) and (3). In this work, the CV measurement was performed at various scan rates in 2 M KOH electrolyte solution.

Galvanostatic charge discharge (GCD) technique is an electrochemical analysis to investigate the charging and the discharging process of electrochemical capacitors. The basic principle is placing a constant current upon an electrode and measuring the variation of the resulting current through the solution. The discharge capacitance (C) is estimated from the current (I) and slope ($\Delta V / \Delta t$) of the linear portion of the discharge curve via the expression.

$$C = \frac{I}{\Delta V / \Delta t} \tag{2}$$

The specific capacitance with mass m is thus given by

$$C_s = \frac{I\Delta t}{m\Delta V} \tag{3}$$

where m is the weight of the active material electrode. In this work, the GCD measurements were performed in 2 M KOH at various current densities (depends on the prepared materials).

Electrochemical impedance spectroscopy (EIS) is an electrochemical method that used a frequency response to evaluate the electrochemical behavior (kinetics, resistive, capacitive, etc.) of cell electrode. A brief concept is applying a sinusoidal potential of small amplitude to the cell electrodes and recorded the resulting current response. According to Ohm's law, the complex impedance is then defined as

$$Z = \frac{V(t)}{I(t)} = |Z| \frac{\cos(\omega t)}{\cos(\omega t - \phi)} = |Z| e^{j\phi} = |Z| (\cos\phi - j\sin\phi) = Z^{'} - jZ^{"} \tag{4}$$

Where $Z^{'}$ and $Z^{"}$ are the real and imaginary parts of the complex impedance, respectively. The phase angle (ϕ) and the modulus $(|Z|)$ are as following equation

$$\phi = \tan^{-1}\left(\frac{z^{"}}{z^{'}}\right) \tag{5}$$

$$|Z| = \sqrt{\left(Z^{'}\right)^2 + \left(Z^{"}\right)^2} \tag{6}$$

At $\phi = 0$, the impedance is real $Z(\omega) = Z^{'}(\omega)$ (purely resistive behavior). The capacitance in term of real ($C^{'}$) and imaginary ($C^{"}$) part are as the following equation

$$C = \frac{1}{j\omega Z} = \frac{Z^{"}}{\omega |Z|^2} - j\left(\frac{Z'}{\omega |Z|^2}\right) = C^{'} - jC^{"} \tag{7}$$

The real part is the effective capacitance that the devices can delivery, while the imaginary part related to the irreversible resistivity loss in the device. According to the equation, the impedance decrease with increasing of capacitance and frequency. For electrochemical capacitor, high frequency and smaller time constant is a characteristic of high power density. In this work, the EIS measurements were performed after cyclic voltammetry test in order to study their resistive behavior. The measurements were carried out in the frequency range of 0.1 Hz to 10^5 Hz which is typically used for most electrochemical systems.

The flowchart diagram showing the overview of experimental procedure performed in this work is illustrated as followed

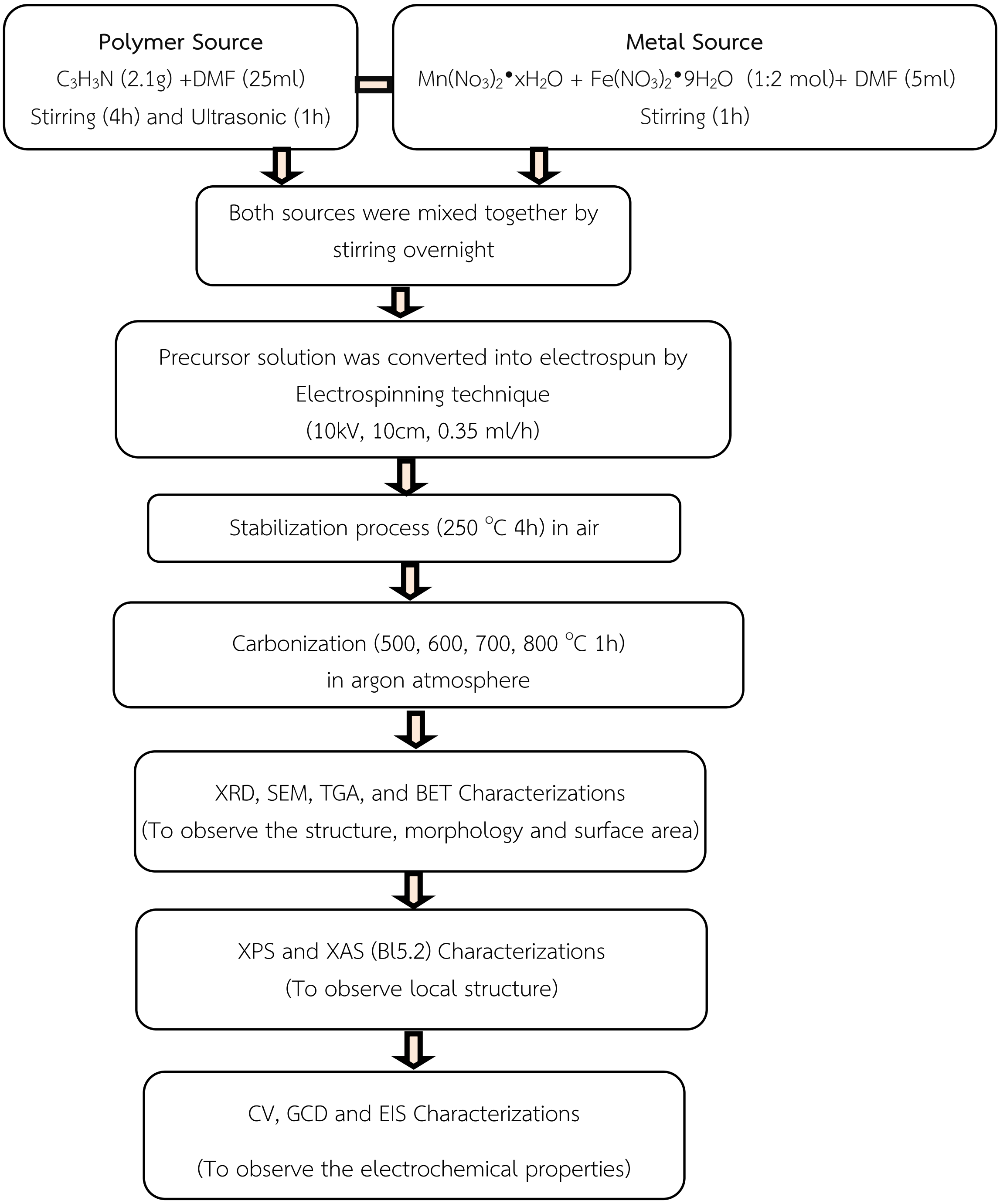

Fig. 3-1 Diagram showing the preparation and characterization of CNF/$MnFe_2O_4$ composite nanostructures.

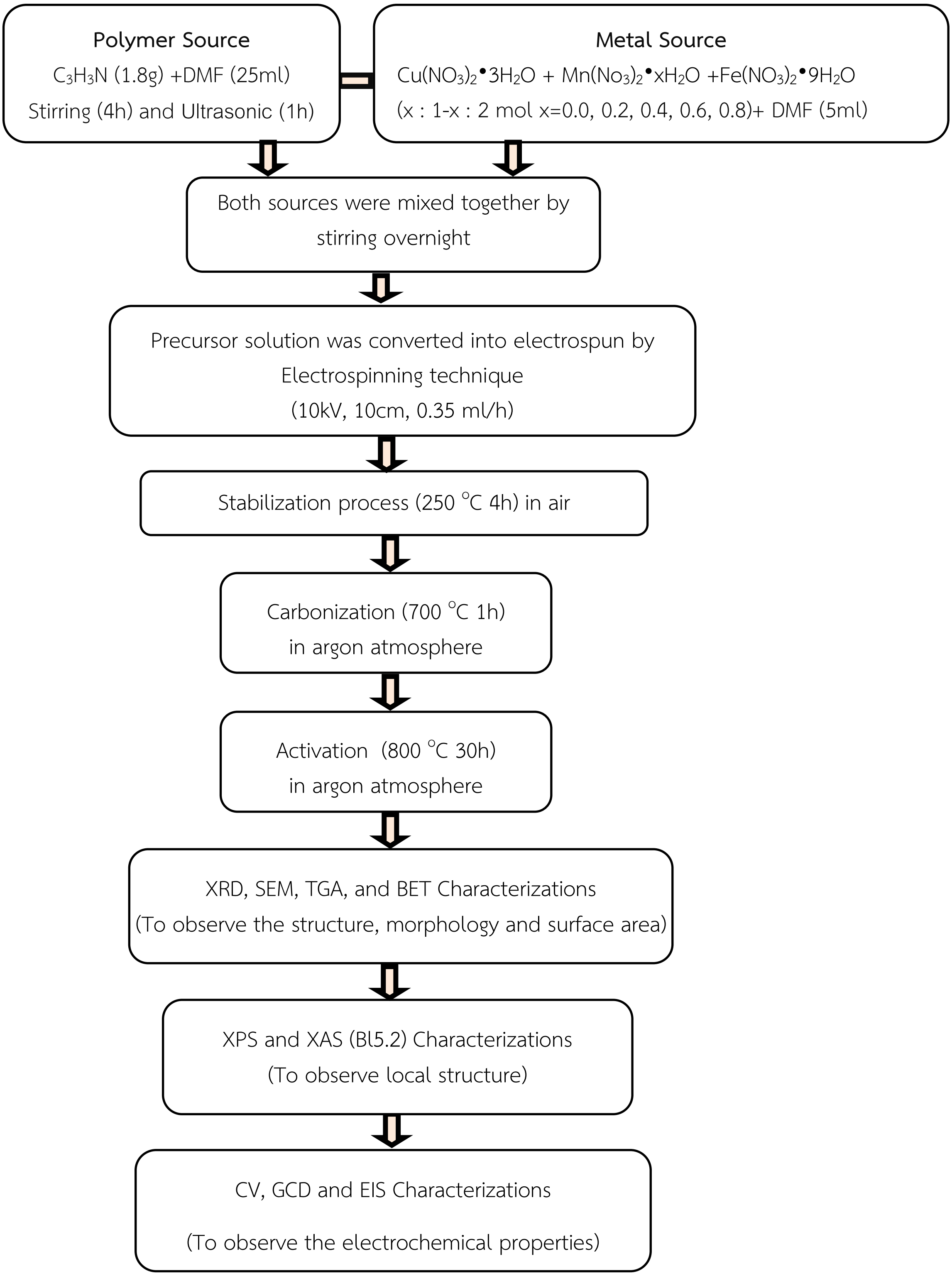

Fig. 3-2 Diagram showing the preparation and characterization of ACNF/$Cu_xMn_{1-x}Fe_2O_4$ composite nanostructures.

4. Results and discussion

This section deals with the results and their discussion. It is divided into two sections related to two different groups of prepared samples: CNF/ $MnFe_2O_4$ and ACNF/$Cu_xMn_{1-x}Fe_2O_4$, respectively.

4.1 CNF/$MnFe_2O_4$ composite nanostructures

To observe the crystal structure of CNF/$MnFe_2O_4$ composite nanostructures, the X-ray diffraction spectroscopy was used. Fig. 4-1 shows the XRD pattern of CNF/$MnFe_2O_4$ nanostructures carbonized at 500, 550, 600 and 700 °C. After carbonization process, PAN nanofibers are converted into CNFs, while metal source is reduced to form manganese ferrite. The peaks at 2θ of 18.318°, 30.183°, 35.579°, 43.134°, 53.684°, 57.12°, and 62.789° are indexed to the (111), (220), (311), (400), (422), (511), and (440) planes, respectively, of face-centered cubic structure of $MnFe_2O_4$ in the standard data no. 10-0319. The diffraction peak (311) became narrower with increasing temperatures indicating the increase of crystallite size. Based on the Scherrer equation [31], the crystallite size are in the range of 13–69 nm. The corresponding lattice constant and d-spacing are slightly decreased with increase of carbonization temperature (Table. 1). The broad peak at 25.2° and 42.6° corresponding to the graphitic crystallite planes of (002) and (100) in JCPDS card no. 75-1621, respectively [32].

Table. 1 Summary of crystallite size, lattice constant, d-spacing, mean pore diameter, total pore volume and surface area of CNF/ $MnFe_2O_4$ composite nanostructures carbonized at 500 to 700 °C

samples	Crystallite size (nm)	Lattice constant (Å)	d-spacing (Å)	Mean pore diameter (nm)	Total pore volume (cm^3g^{-1})	Surface area (m^2g^{-1})
500 °C	12.93	4.685	2.5552	27.90	0.0826	11.84
550 °C	41.43	4.682	2.5536	20.44	0.1019	19.93
600 °C	46.00	4.674	2.5497	15.97	0.1533	38.38
700 °C	68.90	4.622	2.5213	7.47	0.4474	239.4

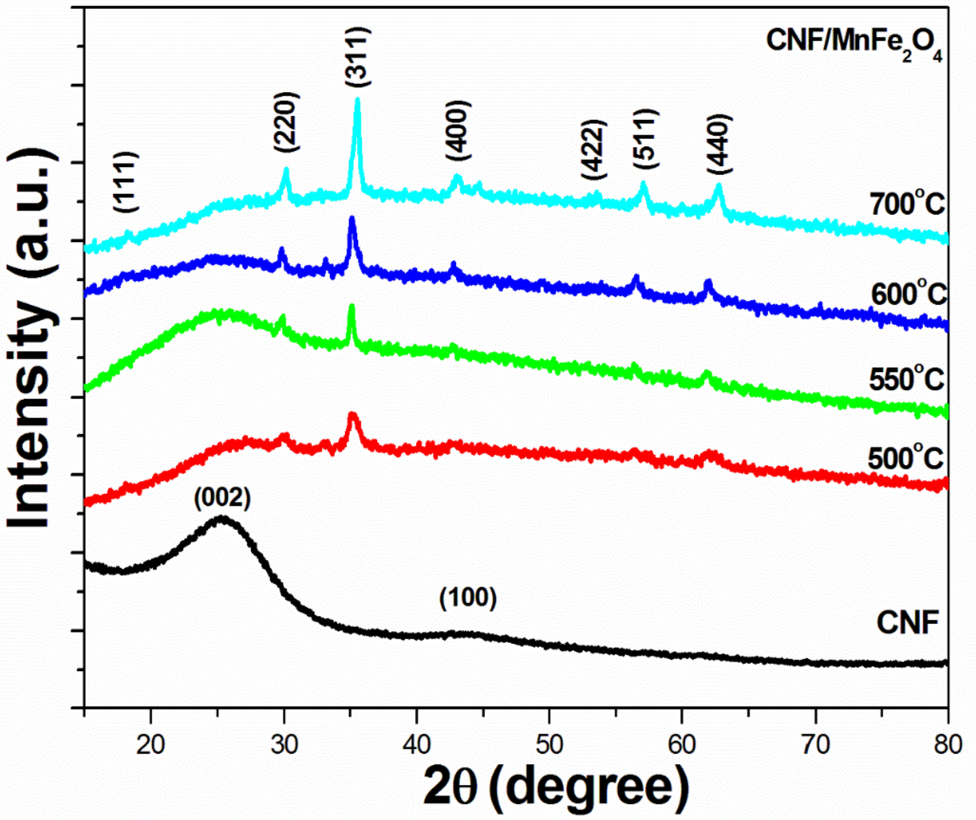

Fig. 4-1 XRD patterns of CNF and CNF/ $MnFe_2O_4$ composite nanostructure carbonized at 500 to 700 °C.

To observe the morphology of CNF/$MnFe_2O_4$ composite nanostructures, the field emission scanning electron microscopy was used Fig. 4-2 shows Fe-SEM images of CNF/$MnFe_2O_4$ composite nanostructures carbonized at different temperatures (500-700 °C). The increasing of carbonization temperature plays an important role to change morphology from nanofibers to nanoparticles. At low temperature of 500 and 550 °C (Fig. 4-2 (a)-(b)), the fibers revealed long, smooth and uniform in cross-section with the average diameter of ~730 and 780 nm, respectively. The fibers became to shrink and fracture with diameter of ~360 nm at 600 °C (Fig. 4-2 (c)) and reduced to be particles with average size of 84 nm after being carbonized at 700 °C (Fig. 4-2 (d)). Normally, CNFs used in electrochemical cell have a diameter less than 1 μm [33]. It is expected that, small diameter of prepared samples offers shortens length for charge diffusion.

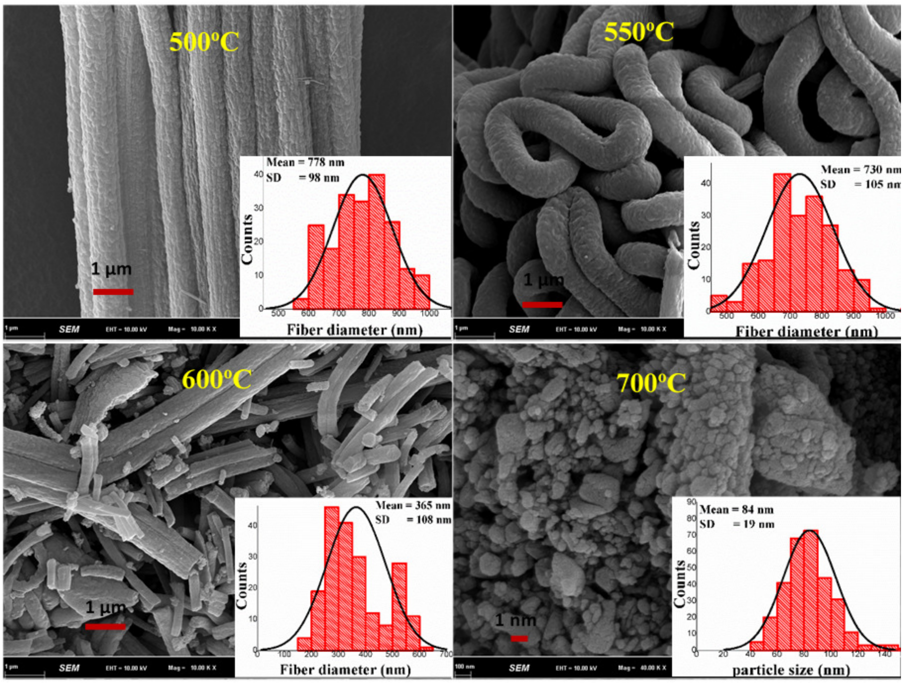

Fig. 4-2 FE-SEM images of the CNF/$MnFe_2O_4$ composite nanostructure carbonized at 500 to 700 °C.

To observe the binding energy peaks of each component in the C/$MnFe_2O_4$ composite nanostructure, the X-ray photoemission spectroscopy was used. Fig. 4-3 represented the XPS spectra of C1s (a), Fe*2p* (b), Mn*2p* (c), and O*1s* (d) for all C/$MnFe_2O_4$ composite nanostructure. To describe the binding energy peaks, the spectra were fitted and some of them are presented in Fig.4-4. All fitted data are listed in Table. 2. The Mn*2p* spectra (Fig. 4-4 (a-d)) show two main peaks at ~641 and ~653 eV, which are attributable to Mn*2p*3/2 and Mn*2p*1/2, respectively of Mn^{2+} [34]. The separation between these two peaks of 11.52, 11.55, 11.49 and 11.52 eV were observed for the sample carbonized at 500, 550, 600 and 700 °C, respectively. The obtained values are approximately equal to 11.5 eV for Mn^{2+} [35]. Peak fitting of the C1s spectrum exhibits three main components arising from C–C (~284 eV), C–O (~286 eV) and C=O (~288 eV) bonds (Fig. 4-4 (e)) [36-37]. XPS fitted spectra of Fe2p were composed of multiple peaks (Fig. 4-4 (f)). Two main peaks at ~710 and ~725 eV are ascribed to the Fe2p3/2 and Fe2p1/2 of Fe^{3+}, respectively [38]. The distinct satellite peaks at about 8 eV above the main peak confirmed the presence of Fe^{3+} in the prepared samples [39-40]. Fig. 4-4 (g) shows three main peaks of O1s fitted spectra. The main peak at ~530 eV was attributed to the lattice oxygen of the metal oxides (Fe–O or Mn–O of $MnFe_2O_4$). The higher binding peak energy at ~532, and ~533 eV were compatible with the oxygen groups bonded with carbon atoms (C-O or C=O).

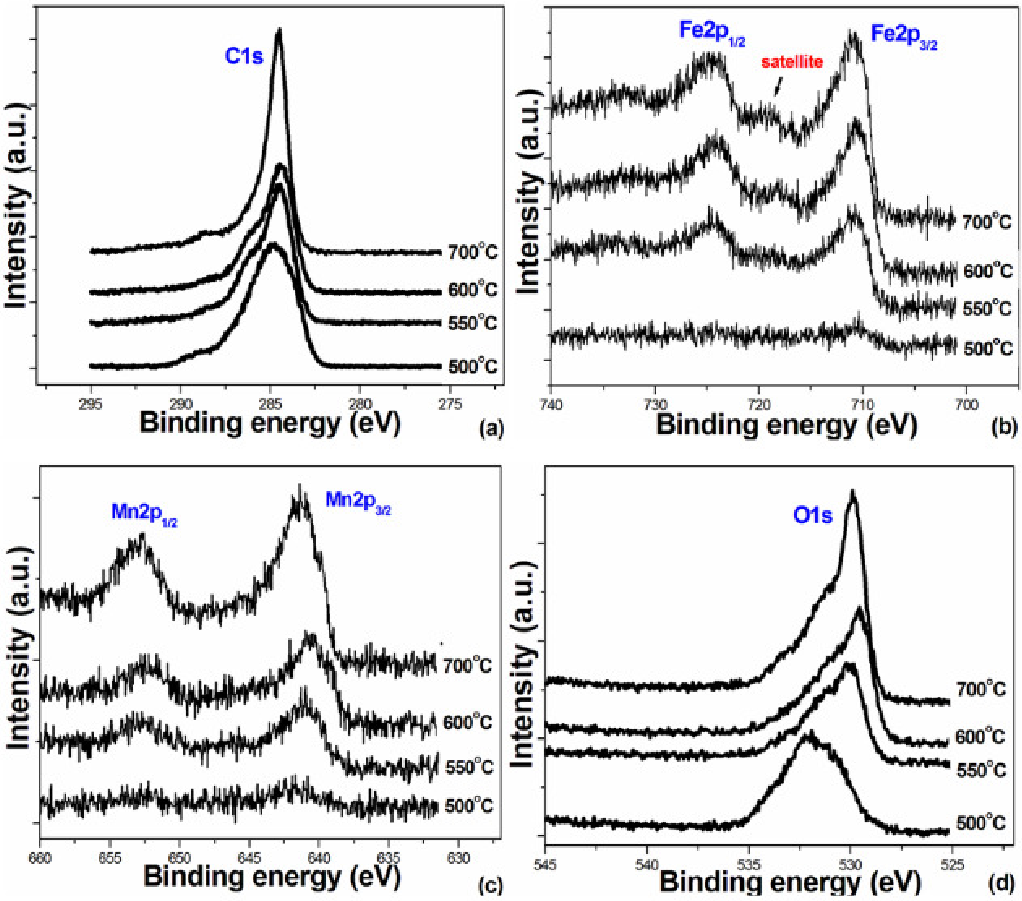

Fig. 4-3 XPS spectra for all CNF/$MnFe_2O_4$ composite nanostructure at (a) C1s, (b) Fe2p (c) Mn2p and (d) O1s.

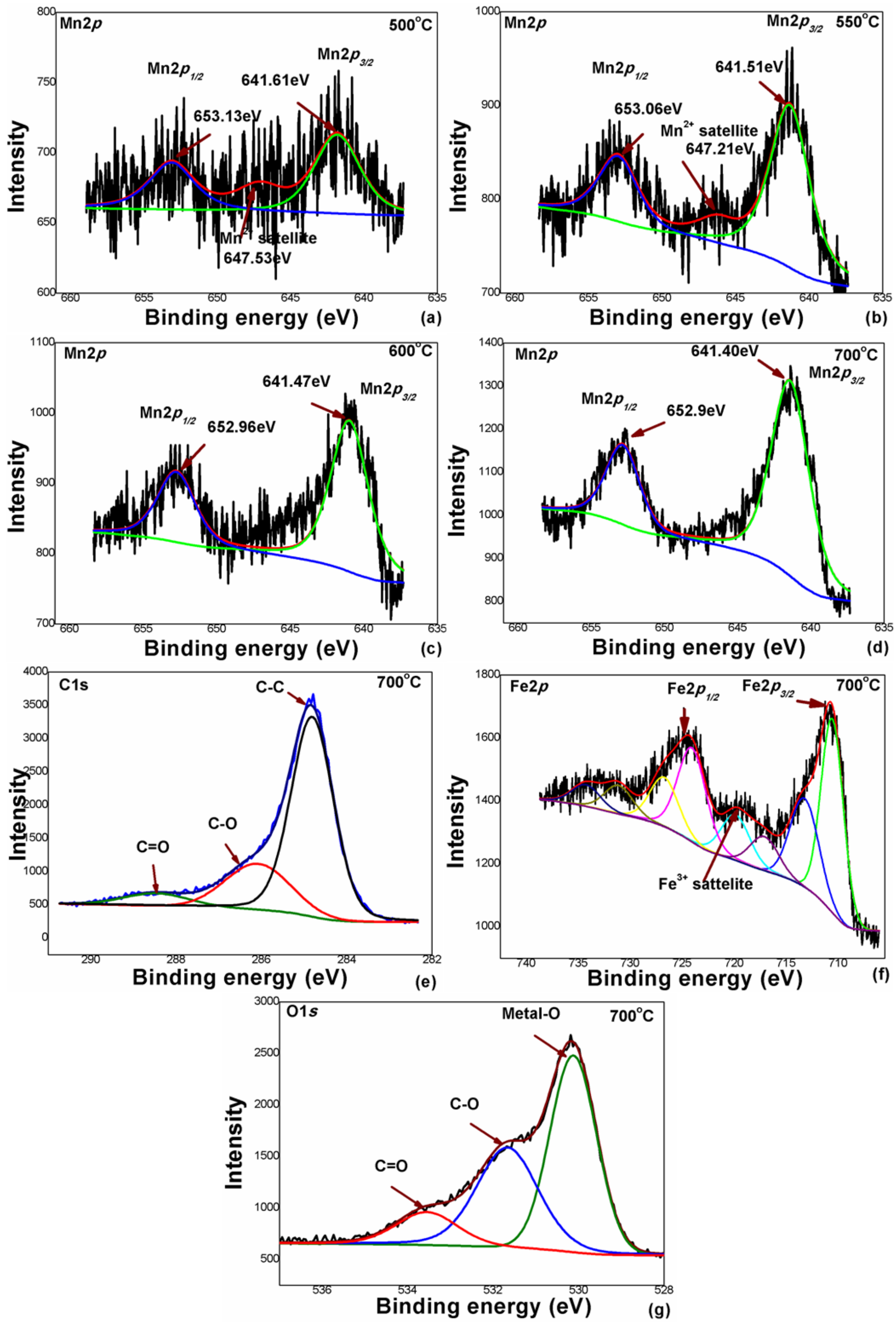

Fig. 4-4. Fitted XPS spectra of Mn2p for CNF/MnFe$_2$O$_4$ carbonized at 500, 550, 600 and 700 °C (a-d) and fitted XPS spectra of C1s, Fe2p, and O1s, respectively for CNF/MnFe$_2$O$_4$ carbonized at 700 °C (e-g)

Table. 2 XPS fitting data of C1s, Fe2p, Mn 2p and O1s of all CNF/$MnFe_2O_4$ composite nanostructures.

samples	C1s	Fe2p	Mn2p	O1s
500 °C	284.27 C-C	710.76	641.61	530.84 M-O*
	285.75 -C-O	724.13	653.13	531.93 C-O
	288.34 -C=O	(Fe^{3+})	(Mn^{2+})	533.38 C=O
550 °C	284.64 C-C	711.61	641.51	530.41 M-O*
	286.31 -C-O	724.26	653.06	531.61 C-O
	288.30 -C=O	(Fe^{3+})	(Mn^{2+})	533.46 C=O
600 °C	284.78 C-C	711.12	641.47	530.27 M-O*
	286.59 -C-O	725.32	652.96	531.46 C-O
	288.68 -C=O	(Fe^{3+})	(Mn^{2+})	533.38 C=O
700 °C	284.81 C-C	711.25	641.40	530.19 M-O*
	286.08 -C-O	723.7	652.90	531.67 C-O
	288.46 -C=O	(Fe^{3+})	(Mn^{2+})	533.55 C=O

*M is metal (Fe or Mn)

To further verify the cations distribution and local environment around the absorber in the spinel structure, the X-ray absorption spectroscopy was used, and the EXAFS spectra at Mn and Fe K-edge were fitted. The Fourier transform ($\chi(R)$) in R space and the $k^3\chi(k)$ weighted in k space from experiment (black line) and fit results (red dash) are shown in Fig. 4-5. The non-linear least square fitting data are given in Table 3. The $k\chi^3(k)$ values at both Mn and Fe K-edges (Fig. 4-5 (c) and (d)) are similar for all prepared samples, indicating similarity of the local environment around the absorber Mn and Fe ions. The cations distribution can be explained by a degree of inversion between A and B-sites (as seem by S_0^2). Typically, in an inverse spinel the Mn^{2+} ions are all located in B-sites, while half of the Fe^{3+} ions preferentially occupy A-site and the rest fill B-sites [41]. According to the fitting data, all prepared samples exhibit partially inverse spinel structure that is both sites contain a fraction of Mn^{2+} and Fe^{3+} cations. The portion of Mn ions in A and B site of about 53.8 and 46.2%, 57.3 and 42.7%, 68.6 and 31.4%, and 70.7 and 29.3% were observed for CNF/$MnFe_2O_4$ carbonized at 500, 550, 600 and 700 °C, respectively. Interestingly, the higher carbonization temperature can switch Mn cations from B to A-sites. Moreover, the percentage of Mn in A-site at 700 °C very closely to previous report on bulk $MnFe_2O_4$ [42]. In the speinel ferrite structure, the substitution cations to change their valence state are critical for offering pseudocapacitance [43]. In our work, the distribution of Fe^{3+} ions in A and B sites are nearly similar proportion. So, the different distribution of Mn over A and B-site may leads to different electrochemical properties.

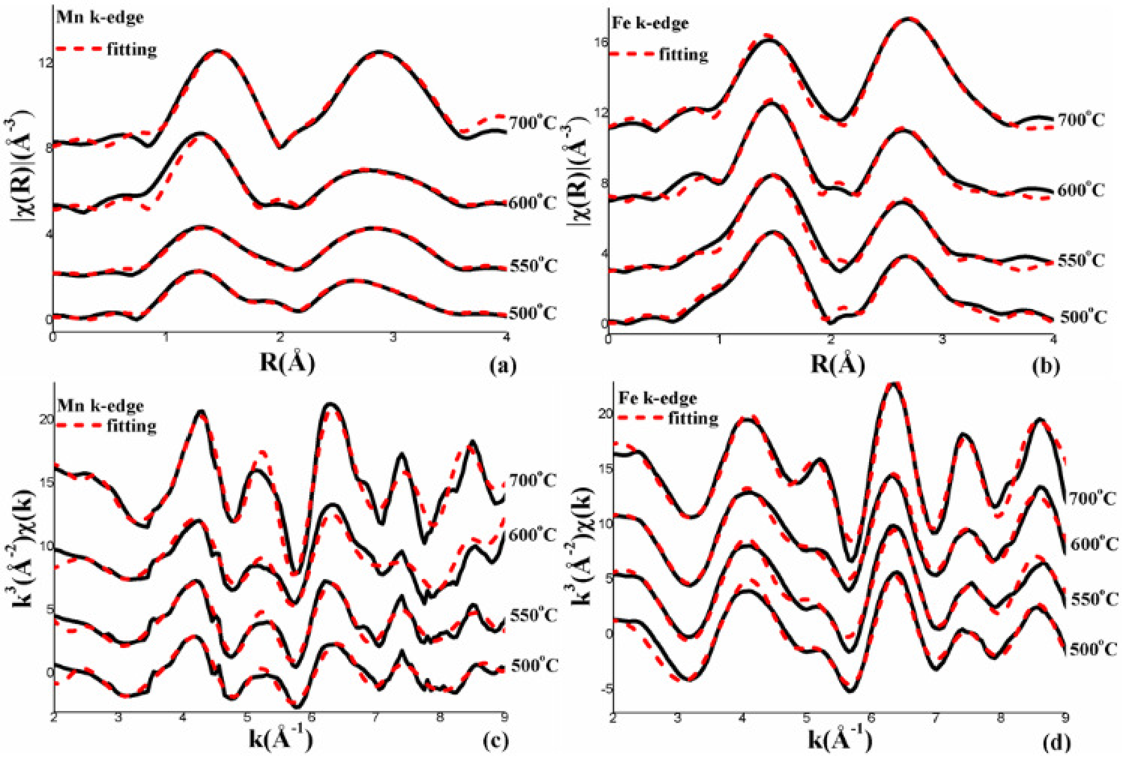

Fig. 4-5. Fourier transform at Mn and Fe K-edge (a, b), and the corresponding $k^3(\chi(k))$ plots (c, d) from experiment (solid line) and fitting (dash line)

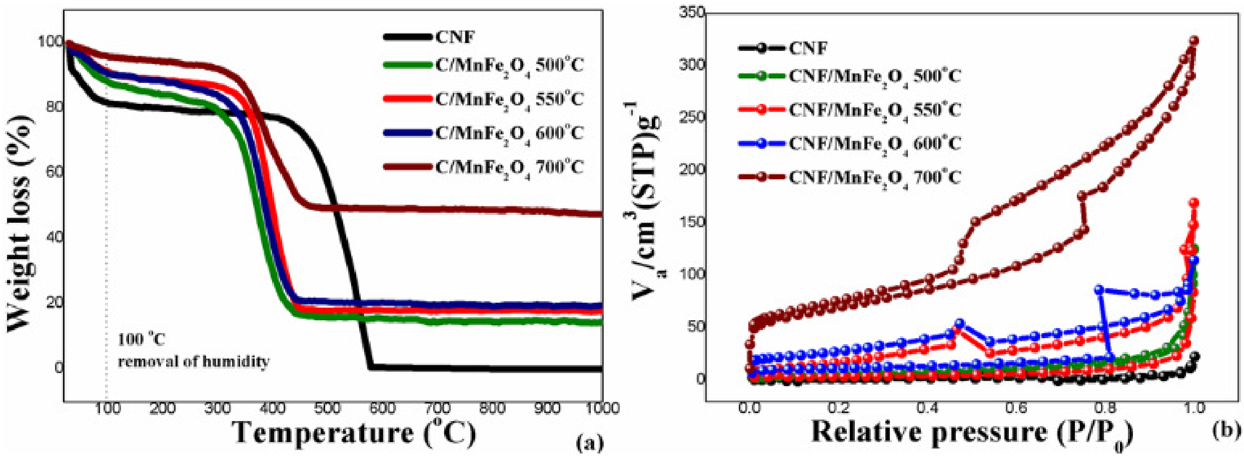

Fig. 4-6. (a) TGA curves and (b) adsorption-desorption isotherms of CNF/ $MnFe_2O_4$ carbonized at 500 to 700 °C.

Table. 3 Lists of coordinate number (N), amplitude reduction (So^2), and interatomic distances (R) from EXAFS fitting

Sample	Shell	N	So^2	R(Å)	Shell	N	So^2	R(Å)
Mn K-edge_500°C					Fe K-edge_500°C			
A site	Mn-O	4	0.538	1.9276	Fe-O	4	0.445	1.8335
	Mn -Mn	6	0.538	3.1633	Fe -Mn	6	0.445	3.4475
	Mn -Fe	4	0.538	3.8417	Fe -Fe	4	0.445	3.6008
B site								
	Mn -O	6	0.462	2.1419	Fe -O	6	0.462	1.9916
	Mn -Fe	3	0.462	2.9014	Fe -Fe	6	0.462	3.3331
	Mn -Fe	6	0.462	3.3455	Fe -O	6	0.462	3.4921
Mn K-edge_550°C					Fe K-edge_550°C			
A site	Mn-O	4	0.573	1.9417	Fe -O	4	0.499	1.9507
	Mn -Mn	6	0.573	3.1895	Fe -Mn	6	0.499	3.6678
	Mn -Fe	4	0.573	4.0713	Fe -Fe	4	0.499	3.8309
B site								
	Mn -O	6	0.427	2.1311	Fe -O	6	0.487	2.0997
	Mn -Mn	3	0.427	3.0052	Fe -Mn	3	0.487	2.9968
	Mn -Fe	6	0.427	3.4229	Fe -Fe	6	0.487	3.5140
Mn K-edge_600°C					Fe K-edge_600°C			
A site	Mn-O	4	0.686	1.9321	Fe -O	4	0.520	1.9634
	Mn -Mn	6	0.686	3.5128	Fe -Mn	6	0.520	3.6916
	Mn -Fe	4	0.686	3.7653	Fe -Fe	4	0.520	3.8558
B site								
	Mn -O	6	0.314	2.1366	Fe -O	6	0.464	2.1338
	Mn -Fe	3	0.314	2.8883	Fe -Mn	3	0.464	3.0455
	Mn -Mn	3	0.314	3.0052	Fe -Fe	6	0.464	3.5711
Mn K-edge_700°C					Fe K-edge_700°C			
A site	Mn-O	4	0.707	1.9450	Fe -O	4	0.522	1.9573
	Mn -Mn	6	0.707	3.5134	Fe -Mn	6	0.522	3.6801
	Mn -Fe	6	0.707	3.6932	Fe -Fe	4	0.522	3.8438
B site								
	Mn -O	6	0.293	2.0970	Fe -O	6	0.485	2.1192
	Mn -Fe	3	0.293	2.8615	Fe -Mn	3	0.485	3.0246
	Mn -Mn	3	0.293	3.0052	Fe -Fe	6	0.485	3.5466

To estimate the weight percentage of residual carbon and $MnFe_2O_4$ in the composite nanostructure, the thermal gravimetric analysis was used. Fig. 4-6 (a) shows the weight loss spectra as a function of temperature for all $C/MnFe_2O_4$ composite nanostructure. The dramatic weight losses in the temperature range of 300-580 ^oC was related to the decomposition of metal nitrates along with the degradation of PAN polymer chain. The weight percentage of $MnFe_2O_4$ was determined from residue weight loss at 1000 ^oC. The value of 14.3, 17.8, 19.5 and 47.6% were observed for the samples 500, 550, 600 and 700^oC, respectively. The corresponding contents of carbon are 73.6%, 73.5%, 70.1% and 48.3%, respectively. As known that, EDLC is the source of energy storage for carbonaceous materials, while pseudocapacitance being for metal oxide systems. Therefore, high residual content of $MnFe_2O_4$ supporting pseudocapacitance.

To observe the surface area and pore size of the prepared samples, the the Brunauer-Emmett-Teller analyzer was used. Fig. 4-6 (b) shows the adsorption and desorption isotherms for all prepared samples. The isotherms exhibit IUPAC type IV pattern, indicating the existence of mesoporous. It was found from Table. 1 that the surface area and total pore volume increased with increasing of carbonization temperature, meanwhile the mean pore diameter decreased possibly due to the growth of crystallite size of $MnFe_2O_4$. The increasing of surface area supporting large number of reaction sites, resulting in an improved electrical double layer capacitance (EDLC).

To study the electrochemical properties of the prepared electrodes, the cyclic voltammetry (CV) was used. Fig. 4-7 shows CV curves over a wide voltage range of -1.2–0.1 V at various scan rates. The potential windows are slightly higher to the theoretical decomposition voltage of water (1.23 V). However, for the application of energy storage in aqueous supercapacitors, the operating voltage can be enlarged due to the existence of over-potential under the gas evolution. No any redox peaks were observed for pure CNF (Fig. 4-7 (a)), which is a characteristic of EDLC of carbon-based materials [44-45]. The composite electrodes (Fig. 4-7 (b)-(e)) show redox peaks implying to pseudo-capacitive behavior of $MnFe_2O_4$. The peaks in positive and negative current region known as anodic and cathodic peaks, respectively. Normally, the redox process of $MnFe_2O_4$ is described as the following equation [46]

$$MnFe_2O_4 + H_2O + 2e^- \leftrightarrow 4MnO + FeO + 2OH^{-\ -} \tag{8}$$

Among all electrodes, $C/MnFe_2O_4$_700^o has the largest capacitive area with sharpest peak (as inset of Fig. 4-7 (e)). At 2 mV/s, the sharp cathodic peak of -1.1 V might be due to the reduction of $MnFe_2O_4$ to metallic Mn and Fe, while the anodic peak appeared at about -0.7 V can be assigned to the oxidation of metallic Mn to MnO or Fe to Fe_2O_4. The potential separation between two peaks (ΔE_{pp}) increase with increasing of potential scan rate (Fig. 4-7 (f)) indicating their irreversible behavior. This may arise from the effect of resistance or the increase of over potentials [47]. According to CV spectra, the specific capacitances (Fg^{-1}) was evaluated via equation (1). The obtained results are shown in Fig. 4-8 (a). It was found that, the C_S value decreased with increases of potential scan rate possibly due to insufficient time for accessible of the electrolyte ions into the inner pores or the gaps between the uniform nanoparticles [48]. Moreover, the C_S value at all scan rate increases with increasing of carbonization temperature. The maximum value is offered by the sample carbonized at 700 °C (345 Fg^{-1} at 2 mV/s), in which nearly consistent to 313 Fg^{-1} (at 5 mVs^{-1}) of $MnFe_2O_4$ thin film electrode in the same electrolyte [49]. The C_S value was also evaluated from the constant current discharge technique at 5 Ag^{-1} (Fig. 4-8 (b)). The nonlinear discharge curves indicate the capacitive behavior of prepared samples [50]. No voltage drop was observed, indicating fast I-V response and low internal resistance of prepared electrodes. The C_S value can be obtained by equation (3). It was found from Fig. 4-8 (c) that, the C_S value increased with increasing of carbonization temperature, here also the same trend to previous reported [43]. The maximum C_S value of 291.9 Fg^{-1} (at 5 Ag^{-1}) is nearly consistent to 293.5 Fg^{-1} (at 1 $mAcm^{-2}$) of $MnFe_2O_4$ thin film electrode [49]. High capacitance of CNF/$MnFe_2O_4$_700 °C possibly due to highest degree of graphitization [51], smallest fibers diameter, largest crystallite size, highest residual content of $MnFe_2O_4$, and maximum surface area of CNF. Moreover, it was found from Fig. 4-8 (c) that more Mn in A-sites leads to higher capacitance, indicating their dominant contribution. However, no systematic mechanistic investigation has been carried out and still cannot be clearly explained. Fig. 4-8 (d) shows plot of the capacitance retention after repeated CV at a scan rate of 100 mV/s over 1000 cycles. The values of 95.41, 87.31, 84.24 and 80.20% were observed for CNF, C/$MnFe_2O_4$ carbonized at 500, 600, and 700 °C electrodes, respectively. All electrodes show over 80% indicating their long term cycling stability. The best cycle life of CNF electrode may due to the network structure restricts the change of electrode during charge/discharge process. The stability of C/$MnFe_2O_4$ electrodes drop significantly with increasing of carbonization temperature. Such behavior mainly attributed to either the decreasing of CNF working as elastic buffer or redox reaction arising from $MnFe_2O_4$ nanoparticles caused damage the structure. Moreover, it was found from the Nyquist plot (Fig. 4-9) that, the length spectra at low frequency for C/$MnFe_2O_4$ carbonized at 500 °C is shorter than those of 600 °C and 700 °C, respectively indicating the electrolyte ion just surface being accessed. As a consequence, low volume changes during charge/discharge caused long term cycling stability. The deeper penetrating of electrolyte ion through pores, cracks, inter-crystalline gap, etc. for C/$MnFe_2O_4$ carbonized at 600 °C and 700 °C, respective may leading to high volume changes caused short term cycling stability, respectively.

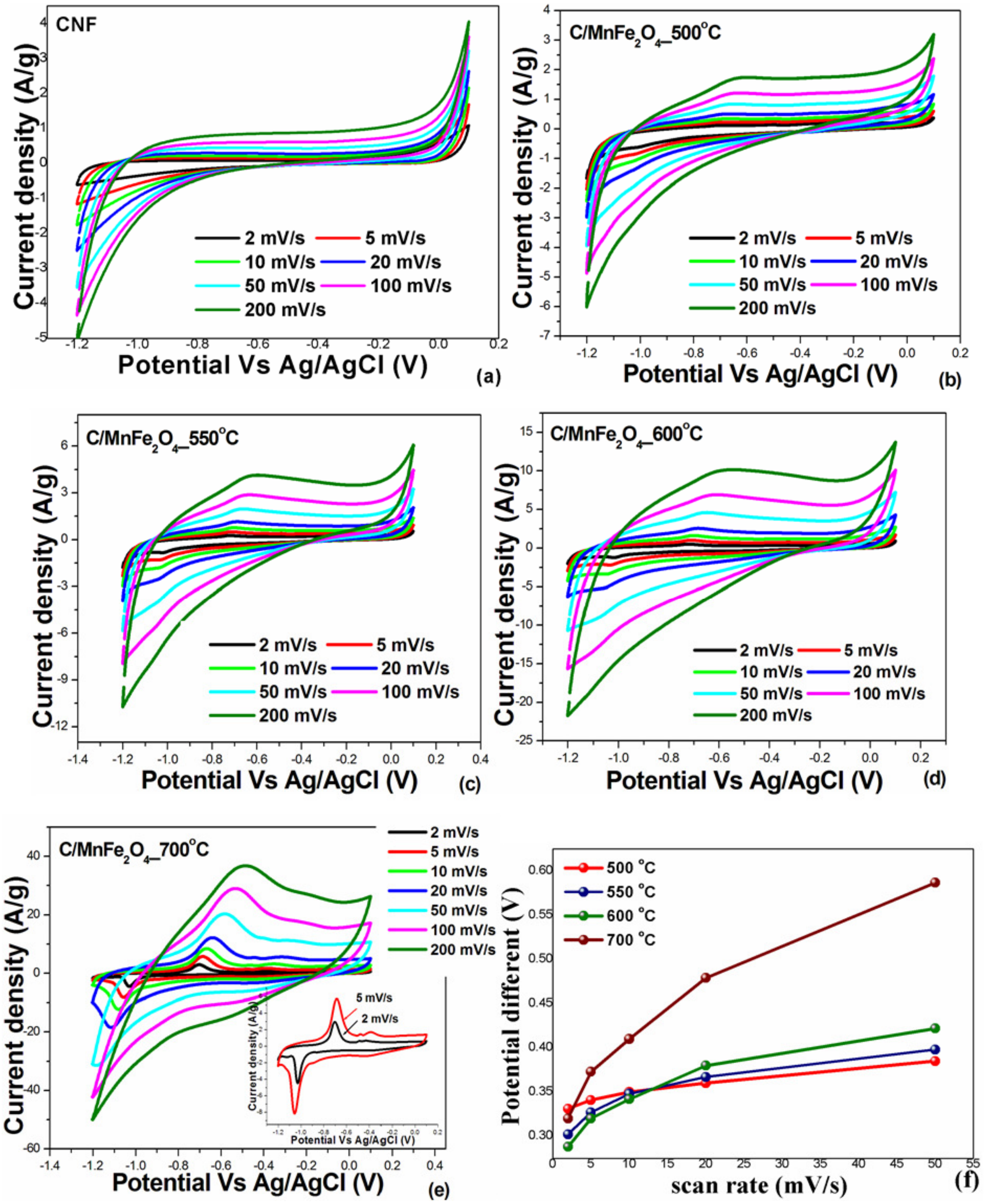

Fig. 4-7. (a-e) CV curves at various scan rate of 2-200 mVs-1 and (d) potential different of CNF/$MnFe_2O_4$ carbonization at 500 to 700 °C.

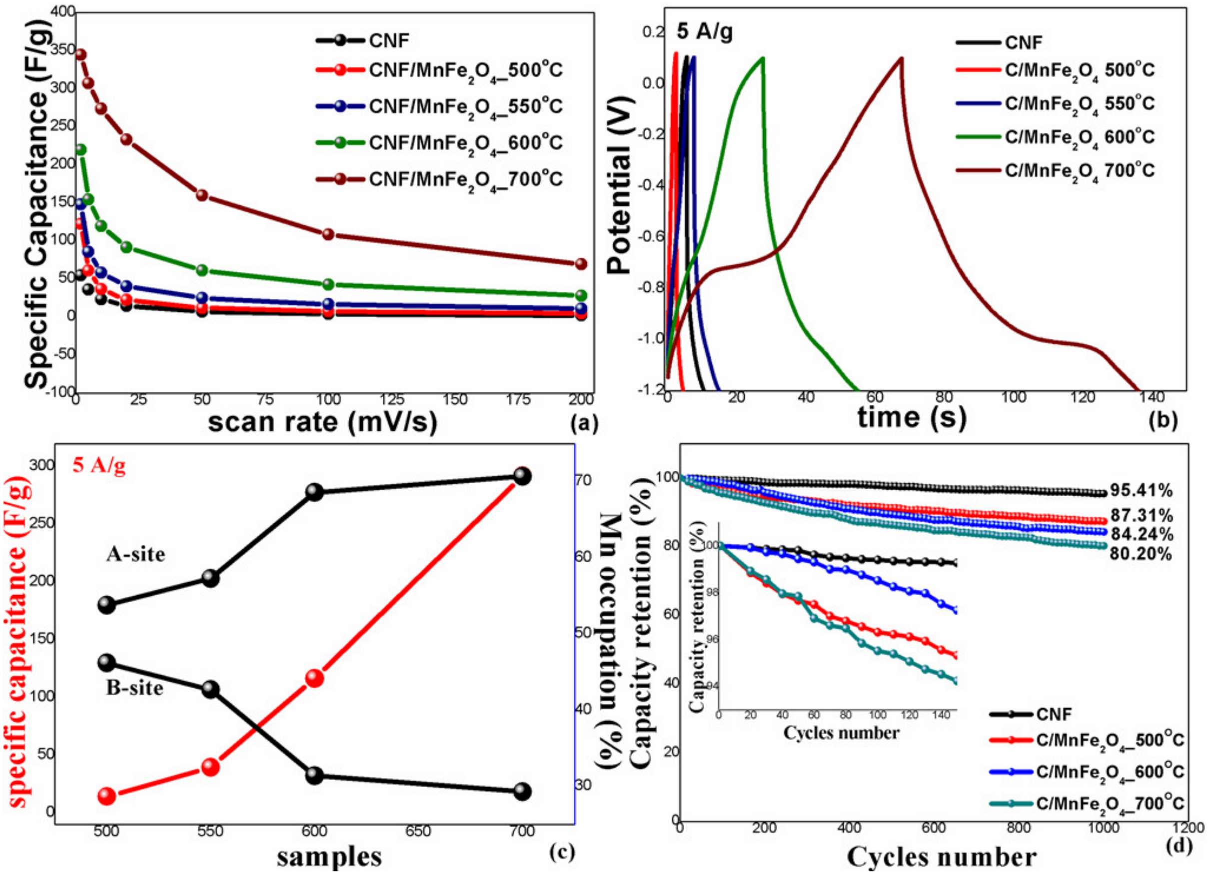

Fig. 4-8. (a) the specific capacitance as function of scan rate from CV (b) galvanostatic charge/discharge spectra at 5 Ag^{-1} (c) the discharge specific capacitance (red line) and the percentage of Mn occupied in A and B-sites (black line), and (d) the capacity retention at 1000 cycles.

To understand the electrical behavior of prepared electrode, the EIS measurement were performed by using the frequency range of 0.01-10^5 Hz. The Nyquist plots for all prepared electrodes are shown in Fig. 4-9. All curves having almost inclination of 45° with imaginary axis and is related to the frequency dependent diffusion resistance of electrolyte ions [52]. At high frequency region, the Nyquist plot of C/MnFe$_2$O$_4$ electrode carbonized at low temperature (500 and 550 °C) show a semicircle related to charge transfer resistance (R_{ct}). While, the semicircle diameter decrease almost vanish for the samples carbonized at higher temperature (600 and 700 °C) demonstrates the enhanced electrochemical behavior. The intercept at x-axis refer to the equivalent series resistances (R_s). The values of 0.810, 0.787, 0.784, 0.775 and 0.762 Ω were observed for CNF and the sample carbonized at 500, 550, 600 and 700 °C, respectively (Fig. 4-9 (b)-(f)). As expected, the R_s values were lower for higher carbonization temperatures samples, signifying the higher current density. The results confirm the electrochemical capacitive properties of the as synthesized electrode.

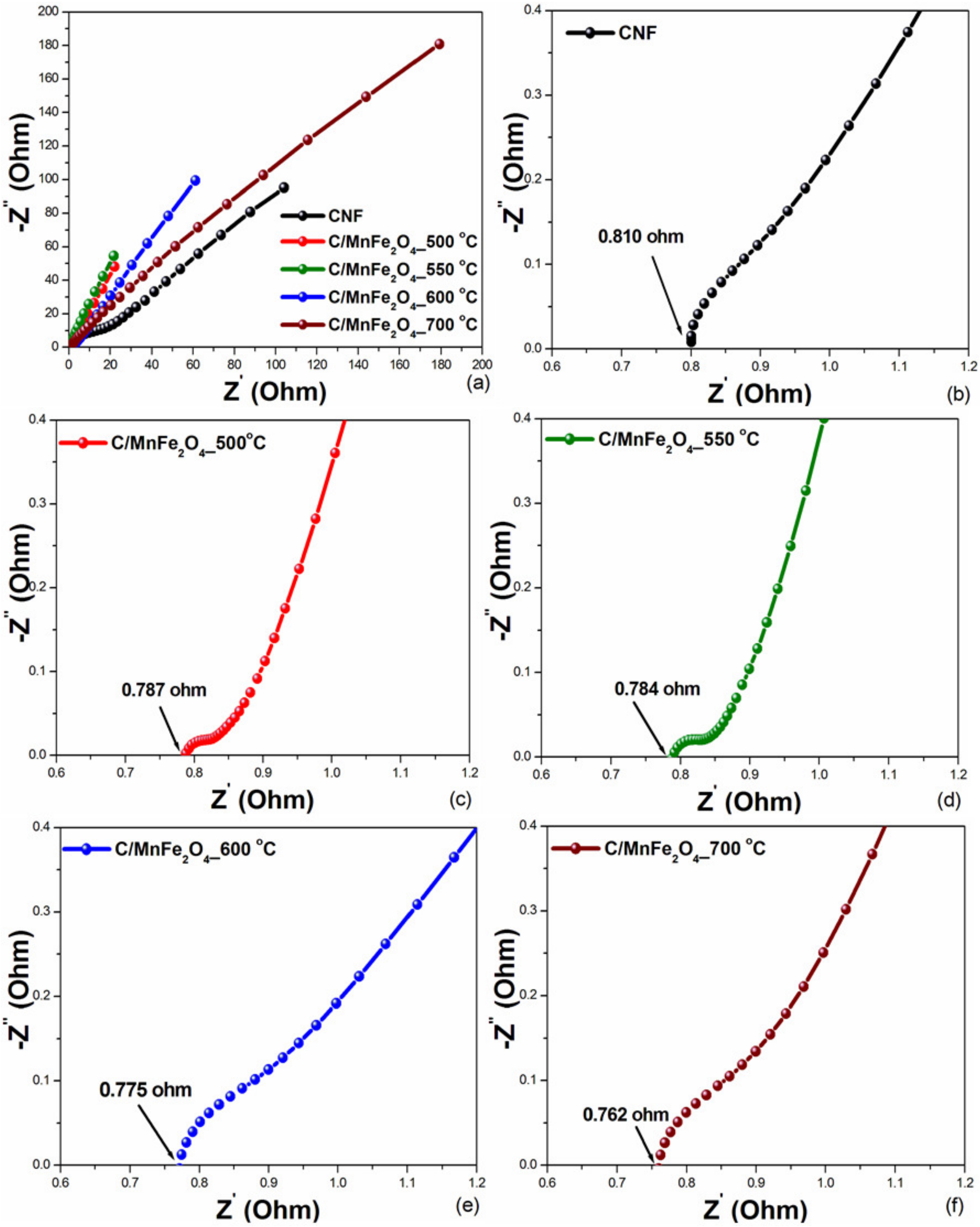

Fig. 4-9 Nyquist plots for CNF, C/MnFe$_2$O$_4$ carbonized at 500, 550, 600 and 700 °C (a) and their portion zooming at high frequency, respectively (b-f).

4.2 ACNF/$Cu_xMn_{1-x}Fe_2O_4$ composite nanostructures

The XRD diffraction patterns of ACNF/$Cu_xMn_{1-x}Fe_2O_4$ composite nanostructure are shown in Fig. 4-10. The peaks at 2θ values of 18.35°, 30.10°, 35.31°, 36.93°, 42.96°, 53.30°, 56.70° and 62.20° can be indexed to (111), (220), (311), (222), (400), (422), (511), and (440) crystal planes of $MnFe_2O_4$ (JCPDS No. 10-0319), while the peak at about 26° confirms the disorder nature of graphite [51] and can be indexed to (002) plane (JCPDS card no. 75-1621). After Cu decoration, three diffraction peaks near 44°, 52° and 75° corresponding to the (111), (200) and (220) planes of copper metal (JCPDS No.85-1326) were observed. With the increasing of " x" , the ferrite peak of (400) around 42° tended to be weak and even disappeared at x=0.8, whereas a new peak of Cu (111) was formed turned up and gradually strengthened. It is speculated that, when the copper oxide is reduced into copper metal during heat treatment process, the spinel structure of the $MnFe_2O_4$ was destroyed. Based on the Scherrer equation [31], the average crystallite size was found to be in the range of 27-48 nm and did not show any significant trend with " x" value. However, sample x=0.2 shows nearly the same size to sample x=0.8, while sample x=0.4 exhibits a similar size to sample x= 0.6. The d-spacing values for all ACNF/$CuMnFe_2O_4$ system are slightly higher than those of ACNF/$MnFe_2O_4$ (x=0) and bulk cubic $MnFe_2O_4$ (2.4298 Å JCPDS 86-2267), possibly due to the effect of ACNF matrix and copper doping. The lattice constant showed slight increase after introducing cupper, suggesting the replacement of Mn^{2+} of radius 0.78 Å or Fe^{3+} 0.69 Å with larger ionic radius of 0.87 Å of Cu^{2+}. Lists of crystallite size, d-spacing and lattice constant are shown in Table. 4.

Fig. 4-11 shows FE-SEM images of the ACNF/ $Cu_xMn_{1-x}Fe_2O_4$ composite nanostructure. All prepared samples exhibited porous surface arising from the activation process. With increase in "x" value, the roughness surface with more nanoparticles covered on were observed. The fibers with diameters varied from 600 to 700 nm were observed for all samples and did not change much with the increase of "x" value. It is worth noting that the nanometer-scale diameter of prepared samples could provide a short ion diffusion distance, which would be beneficial to improve the electrochemical properties of prepared electrode [53]

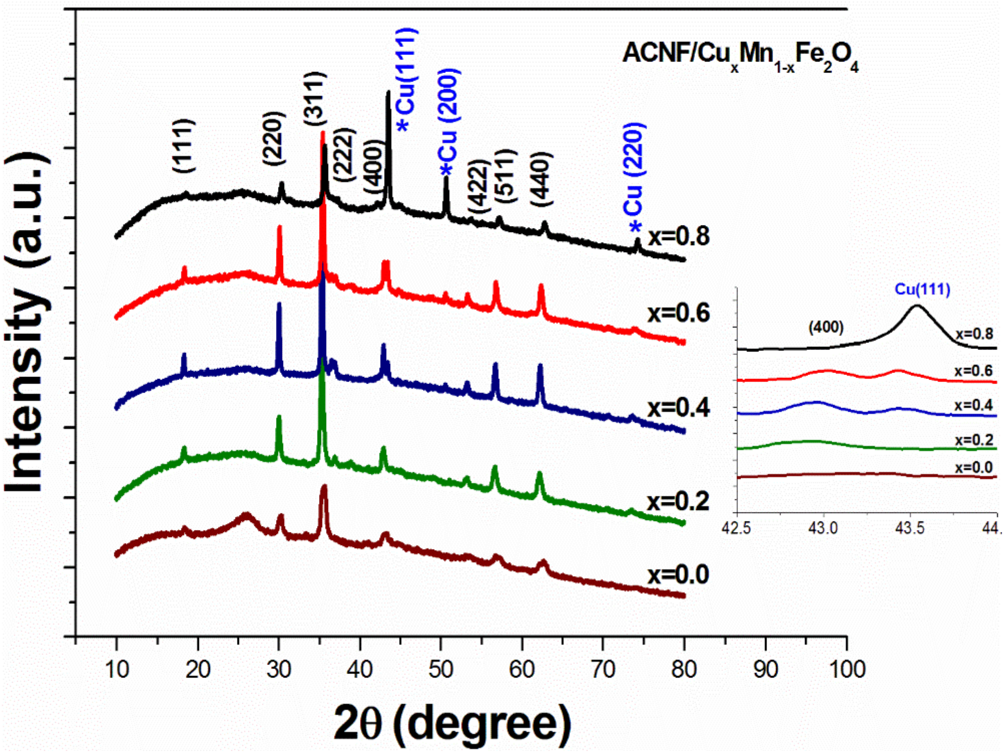

Fig. 4-10 XRD patterns of the ACNF/$Cu_xMn_{1-x}Fe_2O_4$ composite nanostructures

Table. 4 Lists of specific capacitance (C_s), crystallite size (D), d-spacing (d), lattice constant (a), electrolyte resistance (R_s), charge transfer resistance (R_{ct}), the percentage of humidity, carbon, and $CuMnFe_2O_4$, respectively.

Sample	Cs (F/g)		D	d	a	R_s	R_{ct}	humidity	Carbon	$CuMnFe_2O_4$
	CV (2mV/s)	GCD (2A/g)	(nm)	(Å)	(nm)	(Ω)	(Ω)	(%)	(%)	(%)
X = 0.0	175	147.0	27.35	2.5102	0.4602	0.777	0.028	3.5	78.0	18.5
X = 0.2	384	313.9	37.52	2.5397	0.4656	0.854	0.033	0.5	42.3	57.2
X = 0.4	140	122.9	48.28	2.5350	0.4647	0.955	0.039	1.8	35.9	62.3
X = 0.6	144	160.3	43.53	2.5304	0.4639	0.952	0.036	3.1	38.8	58.1
X = 0.8	235	171.7	35.7	2.5151	0.4611	0.938	0.035	2.8	48.8	48.4

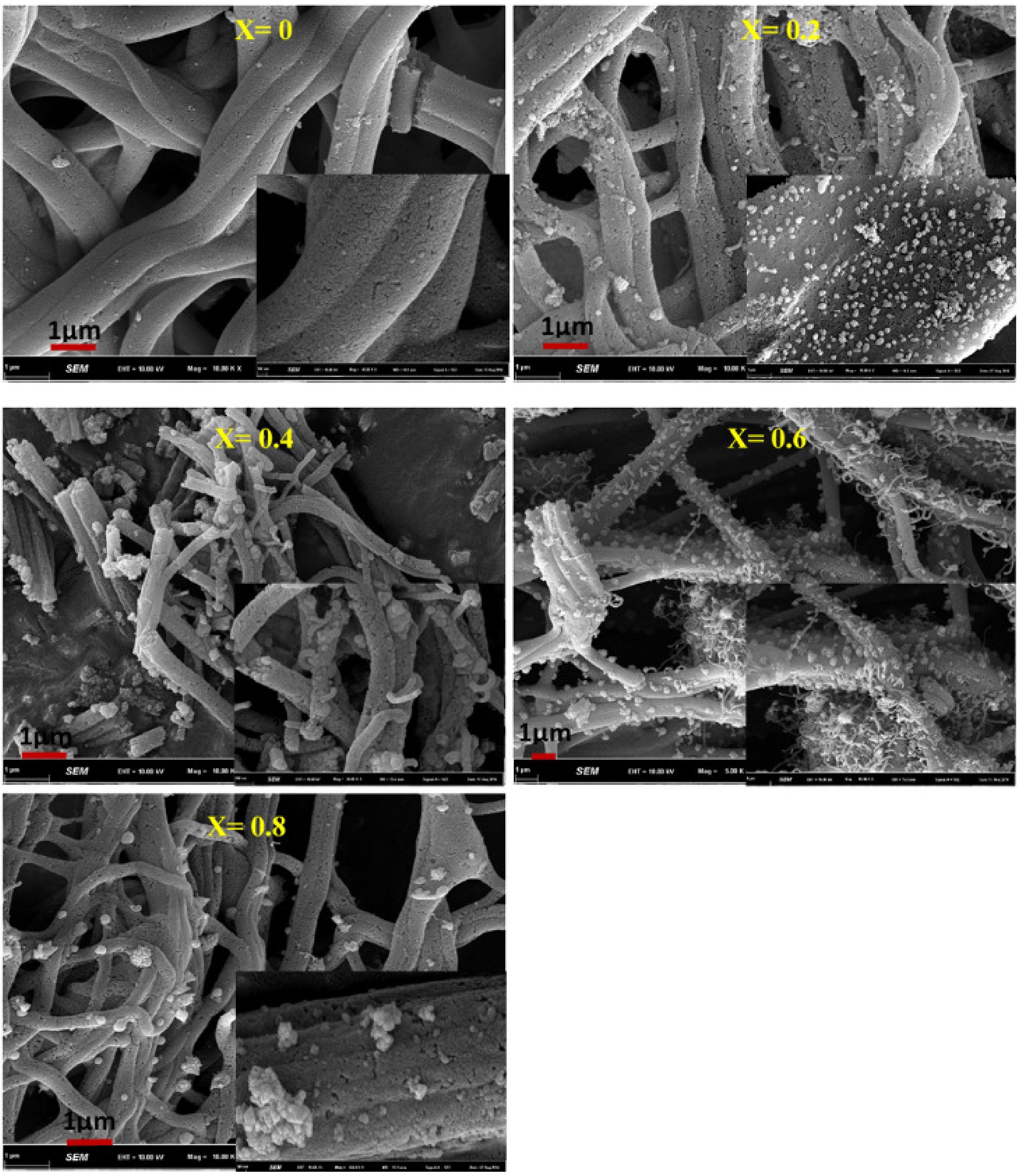

Fig. 4-11 FE-SEM micrographs of the ACNF/$Cu_xMn_{1-x}Fe_2O_4$ composite nanostructures.

Fig. 4-12 shows the surface XPS analysis for C1s, Cu2p, Fe2p, and Mn2p of all ACNF/$Cu_xMn_{1-x}Fe_2O_4$ nanostructures. The binding energy peak at 284.9 eV for C1s indicating to C-C bond [37] was observed for all prepared samples (Fig. 4-12 (a)). Two characteristic peaks of Cu($2p_{3/2}$) and Cu($2p_{1/2}$) at 932.3 and 952.3 eV, respectively (Fig. 4-12 (b)), were attributed to the presence of the Cu^{2+} chemical state on the surface of samples [54]. The sample x = 0.2 shows the shake-up satellite peaks of the Cu($2p_{3/2}$) and Cu $2p_{1/2}$ at 942.5 and 962.6 eV, respectively, confirming formation of Cu^{2+} on the surface [55]. Two main peaks at 710.9 and 724.5 eV are ascribed to the characteristic doublets of $Fe2p_{3/2}$ and $Fe2p_{1/2}$, respectively of Fe^{3+}. For the sample with x = 0.2, the satellite peak at 718.9 eV can be seen clearly and indicates that Fe is mainly in the Fe^{3+} state [40]. Two distinct peaks at binding energies of 642.2 and 653.6 eV attributed to the Mn(2p3/2) and Mn(2p1/2) of Mn^{2+} [56-57] were clearly seen for first two samples with largest Mn content (x = 0.0 and x = 0.2). No shift of the Mn2p peaks was observed indicating that the fraction of each Mn ion state does not change noticeably with Cu addition.

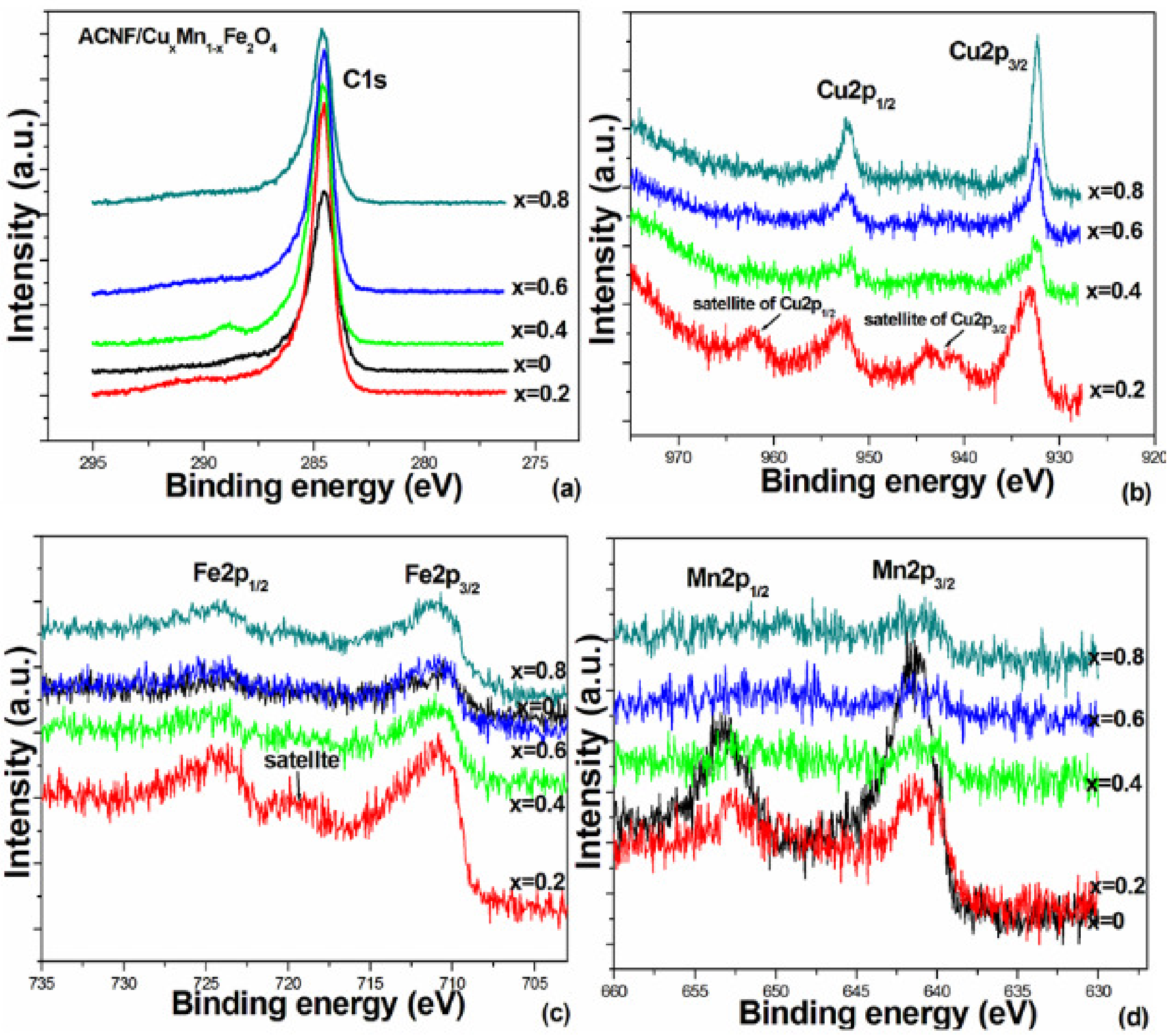

Fig. 4-12 XPS spectra of ACNF/$Cu_xMn_{1-x}Fe_2O_4$ composite nanostructures (a) C1s, (b) Cu2p (c) Fe2p, (d) Mn2p, and (e) O1s

To further verify the bulk oxidation state of Mn and Fe ion in $MnFe_2O_4$, the XANE spectra from XAS technique was used. Fig. 4-13 shows the first derivative XANE spectra at Fe and Mn K-edge. It was found, the Fe K-edge spectra for all samples are similar to that of Fe_2O_3 indicating Fe^{3+}. Meanwhile the edge energies of Mn are lay between MnO and Mn_2O_3 indicating to mixing of $Mn^{2+,3+}$.

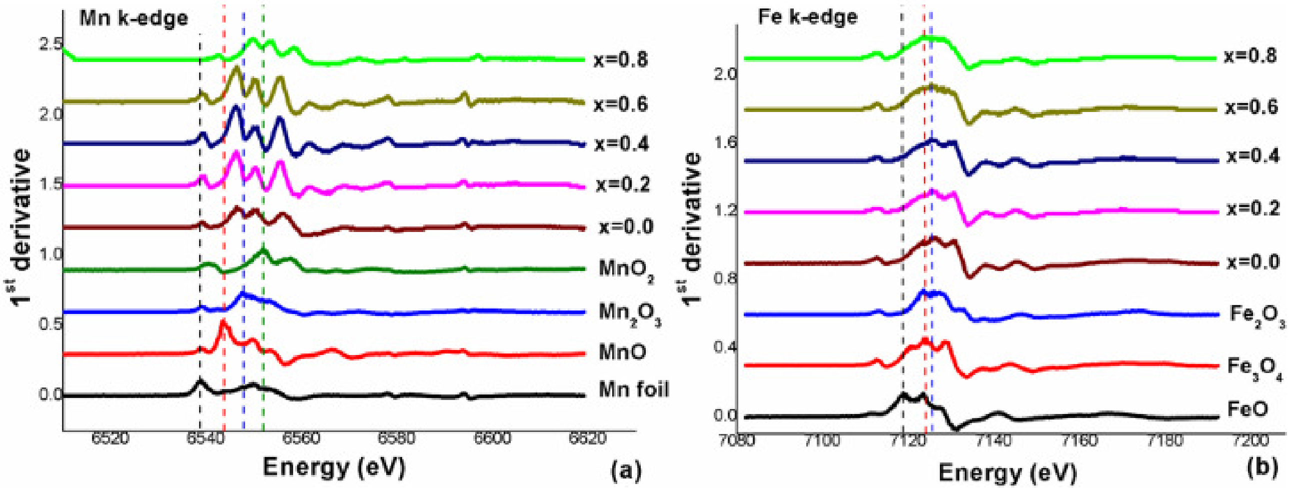

Fig. 4-13 The first derivative plots at Fe K-edge (a), and Mn K-edge (b)

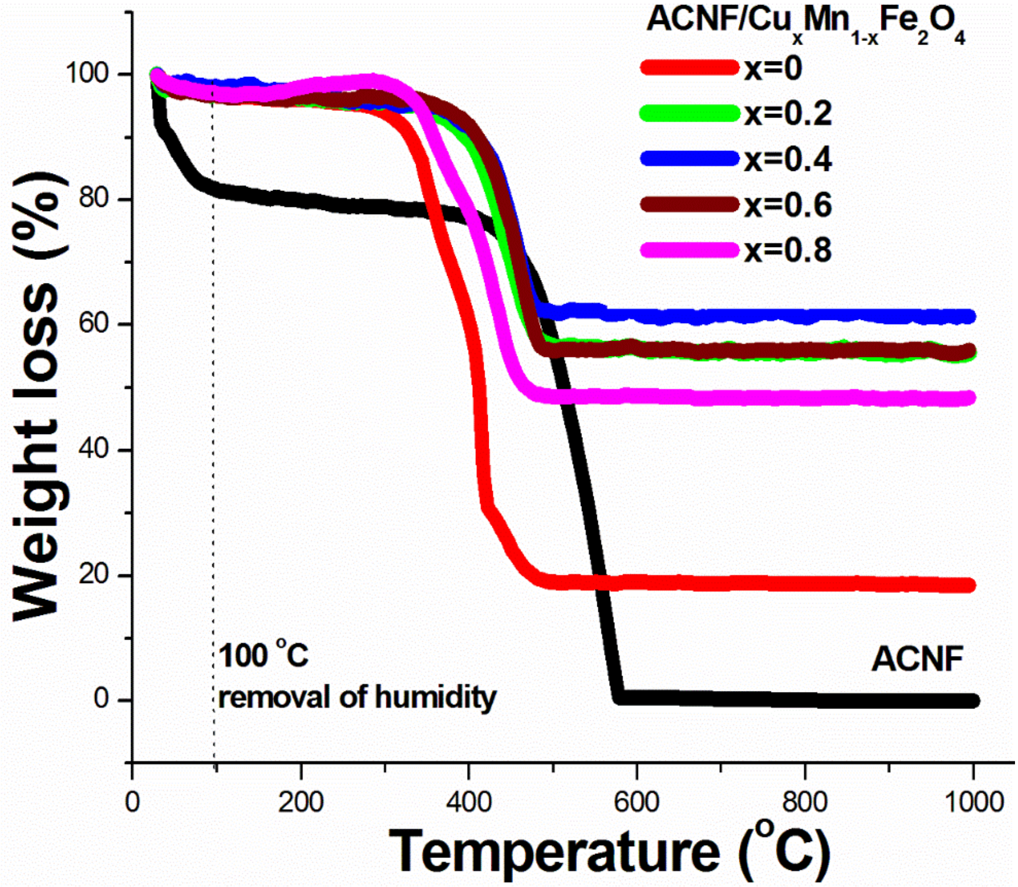

Fig. 4-14 TGA curves of CNF and ACNF/$Cu_xMn_{1-x}Fe_2O_4$ composite nanostructures

Fig. 4-14 shows TG curves for ACNF/ $Cu_xMn_{1-x}Fe_2O_4$ composite nanostructures. All prepared samples show two main step of weight loss at ~20-295 °C (minor) and ~295 - 570 °C (major), respectively. The minor weight loss corresponds to the loss of chemically absorbed water molecular and all trapped solvents. Whereas the major weight loss relate to the decomposition of metal nitrates along with the degradation of PAN polymer chain. The common plateau was observed after that, suggesting the presence of only pure inorganic contents. The weight percentage of $Cu_xMn_{1-x}Fe_2O_4$ loading in the composite nanostructures were determined from residue weight at 1000 ^{o}C. The values of 18.5, 57.2, 62.3 58.1 and 48.4% were observed for samples x= 0, 0.2, 0.4, 0.6 and 0.8, respectively. The corresponding contents of carbon are 78%, 42.3%, 35.9%, 38.8% and 48.8%, respectively. The sample x = 0.2 and 0.8 show nearly content of carbon and $CuMnFe_2O_4$ as those of samples with x = 0.4 and 0.6. As known that, EDLC is the source of energy storage for carbonaceous materials, while pseudocapacitance being for metal oxide systems. Therefore, the appropriate proportion residual content of carbon and $CuMnFe_2O_4$ may supporting high capacitance.

Fig. 4-15 shows the adsorption/ desorption isotherm for ACNF/ $Cu_xMn_{1-x}Fe_2O_4$ composite nanostructures. All isotherms are similar to the IV-type with H3 hysteresis suggesting mesopores (2-50 nm). The mean pore diameter of 3–10 nm based on the BJH method was observed [58]. The corresponding specific surface area (a_{bet}), total pore volumes (V), peak radius of pores (R_p), and mean pore diameter were presented as inset figures. The specific surface area for all samples exhibits higher value than that of 30-190 m^2/g for non-activated CNF in our previous work [59]. In electrochemical analysis, large surface provides high accessible of electrolyte ions and facilitates fast ions transfer between electrode and electrolyte, leading to a large capacity of the prepared electrode [60-61].

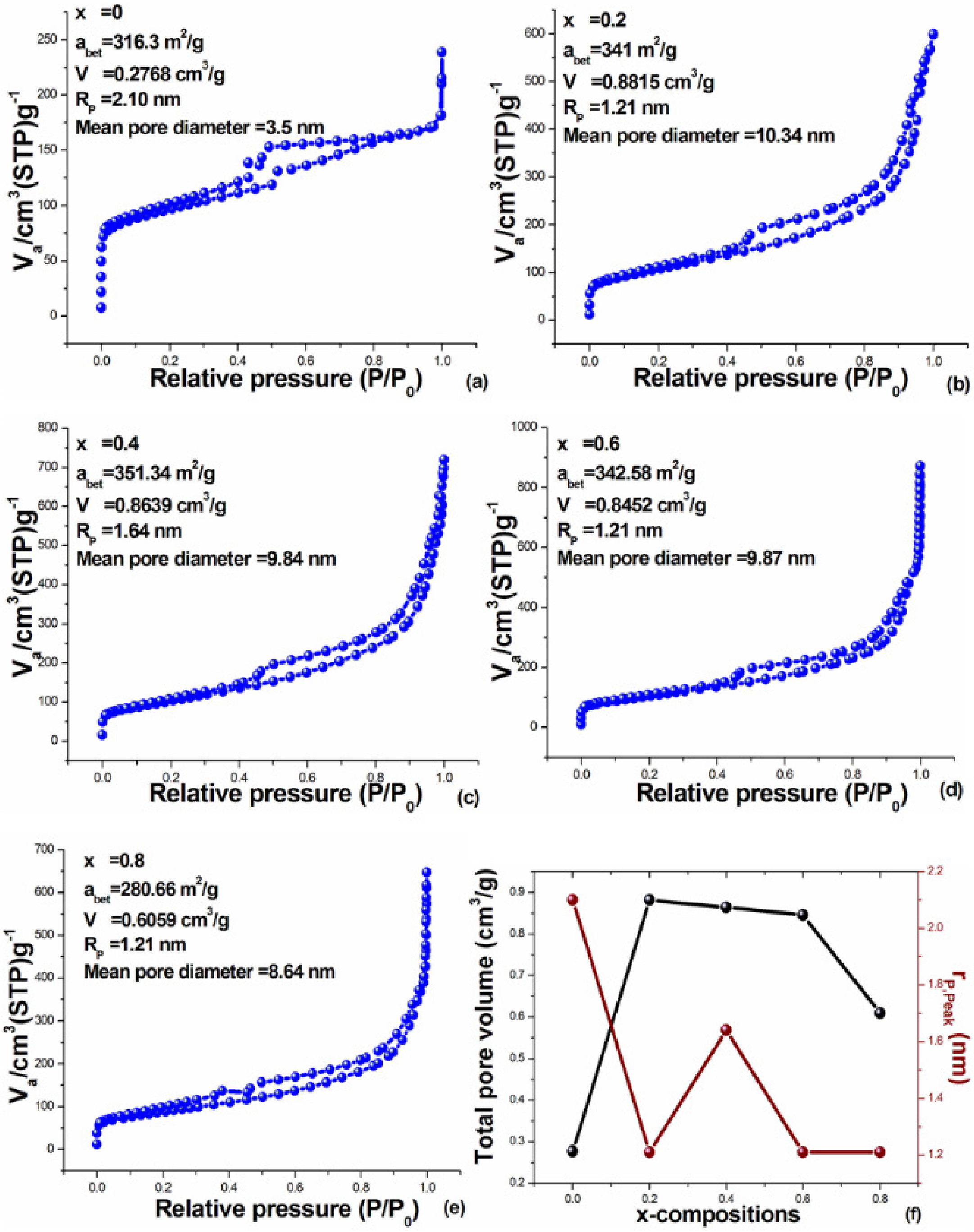

Fig. 4-15 (a-e) adsorption-desorption isotherm and (f) the corresponding pore volume and peak radius porosity

The electrochemical performance of the ACNF/$Cu_xMn_{1-x}Fe_2O_4$ was first examined by cyclic voltammetry (CV) at different scan rates of 2-200 mV/s (Fig. 4-16 (a)-(e)). It was found that the capacitive behavior was observed in the high potential range of -1.2 to 0.1V. The voltammetry current is directly proportional to the scan rate and the redox humps are seen due to pseudo-capacitive behavior. The samples x = 0.2 and 0.8 show clear the sharp anodic peak at -0.72 V (at 2 mV/s) than those other. This peak refer to the oxidation of metallic Cu, Mn, and Fe to CuO, MnO and Fe_2O_4, respectively. The shift of peak to higher potentials with the increase of scan rate may be due to the rearrangement of $CuMnFe_2O_4$ structure [46]. The specific capacitance (C_s) from CV was calculated according to the equation $C_s = \int IdV / m\nu V$ [62], where I is the current density, V is the potential, ν is the scan rate potential, and m is the active mass. The obtained capacitance values decreased with an increase of a scan rate (Fig. 4-16 (f)) suggesting the inaccessibility of electrolyte ions into surface of electrode at high charging/discharging rate [48]. At a scan rate of 2 mV/s, the C_s values of 175, 384, 140, 144 and 235 F/g were observed for samples x = 0.0, 0.2, 0.4, 0.6 and 0.8 respectively. The first two maximum values observed in samples with x = 0.2 and 0.8 correspond to their sharp redox peaks, which may be attributed to the insertion/de-insertion of electrolyte ions into their composite layered structures.

For a further understanding of the conductivity and interfacial charge transfer process at the electrode/electrolyte interface, the electrochemical impedance spectroscopy technique (EIS) was employed. Nyquist plots for ACNF/$Cu_xMn_{1-x}Fe_2O_4$ electrodes in 2M KOH electrolyte are shown in Fig. 4-17 (a). All electrodes show almost a straight line at low frequency with a small semicircle arc in the high frequency region. The sloping line in the low frequency region represented the frequency dependence of ion diffusion into the bulk of the electrode. The diameter of semicircle in the high frequency region represents charge transfer resistance (R_{ct}), greater the diameter manifesting low electrical conductivity. The R_{ct} values of 0.028, 0.033, 0.039, 0.036 and 0.035 Ω were observed for samples x = 0.0, 0.2, 0.4, 0.6 and 0.8, respectively. The values are closely similar to others reported in $MnCuFe_2O_4$/rGO [56] and become smaller compared with ACNF [63]. The real axis intercept represents the bulk solution resistance (R_s) [64-65]. Low values of 0.777, 0.854, 0.955, 0.952 and 0.938 Ω were obtained for the sample x = 0.0, 0.2, 0.4, 0.6 and 0.8, respectively. The enhancement of both resistance values after introducing of Cu is possibly due to the rougher surface causing the enlarged contact area and aggregation of the nanoparticles that may block the penetration of electrolyte ions.

The samples x=0.2 and 0.8 show lower R_s and R_{ct} values than those of samples x=0.4 and 0.6, indicating better conductivity. Fig. 4-17 (b) displays the Bode plots of frequency dependence of phase angle during 0.01 to 10^5 Hz. The phase angle decreases and close to zero with increasing of frequency. At frequency of 0.01 Hz, the phase angles of 72.93, 64.18, 73.60, 74.59, and 71.83 were obtained for x = 0.0, 0.2, 0.4, 0.6 and 0.8 electrodes, respectively. All values are not close to 90^o for ideal capacitors. The low phase angle values for the samples with x = 0.2 and x = 0.8 as compared to the other are an indication of more pseudocapacitive behavior [66]. The capacitor response frequencies at phase angle of 45 ^oC for x = 0.0, 0.2, 0.4, 0.6 and 0.8 electrodes are 0.64, 0.71, 1.39, 1.54, and 1.07 Hz, respectively. The corresponding relaxation time constant (τ_o = 1/ f_o) was calculated to be about 1.56, 1.41, 0.72, 0.65 and 0.93 s, respectively. The lower time constant of copper doping electrodes than that of the sample x = 0 supported faster charge-discharge [67]. Fig. 4-17 (c) shows galvanostatic charge/discharge (GCD) curves at a current density of 2 A/g. The nonlinear discharge curves indicate the capacitive behavior of prepared samples [68, 50]. The C_s value in F/g under the constant current discharge process were calculated based on the equations $C_s = I\Delta t_d / m\Delta V$, where I is the current density, Δt_d is the discharge time and ΔV is the voltage window. The sample x = 0.2 and 0.8 show higher C_s and energy density values than those of the sample x = 0.4 and 0.6 (Fig. 4-17 (d)), which is consistent to results already published elsewhere i.e. $Ni_xMn_{1-x}Fe_2O_4$ films electrode) [69] and $Ni_{1-x}Zn_xFe_2O_4$ [70]. To describe the electrochemical behavior, three parameters (surface area, conductivity and content of carbon and $CuMnFe_2O_4$) were considered. The conductivity is not directly measured in this work, but speculated from the Nyquist plot. It is worth noting from Table. 4 that, the C_s value does not depend directly on surface area, but seemed to depend on electrical conductivity and the residual amount of carbon and $CuMnFe_2O_4$. The samples with nearly proportional content between carbon and $CuMnFe_2O_4$ (x = 0.2 and x=0.8) exhibit higher C_s values than those other samples. Such high C_s value may be attributed to the synergistic effects on charge storage mechanism between two components of composite materials. It was believed that, the redox states for x=0.2 and 0.8 might be higher than those of x=0.4 and 0.6 and offer richer redox reactions, including contributions from all of Cu, Mn and Fe ions and thus maximizing surface charge accumulation.

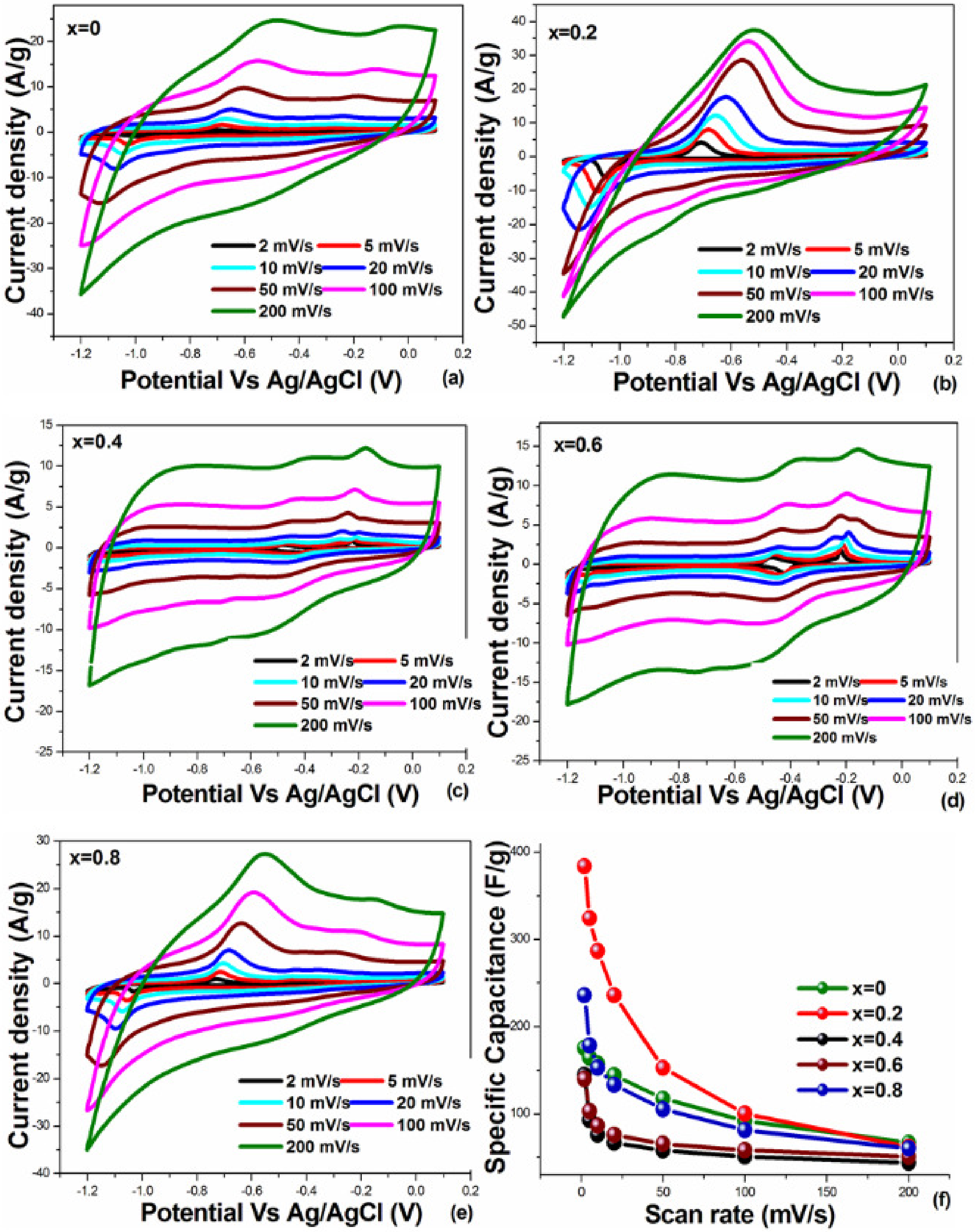

Fig. 4-16 (a-e) CV curve at scan rate of 2- 200 mV/s, and (f) the corresponding specific capacitance as function of scan rate

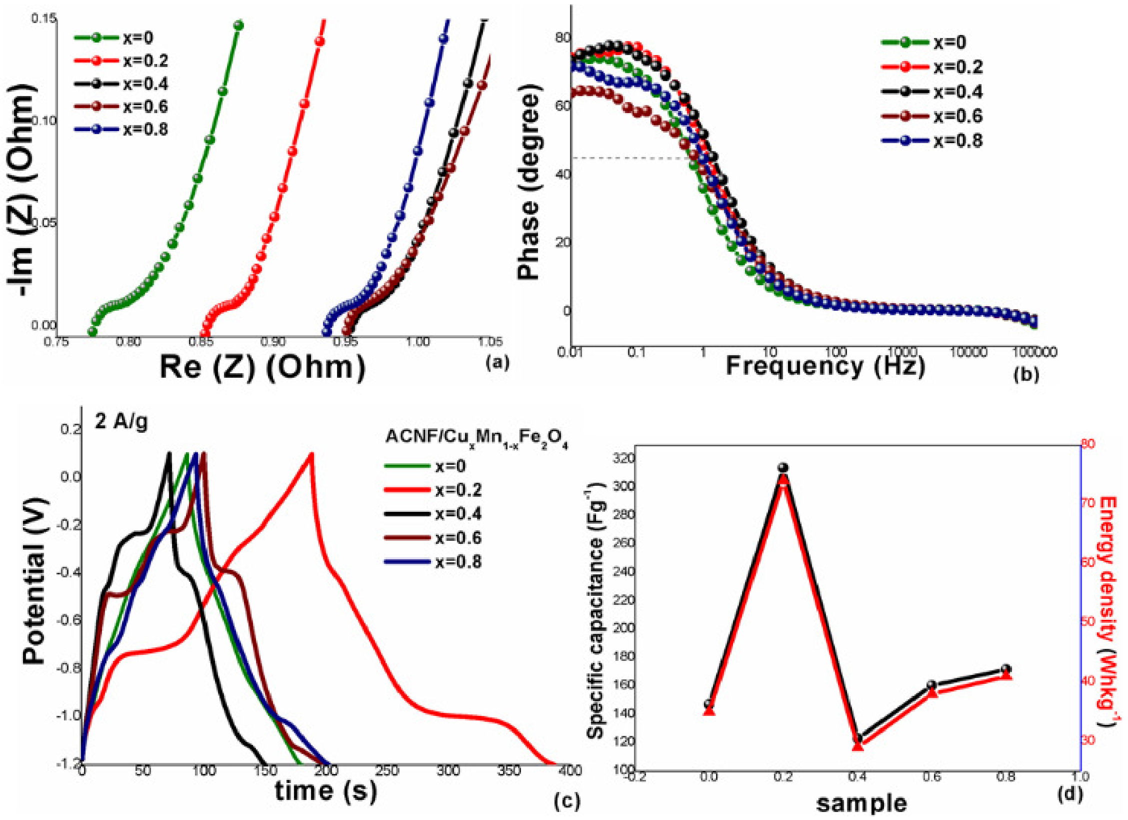

Fig. 4-17 (a) Nyquist plots at a frequency range of 0.01 Hz-100 kHz (b) the corresponding Bode plots of frequency dependence of phase angle (c) Galvanostatic charge/discharge spectra at 2 A/g (d) the corresponding specific capacitance and energy density of ACNF/$Cu_xMn_{1-x}Fe_2O_4$.

Fig. 4-18 (a) shows plot of the capacitance retention after repeated CV at a scan rate of 100 mV/s over 1000 cycles. The values of 80.74, 77.98, 73.88, 75.00 and 80.26% were observed for x=0.0, 0.2, 0.4, 0.6 and 0.8, respectively. The sample x=0 shows the best cycling stability may due to its maximum carbon content (Table. 4). That is, carbon matrix may working as elastic buffer structure and restricts the volume changes of electrode during charge/discharge process. The sample x=0.2 and 0.8 (with 42.3 and 48.8% of carbon, respectively) also show better stability than x=0.4 and 0.6 (with 35.9 and 38.8% of carbon, respectively). In addition, the variation trend of the capacity retention is almost opposite trend of the crystallite size (Fig. 4-18 (b)). Larger crystallite size for x=0.4 and 0.6 than those of x=0.2 and 0.8 means smaller specific surface area and thus may suppressed the interaction between the electrolyte ions and electrode. Moreover, large crystallite size may cause longer migration paths of electrolyte ions and thus reduced the capacity.

Whereas, too small crystallite size (as x=0) may implies more tortuous migration paths of electrolyte ions [71-72], increase the resistance for ions insertion, and thus decrease the capacity. The moderate crystallite size for samples x=0.2 and 0.8 improve the electrochemical performance. This observation is consistent to other studied of Li($Ni_{0.5}Co_{0.2}Mn_{0.3}$)O_2 [73].

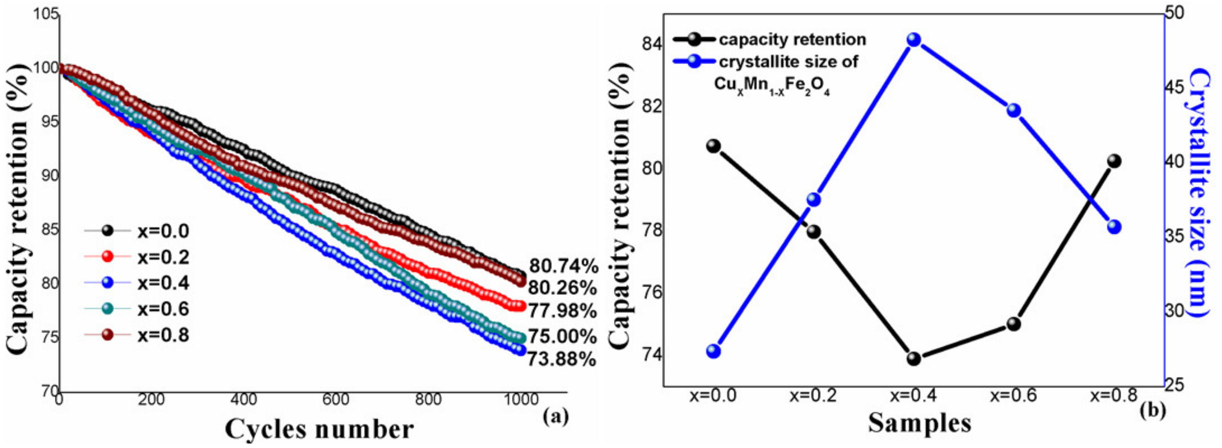

Fig. 4-18 the capacity retention at 1000 cycles (a) and the relationship between crystallite size and capacity retention

5. Conclusions

CNF/$MnFe_2O_4$ composite nanostructures were fabricated by electrospinning followed by carbonization process, while Activated carbon nanofibers composite with copper-manganese ferrite were fabricated by electrospinning followed carbonization and activation process, respectively. The obtained samples were characterized by means of X-ray diffraction (XRD), field emission scanning electron microscopy (FE-SEM), Brunauer-Emmett-Teller analyzer (BET), thermal gravimetric analysis (TGA), X-ray photoemission spectroscopy (XPS) and X-ray absorption spectroscopy (XAS). The electrochemical properties were investigated using cyclic voltammetry (CV), galvanostatic charge-discharge (GCD), and electrochemical impedance spectroscopy (EIS). For CNF/$MnFe_2O_4$ composite nanostructures, the effect of carbonization temperature on the structural, morphological, and electrochemical properties were investigated. By varying the carbonization temperature (500-700 ^{o}C), the crystallite size, surface area, residual content of $MnFe_2O_4$, and Mn ions in A-site increased with increasing of carbonization temperature. These values reach a maximum at 700 ^{o}C, giving rise to a superior capacitance to those in others. The maximum C_S value of 345 Fg^{-1} at 2 mV/s (using CV scan) and 291.9 Fg^{-1} at 5 Ag^{-1} (using galvanostatic discharge) are achieved. The superior capacitance may arise from (i) the presence of the largest crystallite size appears dramatically to alter the surface area and electroconductivity (ii) the maximum surface area supported a large number of sites for electrolyte ions penetration, resulting in an improved EDLC (iii) the smallest size of prepared fibers offers shortens charge diffusion length for electrons/ions diffuse into the matrix of CNFs (iv) the highest residual content of $MnFe_2O_4$ offer high pseudocapacitance through Faradaic reactions (v) lower equivalent series resistances giving rise to higher current density. Moreover, the occupation of Mn cations in A-site may significant dominant contribution in determining the pseudocapacitive performance of $MnFe_2O_4$. For the second group of ACNF/ $Cu_xMn_{1-x}Fe_2O_4$ composite nanostructures, by varying molar content between copper and manganese precursor (ACNF/$Cu_xMn_{1-x}Fe_2O_4$: x = 0.0, 0.2, 0.4, 0.6, 0.8), the cyclic stability strongly depends on the amount of carbon. The samples with x=0.2 and 0.8 exhibit higher capacity than those of the samples with x=0.4 and 0.6. These two of samples provided low resistivity, moderate and nearby crystallite size, and similarly residual content between $CuMnFe_2O_4$ and ACNF. Moreover, the superior capacitance may be attributed to the synergetic effect between pseudocapacitance of $CuMnFe_2O_4$ and EDLC of ACNF.

References

[1] H. Wang, L.F. Cui, Y. Yang, H.S. Casalongue, J.T. Robinson, Y. Liang, Y. Cui, H.J. Dai. (2010). Mn_3O_4-Graphene hybrid as a high-capacity anode materil for Lithium ion batteries. J. Am. Chem. Soc. 132: 13978.

[2] P.G. Bruce, B. Scrosati, J.M. Tarascon. (2008). Nanomaterials for rechargeable lithium batteries. Angew. Chem., Int. Ed. 47: 2930.

[3] C. Largeot, C. Portet, J. Chmiola, P. Taberna, Y. Gogotsi and P. Simon. (2008). Relation between the Ion Size and Pore Size for an Electric Double-Layer Capacitor. J. Am. Chem. Soc. 130: 2730.

[4] S. Kandalkar, D. Dhawale, C. Kim and C. Lokhande. (2010). Chemical synthesis of cobalt oxide thin film electrode for supercapacitor application. Synth. Met. 160: 1299.

[5] M. Winter, R.J. Brodd, (2004). What are batteries, fuel cells, and supercapacitors. Chem. Rev. 104, 4245.

[6] H.R. Ghenaatian, M.F. Mousayi, M.S. Rahmanifar, (2011). High performance battery-super Capacitor hybrid energy storage system based on self-doped polyaniline nanofibers. Synth. Met. 161, 2017-2023.

[7] V. Gupta, N. Miura, (2005). Electrochemically deposited polyaniline nanowire's network. A high-performance electrode material for redox supercapacitor. Solid State Lett. 8, A630 (2005).

[8] H. Wang, Y. Wang, X. Wang, Pulsed laser deposition of large-area manganese oxide nanosheet arrays for high-rate supercapacitors, New J. Chem. 37 (2013) 869-872

[9] G.H. Yue, Y.C. Zhao, C.G. Wang, X.X. Zhang, X.Q. Zhang, Q.S. Xie, (2015) Flower-like nickel oxide nanocomposites anode materials for excellent performance lithium ion batteries. Electrochim. Acta 152, 315–322.

[10] K. Wang, X. Dong, C. Zhao, X. Qian, Y. Xu, Facile synthesis of Cu_2O/CuO/RGO nanocomposite and its superior cyclability in supercapacitor, Electrochim. Acta 152 (2015) 433-442.

[11] P.M. Kulal, D.P. Dubal, C.D. Lokhande, V.J. Fulari, Chemical synthesis of Fe_2O_3 thin films for supercapacitor application, J. Alloys Compd. 509 (2011) 2567-2571.

[12] D. Carta, M.F. Casula, A. Falqui, D. Loche, G. Mountjoy, C. Sangregorio, A. Corrias, A structural avnd magnetic investigation of the inversion degree in ferrite nanocrystals MFe_2O_4 (M = Mn, Co, Ni), J. Phys. Chem. C, 113 (2009) 8606-8615

[13]. Y.H. Jin, S.D. Seo, H.W. Shim, K.S. Park and D.W. Kim. (2012). Synthesis of core/shell spinel ferrite/carbon nanoparticles with enhanced cycling stability for lithium ion battery anodes. Nanotechnology. 23: 125402.

[14] Q.H. Wang, L.F. Jiao, H.M. Du, Y.J. Wang, and H.T. Yuan. (2014). Fe_3O_4 nanoparticles grown on graphene as advanced electrode materials for supercapacitors. J. Power Sources. 245: 101-106.

[15] D. Porter, B. Denizot, E. Rump, J. Lejeune, P. Jallet. (2001). Nonpolymeric coating of iron oxide colloids for biological use as magnetic resonance imaging contrast agents. J. Colloid Interf. Sci. 238: 37-42.

[16] J.B. Haun, T.J. Yoon, H. Lee, R. Weissleder. (2010). Magnetic nanoparticle biosensors, Wiley Interdiscip. Rev. Nanomed. Nanobiotechnol. 2: 291-304.

[17] I. Brigger, C. Dubernet, P. Couvreur. (2002). Nanoparticles in cancer therapy and diagnosis, Adv. Drug Delivery Rev. 54: 631-651.

[18] J. Wang, Q.W. Chen, B.Y. Hou, Z.M. Peng. (2004). Synthesis and magnetic properties of single crystals of $MnFe_2O_4$ nanorods. Eur. J. Inorg. Chem. 6: 1165-1168.

[19] P.Z. Guo, G.L. Zhang, J.Q. Yu, H.L. Li, X.S. Zhao. (2012). Controlled synthesis, magnetic and photocatalytic properties of hollow spheres and colloidal nanocrystal clusters of manganese ferrite. Colloids Surf. A: Physicochem. Eng. Aspects. 395: 168-174.

[20] H.M. Fan, J.B. Yi, Y. Yang, K.W. Kho, H.R. Tan, Z.X. Shen, J. Ding. X.W. Sun, M.C. Olivo, Y.P. Feng. (2009). Single crystalline MFe_2O_4 nanotubes/nanorings synthesized by thermal transformation process for biological applications, ACS Nano 3: 2798-2808.

[21] M.H. Mahmoud, H.H. Hamdeh, J.C. Ho, M.J. O'Shea, J.C. Walker. (2000). Mossbauer studies of manganese ferrite fine particles processed by ball-milling. J. Magn Magn Mater. 220(2-3): 139-46.

[22] M. Muroi, R. Street, P.G. McCormick, J. Amighian. (2001). Magnetic properties of ultrafine $MnFe_2O_4$ powders prepared by mechanochemical processing. Phys Rev B. 63: 184414.

[23] N.S. Gajbhiye, G. Balaji. (2000). Synthesis, reactivity, and cations inversion studies of nanocrystalline $MnFe_2O_4$ particles. Thermochim Acta. 385(1-2): 143-51.

[24] L.J. Cui, P.Z. Guo, G.L. Zhang, Q. Li, R.Y. Wang, M. Zhou, L.N. Ran, X.S. Zhao. (2013). Facile synthesis of cobalt ferrite submicrospheres with tunable magnetic and electrocatalytic properties, Colloids Surf., A: Physicochem. Eng. Aspects. 423: 170-177.

[25] A.J. Han, J.J. Liao, M.Q. Ye, Y. Li, X.H. Peng. (2011). Preparation of nano- $MnFe_2O_4$ and its catalytic performance of thermal decomposition of ammonium perchlorate. Chin. J. Chem. Eng. 19: 1047-1051

[26] S.D. Sartale, C.D. Lokhande. (2005). A room temperature two-step electrochemical process for large area nanocrystalline ferrite thin films deposition. J. Electroceram. 15: 35-44.

[27] S. Sun, H. Zeng, D. B. Robinson, S. Raoux, P. M. Rice, S. X. Wang, and G. Li, (2004). Monodisperse MFe_2O_4 (M = Fe Co, Mn) nanoparticles. J. Am. Chem. Soc. 126(1) 273.

[28] K. Vijaya Sankar and R. Kalai Selvan. The ternary MnFe2O4/graphene/polyaniline hybrid composite as negative electrode for supercapacitors. J. Power Sources. 275 (2015) 399-407.

[29] M.S.A. Rahaman, A.F. Ismail, A. Mustafa, (2007) A review of heat treatment on polyacrylonitrile Polym Degrad Stab. 92, 1421-1432.

[30] D. Zhu, C. Xu, N. Nakura, M. Matsuo, (2002), study of carbon films from PAN/VGCF composites by gelation/crystallization from solution. Carbon 40, 363-373.

[31] H. P. Klug, L. E. Alexander, X-ray Diffraction Procedures for Polycrystalline and amorphous materials, second ed., Wiley-Interscience, New York, 1974.

[32] W. Wang, P. Liu, M. Zhang, J. Hu, F. Xing, (2012) The pore structure of phosphor aluminate cement, Open J. Compos. Mater. 2: 104-112.

[33]. B. Zhang, F. Kang, J.M Tarascon, J.K. Kim, (2016) Recent advances in electrospun carbon nanofibers and their application in electrochemical energy storage, Prog. Mater Sci. 76: 319-380.

[34] Y.J. Yao, Y.M. Cai, F. Lu, F.Y. Wei, X.Y. Wang, S.B. Wang, (2014) Magnetic recoverable $MnFe_2O_4$ and $MnFe_2O_4$ -graphene hybrid as heterogeneous catalysts of peroxymonosulfate activation for efficient degradation of aqueous organic pollutants, J. Hazard. Mater. 270: 61-70.

[35] C. V. Ramana, M. Massot, and C. M. Julien, (2005) XPS and Raman spectroscopic characterization of $LiMn_2O_4$ spinels, Surf. Interface Anal. 37 (4): 412–416.

[36] M. Zong, Y. Huang, H.W. Wu, Y. Zhao, S.Q. Wang, N. Zhang, W. Zhang, (2013) Facile synthesis of RGO/Fe_3O_4/Ag composite with high microwave absorption capacity, Mater. Lett. 111 188-191.

[37] J. Xiao, G. Xu, S.G. Sun, and S. Yang, (2013) MFe_2O_4 and MFe@Oxide core–shell nanoparticles anchored on N-doped graphene sheets for synergistically enhancing lithium storage performance and electrocatalytic activity for oxygen reduction reactions, Part. Part. Syst. Char. 30: 893-904.

[38] B.J. Li, H.Q. Cao, J. Shao, M.Z. Qu, (2011) Enhanced anode performances of the Fe_3O_4-Carbon-rGO three dimensional composite in lithium ion batteries, Chem. Commun. 47 10374-10376.

[39] M. Vijayaraj and C.S. Gopinath, (2006) "On the "Active spacer and stabilizer" role of Zn in $Cu_{1-x}Zn_xFe_2O_4$ in the selective mono-N-methylation of aniline: XPS and catalysis study," J. Catal. 241 (1) 83-95.

[40] D.D. Hawn, B.M. DeKoven, (1987) Deconvolution as a correction for photoelectron inelastic energy losses in the core level XPS spectra of iron oxides, Surf. Interface Anal, 10 63.

[41] L.L. Hench, and J.K. West, Principles of electronic ceramics. New York: John Wiley and Sons, 1990.

[42]. J.M. Hastings and L.M. Corliss, (1956) Neutron Diffraction Study of Manganese Ferrite, Phys. Rev. 104 328.

[43] C. Wei, Z. Feng, M. Baisariyev, L. Yu, L. Zeng, T. Wu, H. Zhao,Y. Huang, M. J. Bedzyk, T. Sritharan, and Z.J. Xu, (2016) Valence change ability and geometrical occupation of substitution cations determine the pseudocapacitance of spinel ferrite XFe_2O_4 (X= Mn, Co, Ni, Fe), Chem. Mater. 28: 4129-4133.

[44] Z.B. Wen, Q.T. Qu, Q. Gao, Z.H. Hu, Y.P. Wu, X.W. Zheng, Y.F. Liu, and X.J. Wang, (2009). An activated carbon with high capacitance from carbonization of a resorcinolformaldehyde resin, Electrochem. Commun, 11: 715-718.

[45] Q.T. Qu, B. Wang, L.C. Yang, Y. Shi, S. Tian, and Y.P. Wu, (2008) Electrochemical performance of MnO_2 nanorods in neutral aqueous electrolytes as a cathode for asymmetric supercapacoitors. Electrochem. Commun, 10: 1625-1655.

[46] B. Bashir, W. Shaheen, M. Asghar, M.F. Warsi, M.A. Khan , S. Haider, I. Shakir, M. Shahid, (2017). Copper doped manganese ferrites nanoparticles anchored on graphene nano-sheets for high performance energy storage applications, J. Alloys Compd. 695: 881-887.

[47] W. Tang, L.L. Liu, Y.S. Zhu, H. Sun, Y.P. Wu, and K. Zhu, (2012) An aqueous rechargeable lithium battery of excellent rate capability based on a nanocomposite of MoO_3 coated with PPy and $LiMn_2O_4$. Energy Environ Sci. 5: 6909.

[48] J. Li, D.B. Le, P.P. Ferguson, J.R. Dahn, (2010) Lithium polyacrylate as a binder for tin–cobalt-carbon negative electrodes in lithium-ion batteries, Electrochim. Acta, 55: 2991.

[49] Manohar K. Zatea, Vijaykumar V. Jadhava, Shyam K. Gorea, Janardhan H. Shendkara, Satish U. Ekare, Ahmed Al-Ostaa, Mu. Naushadc, Rajaram S. Mane, (2016) Structural, morphological and electrochemical supercapacitive properties of sprayed manganese ferrite thin film electrode. J. Anal. Appl. Pyrol, 122: 224-229.

[50] X. Liu, L. Zhou, Y. Zhao, L. Bian, X. Feng, Q. Pu, (2013) Hollow, spherical nitrogen-rich porous carbon shells obtained from a porous organic framework for the supercapacitor, ACS Appl. Mater. Interfaces 5: 10280-10287.

[51] B. Zhang, Y. Yu, Z.L. Xu, S. Abouali, M. Akbari, Y.B. He, F. Kang, J.K. Kim, (2014). Correlation between atomic structure and electrochemical performance of anodes made from electrospun carbon nanofiber films, Adv. Energy Mater. 4: 1301448.

[52] S.G. Khandalkar, H.M. Lee, H. Chae, C.K. Kim, (2011) Structural, morphological andelectrical characteristics of the electrodeposited cobalt oxide electrode forsupercapacitor applications, Mater. Res. Bull. 46: 48-51.

[53] M. Kunowsky, J.P. Marco-Lozar, A. Oya, (2012). Linares-Solano, Hydrogen storage in Co_2-activated amorphous nanofibers and their monoliths, Carbon. 50: 1407.

[54] G. H. Yue, Y. Zhang, X. Q. Zhang, C. G. Wang Y. C. Zhao, D. L. Peng, (2015). Synthesis of Cu2O mesocrystal and its application in photocatalysis. Appl. Phys. A 118: 763–767.

[55] C.C. Chusuei, M.A. Brookshier and D.W. Goodman, Correlation of Relative X-ray Photoelectron Spectroscopy Shake-up Intensity with CuO Particle Size, Langmuir. 15 (1999) 2806-2808.

[56] X.Y. Longa, J.Y. Lia, D. Shenga, H.Z. Liana, (2017), Spinel-type manganese ferrite ($MnFe_2O_4$) microspheres: A novel affinity probe for selective and fast enrichment of phosphopeptides, Talanta. 166: 36–45.

[57] T. Simsek, S. Akansel, S. Ozcan, A. Ceylan, Synthesis of $MnFe_2O_4$ nanocrystals by wet milling under atmospheric conditions, Ceram. Int. 40: 7953-7956.

[58] Y.W. Ju, G.R. Choi, H.R. Jung, W.J. Lee, (2008) Electrochemical properties of electrospun PAN/MWCNT carbon nanofibers electrodes coated with polypyrrole, Electrochim Acta. 53: 5796.

[59] S. Nilmoung, T. Sinprachim, I. Kotutha, P. Kidkhunthod, R. Yimnirun, S. Rujirawat, S. Maensire, (2016). Electrospun carbon/ $CuFe_2O_4$ composite nanofibers with improved electrochemical energy storage performance, J. Alloys Compd, 688: 1131-1140.

[60] H. Wang, Q. Gao, J. Hu, (2010) Preparation of porous doped carbons and the high performance in electrochemical capacitors, Microporous Mesoporous Mater. 131: 89–96.

[61] X.J. Zhu, Y.W. Zhu, S. Murali, M.D. Stoller, and R.S. Ruoff, (2011). Nanostructure reduced graphene oxide/ Fe_2O_3 composite as a high performance anode material for lithium ion batteries. ACS Nano. 5: 3333.

[62] B.E. Conway, Electrochemical supercapacitors: Scientific Fundamentals and technological application, Plenum Press, New York, 1999.

[63] J.E. Yang, I. Jang, M. Kim, S.H. Baeck, S. Hwang, S.E. Shim, (2013) Electrochemically polymerized vine-like nanostructured polyaniline on activated carbon nanofibers for supercapacitor, Electrochim Acta. 111: 136–143.

[64] V. Khomenko, E. Raymundo-Pinero, E. Frackowiak, and F. Beguin, (2006). High voltage asymmetric supercapacitors operating in aqueous electrolyte. Appl. Phys. A. 82: 567-73.

[65] J.G. Wang, Y. Yang, Z.H. Huang, and F. Kang, (2012) Interfacial synthesis of mesoporous MnO_2/ polyaniline hollow spheres and their application in electrochemical capacitors, J. Power Sources. 204: 236-43.

[66] K. Krishnamoorthy, G. Veerasubramani, S. Radhakrishnan, and S.J. Kim, (2014). Supercapacitve behavior of hydrothermally synthesized flower like MoS_2 Nanostructures. Mater. Res. Bull. 50: 499-502.

[67] T.C. Girija, and M.V. Sangaranarayanan, (2006). Analysis of polyaniline based nickel electrodes for electrochemical capacitors. J. Power Sources. 156 (2006) 705.

[68] X. Yang, D. Wu, X. Chen, R. Fu, (2010). Nitrogen-enriched nanocarbons with a 3-D continuous mesopore structure from polyacrylonitrile for supercapacitor application, J. Phys. Chem. C 114: 8581–8586.

[69] Manohar K. Zate, Shoyeb Mohamad F. Shaikh, Vijaykumar V. Jadhav, Kailas K. Tehare, S.S. Kolekar, Rajaram S. Mane, Mu. Naushad, B.N. Pawar, K.N. Hui, (2015).Synthesis and electrochemical supercapacitive performance of nickel–manganese ferrite composite films. J Anal Appl Pyrolysis. 116: 177–182.

[70] D.K. Pawar, S.M. Pawar, P.S. Patil, S.S. Kolekar, (2011).Synthesis of nanocrystalline nickel-zinc ferrite ($Ni_{0.8}Zn_{0.2}Fe_2O_4$) thin films by chemical bath deposition method. J. Alloys Compd. 509: 3587-3591.

[71] S.B. Waje, M. Hashim, W.D.W. Yusoff, Z. Abbas, (2010). X-ray diffraction studies on crystallite size evolution of CoFe2O4 nanoparticles prepared using mechanical allyoying and sintering. Appl. Surf. Sci. 256 (10), 3122–31.

[72] A. Eftekhari, (2017). Ordered mesoporous materials for lithium ion batteries. Microporous Mesoporous Mater. 243, 355–369.

[73] G. Fan, Y. Wen, B. Liu, W. Yang, (2018). J Nanopart Res. 20, 43.

Output จากโครงการวิจัยที่ได้รับทุนจาก สกว.

1. ผลงานตีพิมพ์ในวารสารวิชาการนานาชาติ (ระบุชื่อผู้แต่ง ชื่อเรื่อง ชื่อวารสาร ปี เล่มที่ เลขที่ และหน้า) หรือผลงานตามที่คาดไว้ในสัญญาโครงการ
   - Sukanya Nilmoung, Somchai Sonsupap, Montree Sawangphruk, Santi Maensiri. Fabrication and electrochemical properties of activated CNF/$Cu_xMn_{1-x}Fe_2O_4$ composite nanostructures. Applied Physics A 124 (2018) 427
   - Sukanya Nilmoung, Pinit Kidkhunthod, and Santi Maensiri. The structural and electrochemical properties of CNF/$MnFe_2O_4$ composite nanostructures for supercapacitors. Materials chemistry and physics 220 (2018) 190-200
2. การนำผลงานวิจัยไปใช้ประโยชน์
   - เชิงวิชาการ (มีการพัฒนาการเรียนการสอน/สร้างนักวิจัยใหม่)
3. การเสนอผลงานในที่ประชุมวิชาการ
   - Sukanya Nilmoung’, Kanok-on Ritdon, Pattiya Srikeaw, Pornpis Kongphutorn’ and Santi Maensiri “Fabrication and Electrochemical properties of CNF/MFe_2O_4: (M = Mn, CuMn) Composite Nanofiber for Electrochemical capacitors” ในงานประชุมวิชาการนานาชาติ Nano Thailand 2016 ครั้งที่ 5 (The 5th Thailand International Nanotechnology Conference 2016) ซึ่งจัดขึ้น ในวันที่ 27-29 พฤศจิกายน 2559 ณ โรงแรมเดอะกรีนเนอรี่ รีสอร์ท เขาใหญ่ จ. นครราชสีมา

ภาคผนวก

Applied Physics A (2018) 124:427
https://doi.org/10.1007/s00339-018-1839-3

Applied Physics A
Materials Science & Processing

Fabrication and electrochemical properties of activated CNF/$Cu_xMn_{1-x}Fe_2O_4$ composite nanostructures

Sukanya Nilmoung[1] · **Somchai Sonsupap**[2] · **Montree Sawangphruk**[3] · **Santi Maensiri**[2]

Received: 1 March 2018 / Accepted: 7 May 2018

Abstract

This work reports the fabrication and electrochemical properties of activated carbon nanofibers composited with copper manganese ferrite (ACNF/$Cu_xMn_{1-x}Fe_2O_4$: $x=0.0$, 0.2, 0.4, 0.6, 0.8) nanostructures. The obtained samples were characterized by means of X-ray diffraction, field emission scanning electron microscopy, Brunauer–Emmett–Teller analyzer, thermal gravimetric analysis, X-ray photoemission spectroscopy, and X-ray absorption spectroscopy. The supercapacitive behavior of the electrodes is tested using cyclic voltammetery, galvanostatic charge–discharge and electrochemical impedance spectroscopy. By varying '*x*', the highest specific capacitance of 384 F/g at 2 mV/s using CV and 314 F/g at 2 A/g using GCD are obtained for the $x=0.2$ electrode. The second one of 235 F/g at 2 mV/s using CV and 172 F/g at 2 A/g using GCD are observed for $x=0.8$ electrode. The corresponding energy densities are 74 and 41 Wh/kg, respectively. It is observed that the cyclic stability of the prepared samples strongly depend on the amount of carbon, while the specific capacitance was enhanced by the sample with nearly proportional amount between carbon and $CuMnFe_2O_4$. Such results may arise from the synergetic effect between $CuMnFe_2O_4$ and ACNF.

1 Introduction

With the increasing demand of world energy consumption, supercapacitors are an important choice for energy storage systems due to their typically higher energy density than conventional capacitors and higher power density than batteries [1, 2]. They are widely used as a power source even for consumer electronics, memory back-up systems, electric vehicles, etc. [3–5]. According to their charge storage mechanism, supercapacitors are classified into electrical double layer capacitors (EDLCs) and pseudo-capacitors. Typically, a pseudo-capacitor (based on metal oxide or conducting polymers) exhibits greater capacitance value than EDLCs (based on carbon materials) because their charge storage occurs through surface redox reaction, while EDLCs store energy by accumulating electrostatic charge at the electrode/electrolyte interface. To date, a variety of transition metal oxides such as RuO_2 [6], MnO_2 [7], NiO [8], CuO [9], and Fe_3O_4 [10] have been used as electrode materials due to their pseudo-capacitances. Spinel ferrite material (MFe_2O_4:M is divalent transition metal) is metal oxide with spinel structure that also has been studied extensively. The unit cell of MFe_2O_4 is formed by 56 atoms with the 32 oxygen anions distributed in a cubic close packed structure. The 24 cations occupy 8 of the 64 available tetrahedral sites and 16 of the 32 available octahedral sites [11]. Previous studies on spinel ferrites focused intensively on their magnetic properties because the unpaired electron spins of Fe^{2+} in octahedral sites strongly affected the different magnetic properties [12, 13]. Currently, many studies are focused on their electrochemical performance [14, 15]. Manganese ferrite ($MnFe_2O_4$) is a cubic spinel ferrite materials that possesses stability in electrochemical [16] and contains multi oxidation state that favors the electrochemical reactions very positively [17]. However, bare $MnFe_2O_4$ possesses high electrical resistivity making impractical in energy storage device. Nevertheless, materials scientists try to improve electrochemical properties with various methods including synthesizing particles in nano-scale size, doping

---

✉ Sukanya Nilmoung
sukanya.ni@rmuti.ac.th

[1] Department of Applied Physics, Faculty of Sciences and Liberal Arts, Rajamangala University of Technology Isan, Nakhon Ratchasima 30000, Thailand

[2] School of Physics, Institute of Science, Suranaree University of Technology, Nakhon Ratchasima 30000, Thailand

[3] Department of Chemical and Biomolecular Engineering, School of Energy Science and Technology, Vidyasirimedhi Institute of Science and Technology, Rayong 21210, Thailand

2^+ or 3^+ valence state metals, or combined with carbon materials [17–21]. Moreover, there are various papers which have reported the improvement of energy density after adding $MnFe_2O_4$ into a carbon matrix [20, 22, 23]. However, the capacitance value is still low for applications and needs to be improved. Low capacitance may arise from low surface area of non-activated carbon and low electrical conductivity of $MnFe_2O_4$ nanoparticles.

Herein, activated carbon nanofibers composited with copper–manganese ferrite (ACNF/$CuMnFe_2O_4$) nanostructures are fabricated using an electrospinning process followed by a carbonization and activation process. By varying the molar ratio of two divalent metal Cu_x and Mn_{1-x} ($x=0.0$, 0.2, 0.4, 0.6, and 0.8), the capacitive behavior of ACNF/$Cu_xMn_{1-x}Fe_2O_4$ has been investigated.

2 Experimental

2.1 Materials

Polyacrylonitrile (PAN, MW 150,000, Sigma-Aldrich), *N,N*-dimethylformamide anhydrous (DMF, 99.8%, SIAL), copper (II) nitrate trihydrate [98.0–103% (RT), Sigma-Aldrich], Manganese (II) nitrate hydrate (99.99%, Aldrich), iron (III) nitrate nanohydrate (99.9%, Kento) were used as the precursor substance. Whereas, potassium hydroxide (99.99%, Sigma-Aldrich) is used as the electrolyte solution. All of analytical grade and used without further purification.

2.2 Synthesis of ACNF/$Cu_xMn_{1-x}Fe_2O_4$ composite nanostructures

ACNF/$Cu_xMn_{1-x}Fe_2O_4$ composite nanostructures were prepared by the electrospinning technique using a homogenous solution of polymer and metal sources. The polymer source was prepared by dissolving PAN 1.8 g in 25 ml of DMF solvent, whereas the metal source was obtained by mixing Cu, Mn and Fe nitrates (with molar ratio of x: $1-x$: 2, $x=0.0$, 0.2, 0.4, 0.6 and 0.8) in DMF solvent. Both sources were mixed thoroughly with a magnetic stirrer for 120 min, followed by sonication for 60 min. The precursor solution was turned to nanofibers using our home-made electrospinning system under an applied voltage of 10 kV, a feeding rate of 0.35 ml/h, a distance from syringe nozzle to collector of 10 cm, and drum rotating at 500 rpm. After drying at 60 °C for 48 h, the as-spun fibers were stabilized at 250 °C for 4 h in air atmosphere to form a ladder structure by the dehydrogenation and cyclization process [24]. To get the CNF/$CuMnFe_2O_4$ composite nanostructures, the stabilized samples were carbonized at 750 °C for 1 h under flowing of mixed air and argon atmosphere (30:300 ml/min). In this process, the heteroatoms like nitrogen are eliminated and the aromatic structure grows [25]. After that, ACNF/$CuMnFe_2O_4$ samples were obtained via activation process at 800 °C for 30 min under CO_2 atmosphere (160 ml/min). In this process, CO_2 reacts with carbon according to $C+CO_2 \rightarrow 2CO$, removes some carbon from the fibers, develops porosity and thus enlarges surface area. A schematic diagram of the formation of ACNF/$CuMnFe_2O_4$ composite nanostructures is presented in Fig. 1.

2.3 Physical characterization

The structural elucidation of the prepared ACNF/$Cu_xMn_{1-x}Fe_2O_4$ nanostructures was carried out using X-ray diffraction technique (XRD, Bruker D2 advance) with a Cu-Kα radiation source ($\lambda=0.15406$ nm). The morphologies were observed by field emission scanning electron microscopy (FE-SEM, Carl Zeiss, Auriga). The oxidation state of metal atoms was conducted at X-ray photoemission spectroscopy and X-ray absorption spectroscopy station (XPS and

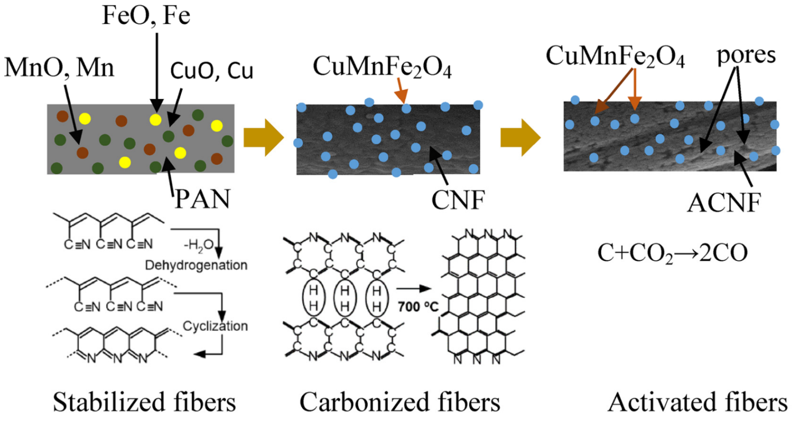

Fig. 1 Schematic diagram of the heat treatment process for ACNF/$Cu_xMn_{1-x}Fe_2O_4$ composite nanostructures

Table 1 Lists of specific capacitance (C_s), crystallite size (D), d-spacing (d), lattice constant (a), electrolyte resistance (R_s), charge transfer resistance (R_{ct}), the percentage of humidity, carbon, and $CuMnFe_2O_4$, respectively

Sample	C_s (F/g)		D (nm)	d (Å)	a (nm)	R_s (Ω)	R_{ct} (Ω)	Humidity (%)	Carbon (%)	$CuMnFe_2O_4$ (%)
	CV (2 mV/s)	GCD (2A/g)								
$X=0.0$	175	147.0	27.35	2.5102	0.4602	0.777	0.028	3.5	78.0	18.5
$X=0.2$	384	313.9	37.52	2.5397	0.4656	0.854	0.033	0.5	42.3	57.2
$X=0.4$	140	122.9	48.28	2.5350	0.4647	0.955	0.039	1.8	35.9	62.3
$X=0.6$	144	160.3	43.53	2.5304	0.4639	0.952	0.036	3.1	38.8	58.1
$X=0.8$	235	171.7	35.7	2.5151	0.4611	0.938	0.035	2.8	48.8	48.4

XAS, BL5.2, 1.2 GeV, bending magnet) at SLRI, Thailand. The surface area was obtained using the Brunauer-Emmett-Teller analyzer (BEL SORP MINI II, JAPAN). To estimate the weight percentage of residual carbon and $CuMnFe_2O_4$ in the composite nanostructure, the thermal gravimetric analyzer (TGA/DSC, NETZSCH STA 449F3, Germany) was used.

2.4 Electrochemical characterization

The electrochemical performance was performed using cyclic voltammetry (CV), galvanic static charge discharge (GCD) and electrochemical impedance spectroscopy (EIS) techniques on a PGSTAT 302N (Auto lab, The Netherlands). Three electrodes configuration consisting of working electrode (WE), counter electrode (CE) and reference electrode (RE) was used in 2.0 M KOH aqueous solution. The WE electrode was prepared by mixing an active sample with acetylene black (conductive agent) and polyvinylidene difluoride (binder) with a weight ratio of 8:1:1 in DMF solvent. The mixed precursor in a slurry produced by sonicating for 60 min was dropped onto the 1 cm^2 Ni foam and then dried at 70 °C on a hot plate. A platinum (Pt) wire and silver/silver chloride (Ag/AgCl) were used as CE and RE electrodes, respectively. The CV measurements were carried out at different scan rates ranging from 2 to 200 mV/s. The charge/discharge between the selected potential windows was measured with a current density of 2 A/g, while EIS spectra were taken over a frequency range of 100 kHz to 0.01 Hz.

3 Result and discussion

The XRD diffraction patterns of ACNF/$Cu_xMn_{1-x}Fe_2O_4$ composite nanostructure are shown in Fig. 2. The peaks at 2θ values of 18.35°, 30.10°, 35.31°, 36.93°, 42.96°, 53.30°, 56.70° and 62.20° can be indexed to (111), (220), (311), (222), (400), (422), (511), and (440) crystal planes of $MnFe_2O_4$ (JCPDS No. 10–0319), while the peak at about 26° confirms the disorder nature of graphite [26] and can be indexed to (002) plane (JCPDS card no. 75-1621). After Cu decoration, three diffraction peaks near 44°, 52° and 75° corresponding to the (111), (200) and (220) planes of copper metal (JCPDS No. 85-1326) were observed. With the increasing of "x", the ferrite peak of (400) around 42° tended to be weak and even disappeared at $x=0.8$, whereas a new peak of Cu (111) was formed turned up and gradually strengthened. It is speculated that, when the copper oxide is reduced into copper metal during heat treatment process, the spinel structure of the $MnFe_2O_4$ was destroyed. Based on the Scherrer equation [27], the average crystallite size was found to be in the range of 27–48 nm and did not show any significant trend with "x" value. However, sample $x=0.2$ shows nearly the same size to sample $x=0.8$, while sample $x=0.4$ exhibits a similar size to sample $x=0.6$. The d-spacing values for all ACNF/$CuMnFe_2O_4$ system are slightly higher than those of ACNF/$MnFe_2O_4$ ($x=0$) and bulk cubic $MnFe_2O_4$ (2.4298 Å JCPDS 86-2267), possibly due to the effect of ACNF matrix and copper doping. The lattice constant showed slight increase after introducing cupper, suggesting the replacement of Mn^{2+} of radius 0.78 Å or Fe^{3+} 0.69 Å with larger ionic radius of 0.87 Å of Cu^{2+}. Lists of

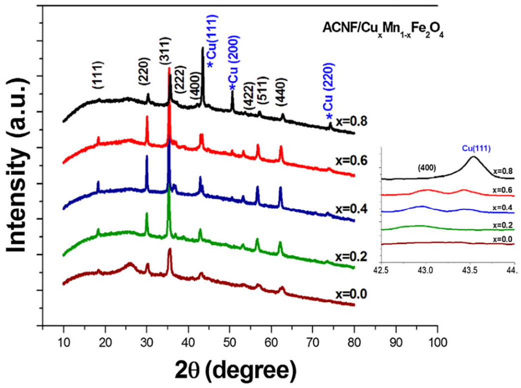

Fig. 2 XRD patterns of the ACNF/$Cu_xMn_{1-x}Fe_2O_4$ composite nanostructures

crystallite size, *d*-spacing and lattice constant are shown in Table 1.

Figure 3 shows FE-SEM images of the ACNF/$Cu_xMn_{1-x}Fe_2O_4$ composite nanostructure. All prepared samples exhibited porous surface arising from the activation process. With increase in “x” value, the roughness surface with more nanoparticles covered was observed. The fibers with diameters varied from 600 to 700 nm were observed for all samples and did not change much with the increase of “x” value. It is worth noting that the nanometer-scale diameter of prepared samples could provide a short ion diffusion distance, which would be beneficial to improve the electrochemical properties of prepared electrode [28].

Figure 4 shows the surface XPS analysis for C1s, Cu2p, Fe2p, and Mn2p of all ACNF/$Cu_xMn_{1-x}Fe_2O_4$ nanostructures. The binding energy peak at 284.9 eV for C1s indicating to C–C bond [29] was observed for all prepared samples (Fig. 4a). Two characteristic peaks of Cu($2p_{3/2}$) and Cu($2p_{1/2}$) at 932.3 and 952.3 eV, respectively (Fig. 4b), were attributed to the presence of the Cu^{2+} chemical state on the surface of samples [30]. The sample $x = 0.2$ shows the shake-up satellite peaks of the Cu($2p_{3/2}$) and Cu $2p_{1/2}$ at 942.5 and 962.6 eV, respectively, confirming the formation of Cu^{2+} on the surface [31]. Two main peaks at 710.9 and 724.5 eV are ascribed to the characteristic doublets of Fe$2p_{3/2}$ and Fe$2p_{1/2}$, respectively of Fe^{3+}. For the sample with $x = 0.2$, the satellite peak at 718.9 eV can be seen clearly and indicates that Fe is mainly in the Fe^{3+} state [32]. Two distinct peaks at binding energies of 642.2 and 653.6 eV attributed to the Mn (2p3/2) and Mn (2p1/2) of Mn^{2+} [33, 34] were clearly seen for first two samples with largest Mn content ($x = 0.0$ and $x = 0.2$). No shift of the Mn2p peaks was observed indicating that the fraction of each Mn ion state does not change noticeably with Cu addition.

To further verify the bulk oxidation state of Mn and Fe ion in $MnFe_2O_4$, the XANE spectra from XAS technique

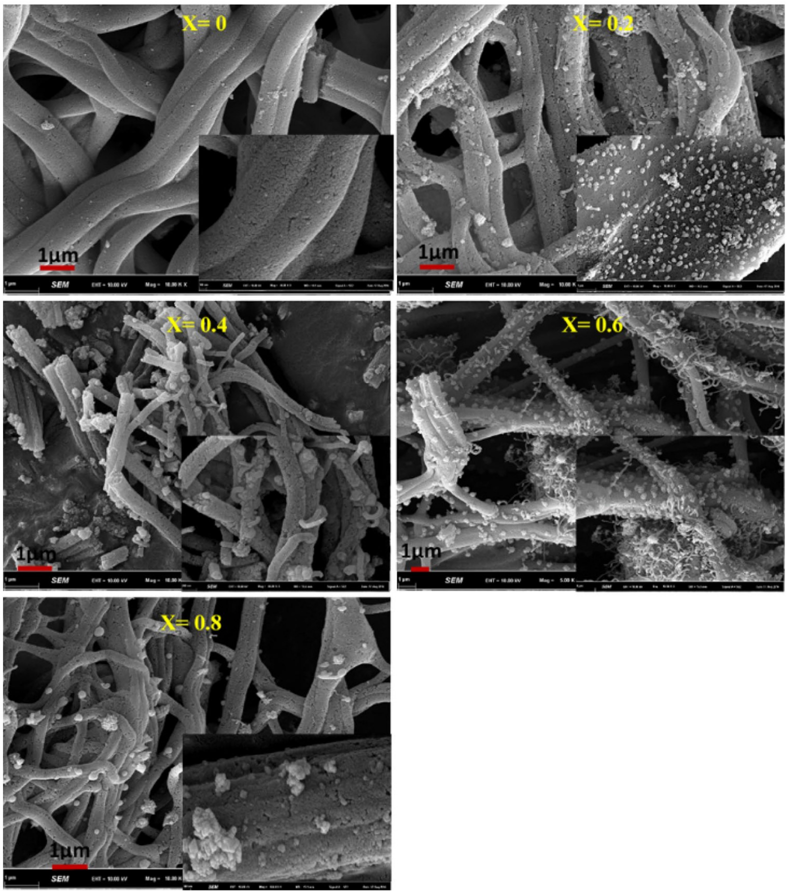

Fig. 3 FE-SEM micrographs of the ACNF/$Cu_xMn_{1-x}Fe_2O_4$ composite nanostructures

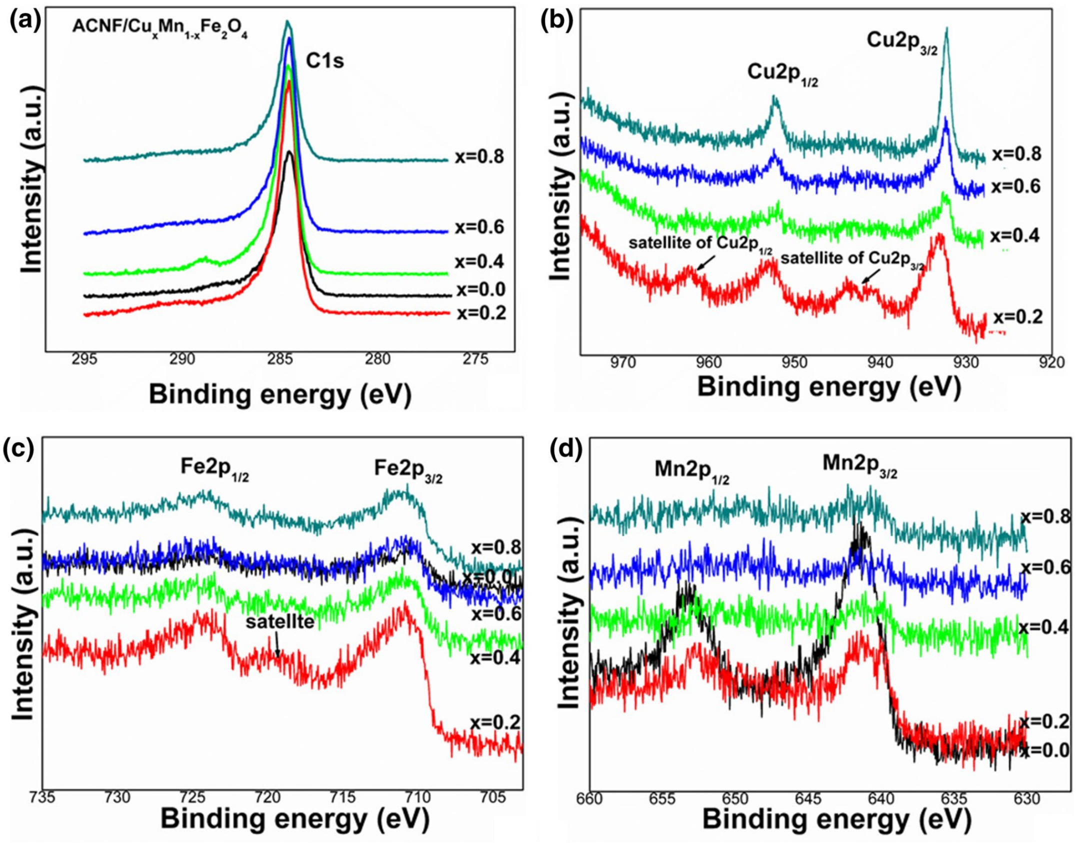

Fig. 4 XPS spectra of ACNF/$Cu_xMn_{1-x}Fe_2O_4$ composite nanostructures **a** C1s, **b** Cu2p, **c** Fe2p, **d** Mn2p, and **e** O1s

was used. Figure 5 shows the first derivative XANE spectra at Fe and Mn K-edge. It was found the the Fe K-edge spectra for all samples are similar to that of Fe_2O_3 indicating Fe^{3+}. Meanwhile the edge energies of Mn lay between MnO and Mn_2O_3 indicating mixing of $Mn^{2+,3+}$.

Figure 6 shows TG curves for ACNF/ $Cu_xMn_{1-x}Fe_2O_4$ composite nanostructures. All prepared samples show two main steps of weight loss at ~ 20–295 °C (minor) and ~ 295–570 °C (major). The minor weight loss corresponds to the loss of chemically absorbed water molecular and all trapped solvents. The major weight loss relates to the decomposition of metal nitrates along with the degradation of PAN polymer chain. The common plateau was observed after that, suggesting the presence of only pure inorganic contents. The weight percentage of $Cu_xMn_{1-x}Fe_2O_4$ loading in the composite nanostructures was determined from the residue weight at 1000 °C. The values of 18.5, 57.2, 62.3, 58.1 and 48.4% were observed for samples $x = 0$, 0.2, 0.4, 0.6 and 0.8, respectively. The corresponding contents of carbon are 78, 42.3, 35.9, 38.8 and 48.8%, respectively. The samples $x = 0.2$ and 0.8 show nearly content of carbon and $CuMnFe_2O_4$ as those of samples with $x = 0.4$ and 0.6. As known, EDLC is the source of energy storage for carbonaceous materials, while pseudocapacitance is for metal oxide systems. Therefore, the appropriate proportion of residual content of carbon and $CuMnFe_2O_4$ may support high capacitance.

Figure 7 shows the adsorption/desorption isotherm for ACNF/$Cu_xMn_{1-x}Fe_2O_4$ composite nanostructures. All isotherms are similar to the IV-type with H3 hysteresis suggesting mesopores (2–50 nm). The mean pore diameter of 3–10 nm based on the BJH method was observed [35]. The corresponding specific surface area (a_{bet}), total pore volumes (V), peak radius of pores (R_p), and mean pore diameter are presented as inset figures. The specific surface area for all samples exhibits higher value than that of 30–190 m^2/g for

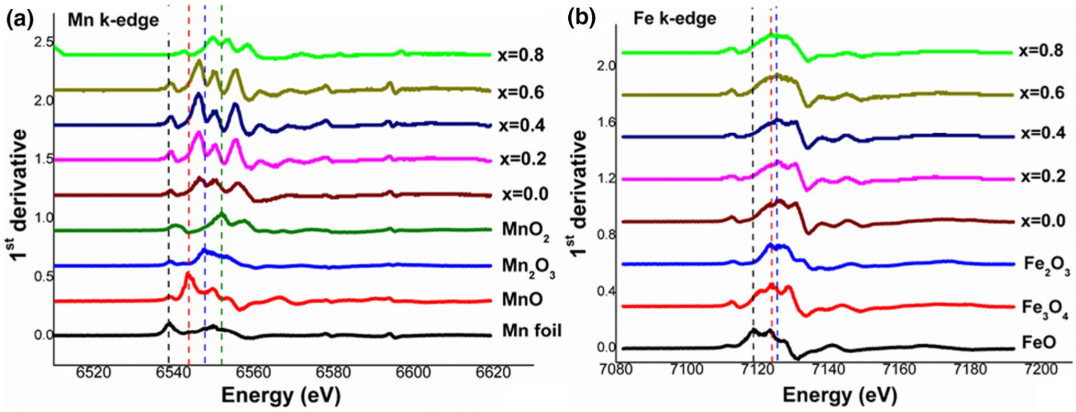

Fig. 5 The first derivative plots at Fe K-edge (**a**), and Mn K-edge (**b**)

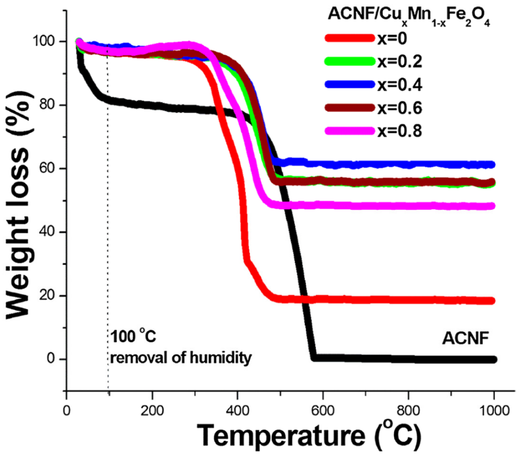

Fig. 6 TGA curves of CNF and ACNF/$Cu_xMn_{1-x}Fe_2O_4$ composite nanostructures

non-activated CNF in our previous work [15]. In electrochemical analysis, large surface provides high accessiblity of electrolyte ions and facilitates fast ions transfer between electrode and electrolyte, leading to a large capacity of the prepared electrode [36, 37].

The electrochemical performance of the ACNF/$Cu_xMn_{1-x}Fe_2O_4$ was first examined by cyclic voltammetry (CV) at different scan rates of 2–200 mV/s (Fig. 8a–e). It was found that the capacitive behavior was observed in the high potential range of − 1.2 to 0.1V. The voltammetry current is directly proportional to the scan rate and the redox humps are seen due to pseudo-capacitive behavior. The samples $x = 0.2$ and 0.8 sshow large anodic peak around − 0.5 to − 0.7V (at 2-200 mV/s). This peak refer to the oxidation of metallic Cu, Mn, and Fe to CuO, MnO and Fe_2O_4, respectively. The shift of peak to higher potentials with the increase of scan rate may be due to the rearrangement of $CuMnFe_2O_4$ structure [38]. The specific capacitance (C_s) from CV was calculated according to the equation $C_s = \int IdV/mvV$ [39], where I is the current density, V is the potential, v is the scan rate potential, and m is the active mass. The obtained capacitance values decreased with an increase of a scan rate (Fig. 8f) suggesting the inaccessibility of electrolyte ions into surface of electrode at high charging/discharging rate [40]. At a scan rate of 2 mV/s, the C_s values of 175, 384, 140, 144 and 235 F/g were observed for samples $x = 0.0$, 0.2, 0.4, 0.6 and 0.8, respectively. The first two maximum values observed in samples with $x = 0.2$ and 0.8 correspond to their sharp redox peaks, which may be attributed to the insertion/de-insertion of electrolyte ions into their composite layered structures.

For a further understanding of the conductivity and interfacial charge transfer process at the electrode/electrolyte interface, the electrochemical impedance spectroscopy technique (EIS) was employed. Nyquist plots for ACNF/$Cu_xMn_{1-x}Fe_2O_4$ electrodes in 2 M KOH electrolyte are shown in Fig. 9a. All electrodes show almost a straight line at low frequency with a small semicircle arc in the high frequency region. The sloping line in the low frequency region represented the frequency dependence of ion diffusion into the bulk of the electrode. The diameter of semicircle in the high frequency region represents charge transfer resistance (R_{ct}), greater the diameter manifesting low electrical conductivity. The R_{ct} values of 0.028, 0.033, 0.039, 0.036 and 0.035 Ω were observed for samples $x = 0.0$, 0.2, 0.4, 0.6 and 0.8, respectively. The values are closely similar to others reported in $MnCuFe_2O_4$/rGO [33] and become smaller

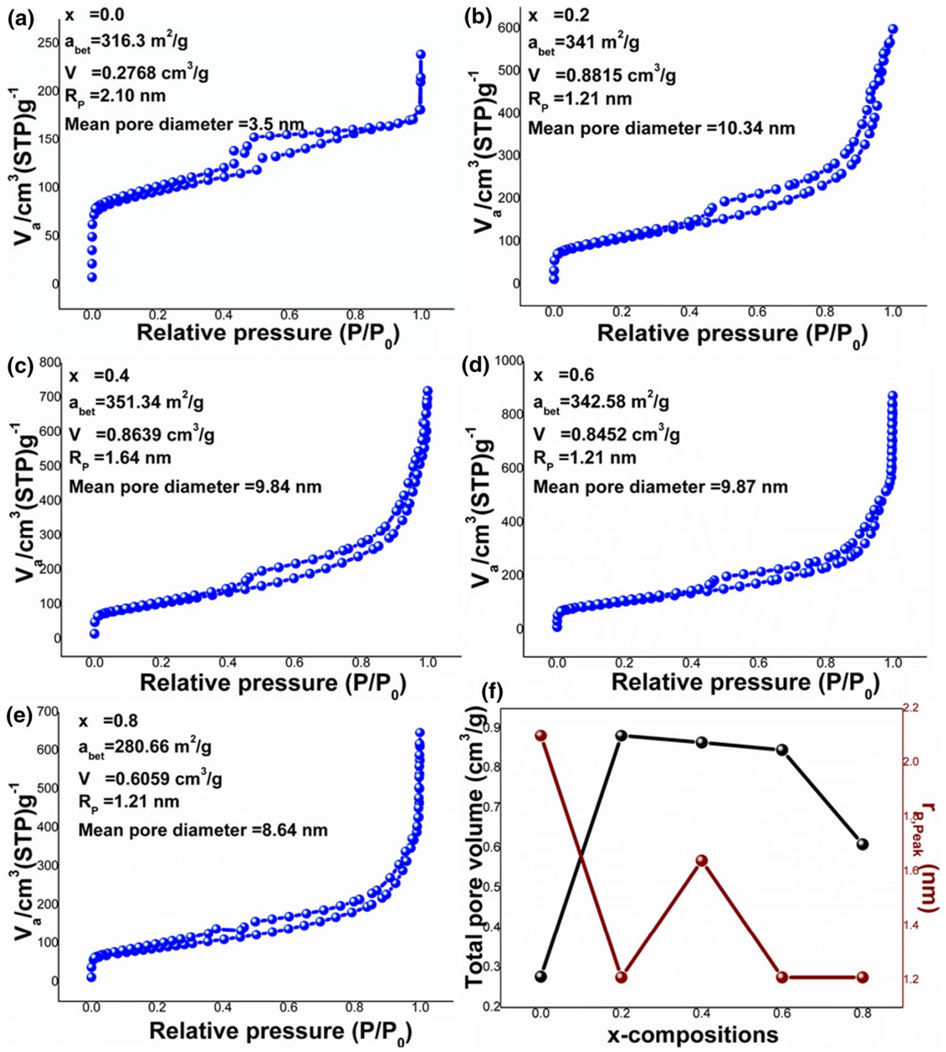

Fig. 7 **a–e** Adsorption–desorption isotherm and **f** the corresponding pore volume and peak radius porosity

compared with ACNF [41]. The real axis intercept represents the bulk solution resistance (R_s) [42, 43]. Low values of 0.777, 0.854, 0.955, 0.952 and 0.938 Ω were obtained for the sample $x = 0.0$, 0.2, 0.4, 0.6 and 0.8, respectively. The enhancement of both resistance values after introducing of Cu is possibly due to the rougher surface causing the enlarged contact area and aggregation of the nanoparticles that may block the penetration of electrolyte ions. The samples $x = 0.2$ and 0.8 show lower R_s and R_{ct} values than those of samples x = 0.4 and 0.6, indicating better conductivity. Figure 9b displays the Bode plots of frequency dependence of phase angle during 0.01–10^5 Hz. The phase angle decreases and close to zero with increasing of frequency. At frequency of 0.01 Hz, the phase angles of 72.93, 64.18, 73.60, 74.59, and 71.83 were obtained for $x = 0.0$, 0.2, 0.4, 0.6 and 0.8 electrodes, respectively. All values are not close to 90° for ideal capacitors. The low phase angle values for the samples with $x = 0.2$ and $x = 0.8$ as compared to the other are an indication of more pseudocapacitive behavior [44]. The capacitor response frequencies at phase angle of 45 °C for $x = 0.0$, 0.2, 0.4, 0.6 and 0.8 electrodes are 0.64, 0.71, 1.39, 1.54, and 1.07 Hz, respectively. The corresponding

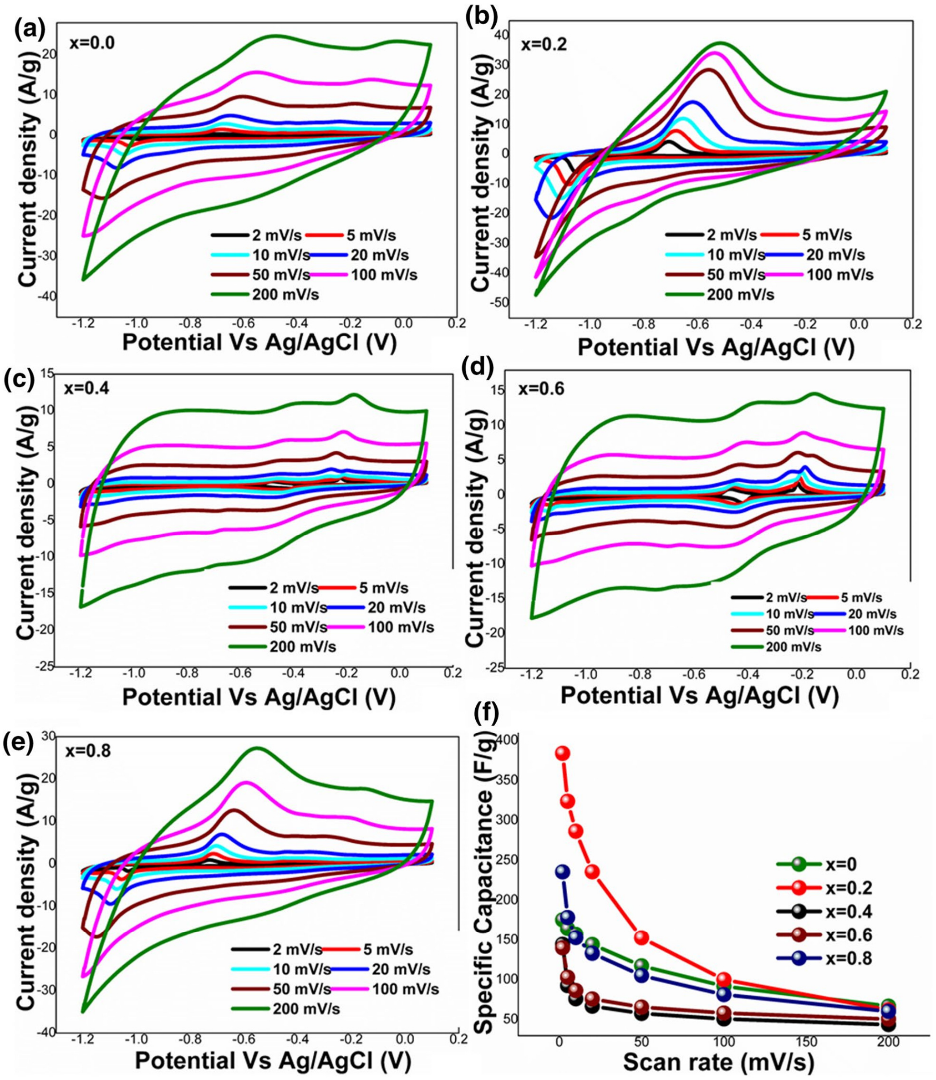

Fig. 8 **a–e** CV curve at scan rate of 2–200 mV/s, and **f** the corresponding specific capacitance as function of scan rate

relaxation time constant ($\tau_o = 1/f_o$) was calculated to be about 1.56, 1.41, 0.72, 0.65 and 0.93 s, respectively. The lower time constant of copper doping electrodes than that of the sample $x = 0$ supported faster charge–discharge [45]. Figure 9c shows galvanostatic charge/discharge (GCD) curves at a current density of 2 A/g. The nonlinear discharge curves indicate the capacitive behavior of prepared samples [46, 47]. The C_s value in F/g under the constant current discharge process was calculated based on the equation $C_s = It_d/mV$, where I is the current density, t_d is the discharge time and V is the voltage window. The samples $x = 0.2$ and 0.8 show higher C_s and energy density values than those of the samples $x = 0.4$ and 0.6 (Fig. 9d), which is consistent to the results already published elsewhere, i.e. $Ni_xMn_{1-x}Fe_2O_4$ films electrode [19] and $Ni_{1-x}Zn_xFe_2O_4$ [48]. To describe the electrochemical behavior, three parameters (surface area, conductivity and content of carbon and $CuMnFe_2O_4$) were considered. The conductivity is not directly measured in this work, but speculated from the Nyquist plot. It is worth noting from Table 1 that the C_s value does not depend directly

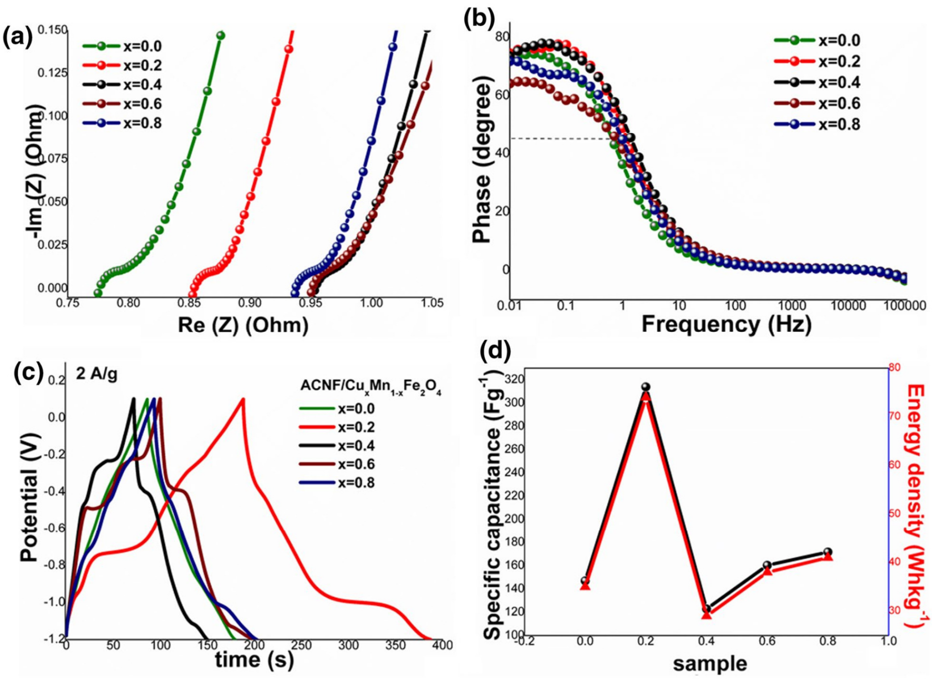

Fig. 9 **a** Nyquist plots at a frequency range of 0.01 Hz–100 kHz. **b** the corresponding Bode plots of frequency dependence of phase angle. **c** Galvanostatic charge/discharge spectra at 2 A/g. **d** The corresponding specific capacitance and energy density of ACNF/Cu$_x$Mn$_{1-x}$Fe$_2$O$_4$

on surface area, but seemed to depend on electrical conductivity and the residual amount of carbon and CuMnFe$_2$O$_4$. The samples with nearly proportional content between carbon and CuMnFe$_2$O$_4$ ($x = 0.2$ and $x = 0.8$) exhibit higher C_s values than those other samples. Such high C_s value may be attributed to the synergistic effects on charge storage mechanism between two components of composite materials. It was believed that the redox states for $x = 0.2$ and 0.8 might be higher than those of $x = 0.4$ and 0.6 and offer richer redox reactions, including contributions from all of Cu, Mn and Fe ions and thus maximizing surface charge accumulation.

Figure 10a shows plot of the capacitance retention after repeated CV at a scan rate of 100 mV/s over 1000 cycles. The values of 80.74, 77.98, 73.88, 75.00 and 80.26% were observed for $x = 0.0$, 0.2, 0.4, 0.6 and 0.8, respectively. The sample $x = 0$ shows the best cycling stability may due to its maximum carbon content (Table 1). In other words, carbon matrix may be working as elastic buffer structure and restricts the volume changes of electrode during charge/discharge process. The samples $x = 0.2$ and 0.8 (with 42.3 and 48.8% of carbon, respectively) also show better stability than $x = 0.4$ and 0.6 (with 35.9 and 38.8% of carbon, respectively). In addition, the variation trend of the capacity retention is almost opposite trend of the crystallite size (Fig. 10b). Larger crystallite size for $x = 0.4$ and 0.6 than those of $x = 0.2$ and 0.8 means smaller specific surface area and thus may suppress the interaction between the electrolyte ions and electrode. Moreover, large crystallite size may cause longer migration paths of electrolyte ions and thus reduce the capacity. Very small crystallite size (as $x = 0$) may imply more tortuous migration paths of electrolyte ions [49, 50], increase the resistance for ions insertion, and thus decrease the capacity. The moderate crystallite size for samples $x = 0.2$ and 0.8 improves the electrochemical performance. This observation is consistent with other studies of Li (Ni$_{0.5}$Co$_{0.2}$Mn$_{0.3}$)O$_2$ [51].

4 Conclusions

Activated carbon nanofibers composite with copper–manganese ferrite were fabricated by electrospinning followed by heat treatment process to observe the electrochemical properties. By varying molar content between copper and manganese precursor (ACNF/Cu$_x$Mn$_{1-x}$Fe$_2$O$_4$: $x = 0.0$, 0.2, 0.4, 0.6, 0.8), the cyclic stability strongly depends on the amount of carbon. The samples with $x = 0.2$ and 0.8 exhibit higher capacity than those of the samples with $x = 0.4$ and

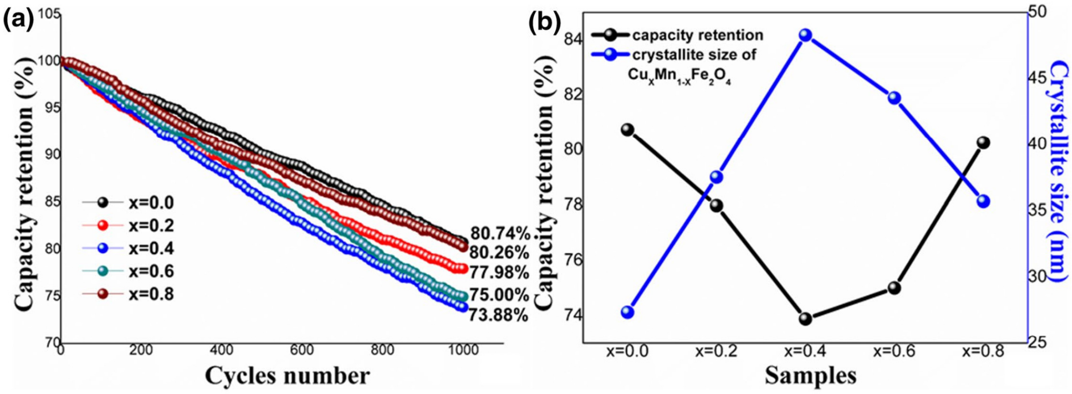

Fig. 10 the capacity retention at 1000 cycles (**a**) and the relationship between crystallite size and capacity retention

0.6. These two samples provided low resistivity, moderate and nearby crystallite size, and similarly residual content between $CuMnFe_2O_4$ and ACNF. Moreover, the superior capacitance may be attributed to the synergetic effect between pseudocapacitance of $CuMnFe_2O_4$ and EDLC of ACNF. The present work demonstrates an easy way to prepare high electrochemical performance of the polymer composite electrode.

Acknowledgements This work was supported by Thailand Research Fund and Synchrotron Light Research Institute (Public Organization) (TRF-SLRI) (Grant Number TRG5980001). The authors are thankful to the department of Applied Physics Rajamagala University of Technology Isan (RMUTI), the Advanced Material Physics Laboratory (AMP) at Suranaree University of Technology (SUT), for all facilities.

References

1. M. Winter, R.J. Brodd, Chem. Rev. **104**, 4245 (2004)
2. H.R. Ghenaatian, M.F. Mousavi, M.S. Rahmanifar, Synth. Met. **161**, 2017–2023 (2011)
3. L.L. Zhang, X.S. Zhao, Chem. Soc. Rev. **38**, 2520–2531 (2009)
4. J.P. Zheng, J. Electrochem. Soc. **152**, A1864–A1869 (2005)
5. H. Jiang, P.S. Lee, C. Li, Energy Environ. Sci. **6**, 41–53 (2013)
6. V. Gupta, N. Miura, Electrochem. Solid State Lett. **8**, A630 (2005)
7. H. Wang, Y. Wang, X. Wang, N. J. Chem. **37**, 869–872 (2013)
8. G.H. Yue, Y.C. Zhao, C.G. Wang, X.X. Zhang, X.Q. Zhang, Q.S. Xie, Electrochim. Acta **152**, 315–322 (2015)
9. K. Wang, X. Dong, C. Zhao, X. Qian, Y. Xu, Electrochim. Acta **152**, 433–442 (2015)
10. P.M. Kulal, D.P. Dubal, C.D. Lokhande, V.J. Fulari, J. Alloys Compd. **509**, 2567–2571 (2011)
11. D. Carta, M.F. Casula, A. Falqui, D. Loche, G. Mountjoy, C. Sangregorio, A. Corrias, J. Phys. Chem. C **113**, 8606–8615 (2009)
12. L. Wu, P.O. Jubert, D. Berman, W. Imaino, A. Nelson, H. Zhu, S. Zhang, S. Sun, Nano Lett. **14**, 3395–3399 (2014)
13. S. Nilmoung, P. Kidkhunthod, S. Pinitsoontorn, S. Rujirawat, R. Yimnirun, S. Maensiri, Appl. Phys. A. **119**(1), 141–154 (2015)
14. H. Zhu, S. Zhang, Y.X. Huang, L. Wu, S. Sun, Nano Lett. **13**, 2947–2951 (2013)
15. S. Nilmoung, T. Sinprachim, I. Kotutha, P. Kidkhunthod, R. Yimnirun, S. Rujirawat, S. Maensiri, J. Alloys Compd. **688**, 1131–1140 (2016)
16. S. Sun, H. Zeng, D.B. Robinson, S. Raoux, P.M. Rice, S.X. Wang, G. Li, J. Am. Chem. Soc. **126**(1), 273–279 (2004)
17. K. Vijaya Sankar, R. Kalai Selvan, J. Power Sources. **275**, 399–407 (2015)
18. S.F. Zhoua, X.J. Hana, H.L. Fanb, Q.X. Zhangc, Y.Q. Liua, Electrochim. Acta **174**, 1160–1166 (2015)
19. M.K. Zate, S.M. Shaikh, V.V. Jadhav, K.K. Tehare, S.S. Kolekar, R.S. Mane, M. Naushad, B.N. Pawar, K.N. Hui, J Anal Appl Pyrolysis. **116**, 177–182 (2015)
20. M. Taei, F. Hasanpour, F. Basiri, N. Tavakkoli, N. Rasouli, Microchem. J. **129**, 166–172 (2016)
21. B. Li, Y. Fu, H. Xia, X. Wang, Mater. Lett. **122**, 193–196 (2014)
22. Y. Sang, Y. Cui, Z. Li, W. Ye, H. Li, X.S. Zhao, P. Guo, Sens. Actuators B **234**, 46–52 (2016)
23. S.L. Kuo, N.L. Wu, J. Power Sources. **162**, 1437–1443 (2006)
24. M.S.A. Rahaman, A.F. Ismail, A. Mustafa, Polym. Degrad. Stab. **92**, 1421–1432 (2007)
25. D. Zhu, C. Xu, N. Nakura, M. Matsuo, Carbon **40**, 363–373 (2002)
26. W. Wang, P. Liu, M. Zhang, J. Hu, F. Xing, Open J. Compos. Mater. **2**, 104–112 (2012)
27. H.P. Klug, L.E. Alexander, *X-ray Diffraction Procedures for Polycrystalline and Amorphous Materials*, 2nd edn. (Wiley, New York, 1974)
28. M. Kunowsky, J.P. Marco-Lozar, A. Oya, A. Linares-Solano, Carbon. **50**, 1407 (2012)
29. J. Xiao, G. Xu, S.-G. Sun, S. Yang, Part. Part. Syst. Charact. **30**, 893–904 (2013)
30. G.H. Yue, Y. Zhang, X.Q. Zhang, C.G. Wang, Y.C. Zhao, D.L. Peng, Appl. Phys. A **118**, 763–767 (2015)
31. C.C. Chusuei, M.A. Brookshier, D.W. Goodman, Langmuir. **15**, 2806–2808 (1999)
32. D.D. Hawn, B.M. DeKoven, Surf. Interface Anal. **10**, 63 (1987)
33. X.Y. Longa, J.Y. Lia, D. Shenga, H.Z. Liana, Talanta. **166**, 36–45 (2017)
34. T. Simsek, S. Akansel, S. Ozcan, A. Ceylan, Ceram. Int. **40**, 7953–7956 (2014)

35. Y.W. Ju, G.R. Choi, H.R. Jung, W.J. Lee, Electrochim. Acta **53**, 5796 (2008)
36. H. Wang, Q. Gao, J. Hu, Microporous Mesoporous Mater. **131**, 89–96 (2010)
37. X.J. Zhu, Y.W. Zhu, S. Murali, M.D. Stoller, R.S. Ruoff, ACS Nano. **5**, 3333 (2011)
38. B. Bashir, W. Shaheen, M. Asghar, M.F. Warsi, M.A. Khan, S. Haider, I. Shakir, M. Shahid, J. Alloys Compd. **695**, 881–887 (2017)
39. B.E. Conway, *Electrochemical Supercapacitors: Scientific Fundamentals and Technological Applications*, (Plenum Press, New York, 1999)
40. J. Li, D.B. Le, P.P. Ferguson, J.R. Dahn, Electrochim. Acta **55**, 2991 (2010)
41. J.E. Yang, I. Jang, M. Kim, S.H. Baeck, S. Hwang, S.E. Shim, Electrochim. Acta **111**, 136–143 (2013)
42. V. Khomenko, E. Raymundo-Pinero, E. Frackowiak, F. Beguin, Appl. Phys. A. **82**, 567–573 (2006)
43. J.G. Wang, Y. Yang, Z.H. Huang, F. Kang, J. Power Sources. **204**, 236–243 (2012)
44. K. Krishnamoorthy, G. Veerasubramani, S. Radhakrishnan, S.J. Kim, Mater. Res. Bull. **50**, 499–502 (2014)
45. T.C. Girija, M.V. Sangaranarayanan, J. Power Sources. **156**, 705 (2006)
46. X. Yang, D. Wu, X. Chen, R. Fu, J. Phys. Chem. C **114**, 8581–8586 (2010)
47. X. Liu, L. Zhou, Y. Zhao, L. Bian, X. Feng, Q. Pu, ACS Appl. Mater. Interfaces. **5**, 10280–10287 (2013)
48. D.K. Pawar, S.M. Pawar, P.S. Patil, S.S. Kolekar, J. Alloys Compd. **509**, 3587–3591 (2011)
49. S.B. Waje, M. Hashim, W.D.W. Yusoff, Z. Abbas, Appl. Surf. Sci. **256**(10), 3122–3131 (2010)
50. A. Eftekhari, Microporous Mesoporous Mater. **243**, 355–369 (2017)
51. G. Fan, Y. Wen, B. Liu, W. Yang, J. Nanopart. Res. **20**, 43 (2018)

Materials Chemistry and Physics 220 (2018) 190–200

Contents lists available at ScienceDirect

Materials Chemistry and Physics

journal homepage: www.elsevier.com/locate/matchemphys

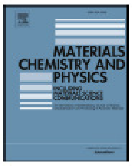

The structural and electrochemical properties of CNF/$MnFe_2O_4$ composite nanostructures for supercapacitors

Sukanya Nilmoung[a,*], Pinit Kidkhunthod[b], Santi Maensiri[c,d,e]

[a] Department of Applied Physics, Faculty of Sciences and Liberal Arts, Rajamangala University of Technology Isan, Nakhon Ratchasima 30000, Thailand
[b] Synchrotron Light Research Institute (Public Organization), 111 University Avenue, Muang District, Nakhon Ratchasima 30000, Thailand
[c] School of Physics, Institute of Science, Suranaree University of Technology, Nakhonratchasima 30000, Thailand
[d] NANOTEC-SUT Center of Excellence on Advanced Functional Nanomaterials, Suranaree University of Technology, Nakhonratchasima, Thailand
[e] SUT Center of Excellence on Advanced Functional Materials (AFM), Suranaree University of Technology, Nakhon Ratchasima 30000, Thailand

HIGHLIGHTS

- CNF/$MnFe_2O_4$ composite nanostructures have been successfully synthesized.
- Carbonization temperature influence the electrochemical performance.
- Higher carbonization temperature reduced equivalent series resistances.
- The existence of $MnFe_2O_4$ in carbon matrix reduced the stability of electrodes.

ARTICLE INFO

Keywords:
Carbon nanofibers composite
$MnFe_2O_4$
Spinel ferrites
Supercapacitors

ABSTRACT

This work report the structural, morphological and electrochemical properties of carbon nanofibers composited with manganese ferrite (CNF/$MnFe_2O_4$) for supercapacitors. The obtained samples were characterized by means of X-ray diffraction (XRD), field emission scanning electron microscopy (FE-SEM), Brunauer-Emmett-Teller analyzer (BET), thermal gravimetric analysis (TGA), X-ray photoemission spectroscopy (XPS) and X-ray absorption spectroscopy (XAS). The electrochemical properties were investigated using cyclic voltammetry (CV), galvanostatic charge-discharge (GCD), and electrochemical impedance spectroscopy (EIS). By increasing the carbonization temperature from 500 to 700 °C, the local structure of $MnFe_2O_4$ was found to be partial inverted spinel ferrite with oxidation state of Fe^{3+} and Mn^{2+}. The crystallite size, surface area, residual content of $MnFe_2O_4$, and fraction of Mn ions in tetrahedral site increased with increasing of carbonization temperature. The benefits of sample with maximum surface area, largest crystallite size, highest residual content of $MnFe_2O_4$ and high fraction of Mn^{2+} in tetrahedral site leading to enhanced energy storage. The maximum specific capacitance of 345 Fg^{-1} at 2 mVs^{-1} (using CV) and 291.87 Fg^{-1} at 5 Ag^{-1} (using GCD) were observed. The fascinating electrochemical properties of CNF/$MnFe_2O_4$ composite nanostrucutre makes it a potential candidate for high performance energy storage devices.

1. Introduction

Supercapacitors (SCs) are one of the most promising device for storage energy due to their high power density, fast charge/discharge rate and long cycling life [1–3]. According to charge storage mechanism, SC is classified into two types namely EDLC and pseudo-capacitors. EDLCs store energy by accumulating electrostatic charge at the electrode/electrolyte interface, while a pseudo-capacitor store charge through Faradaic with redox reaction. Nowadays, most of electrode material researches have been focusing on the development of transition metal oxides (V_2O_5 [4], NiO [5], Co_3O_4 [6], etc) because their redox reaction provides higher specific capacitance than those of EDLCs. Spinel ferrite (MFe_2O_4) is a metal oxide with spinel structure that consists of tetrahedral (A) and octahedral (B) sites for arrangements of cations ($[M_{1-i}Fe_i]^A[M_iFe_{2-i}]^BO_4$, where M is divalent transition metal, i is the inversion degree in between 0 and 1 (i = 0 is normal spinel (100% M in A-site), i = 1 is inverted spinel (100% M in B-site) and 0 < i < 1 is partially inverted spinel (M are in both A and B-site)). The cubic spinel ferrite unit cell is formed by 56 atoms, 32 oxygen anions distributed in a cubic close packed structure, and 24

---

[*] Corresponding author.
E-mail address: sukanya.ni@rmuti.ac.th (S. Nilmoung).

https://doi.org/10.1016/j.matchemphys.2018.08.084
Received 10 October 2017; Received in revised form 21 April 2018; Accepted 24 August 2018

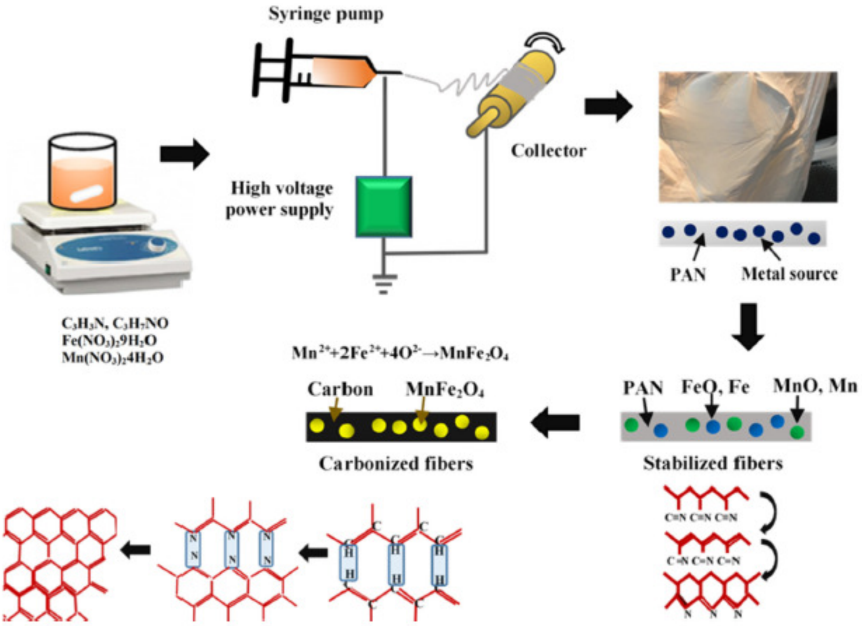

Fig. 1. Schematic diagram of the fabrication process and mechanism of the formation of CNF/$MnFe_2O_4$ composite nanostructures.

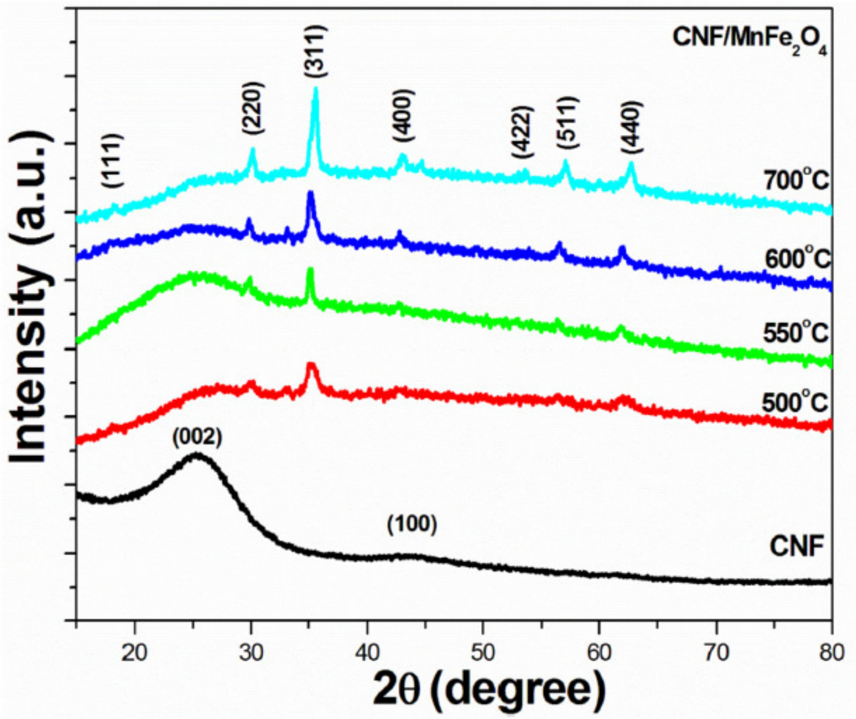

Fig. 2. XRD patterns of CNF and CNF/$MnFe_2O_4$ composite nanostructure carbonized at 500–700 °C.

Table 1
Summary of crystallite size, lattice constant, d-spacing, mean pore diameter, total pore volume and surface area of CNF/$MnFe_2O_4$ composite nanostructures carbonized at 500–700 °C.

samples	Crystallite size (nm)	Lattice constant (Å)	d-spacing (Å)	Mean pore diameter (nm)	Total pore volume (cm^3g^{-1})	Surface area (m^2g^{-1})
500 °C	12.93	4.685	2.5552	27.90	0.0826	11.84
550 °C	41.43	4.682	2.5536	20.44	0.1019	19.93
600 °C	46.00	4.674	2.5497	15.97	0.1533	38.38
700 °C	68.90	4.622	2.5213	7.47	0.4474	239.4

cations occupying 8 of the 64 available A-sites and 16 of the 32 available B-sites [7]. Previous studies on spinel ferrites focused intensively on their magnetic properties due to the unpaired electron spins of Fe^{2+} in B-sites strongly affected to the different magnetic properties [8,9]. Recently, many studies also focused on their electrochemical performance [10,11]. Among the various kinds of spinel ferrite, $MnFe_2O_4$ represent one of the most interesting in the electrochemical study for energy storage devices due to its high pseudocapacitance [12]. However, bare $MnFe_2O_4$ possess low electronic conductivities and less cycling stability limits their application in commercial. To overcome these drawbacks, various carbon-based active materials MWCNT [13], CB [14], Graphene [15], etc.) are widely used to incorporate into $MnFe_2O_4$. CNF is a carbonaceous materials that have been widely interested to composite with $MnFe_2O_4$ due to their conductive additives, and can serve as active sites for reactions. Moreover, CNF can easily fabricate by electrospinning, which is a simple and convenient technique for fabricating polymer fibers with diameters of nanometers [16]. The confining dimensions of nanomaterials enlarge their potential applications in energy storage [17,18].

In the present work, the synthesis of CNF/$MnFe_2O_4$ composite nanostructure was reported. The influences of carbonization temperatures
on the atomic structures, surface area, residual content, and capacit
behavior of CNF/$MnFe_2O_4$ were studied. To describe how the cat
arrangement within the spinel structure of $MnFe_2O_4$ affected to
electrochemical properties, the extended X-ray absorption fine str
ture (EXAFS) fitting was performed.

2. Experiments

2.1. Materials

In this work, Polyacrylonitrile (PAN, MW 150,000, Sigma-Aldric
N,N-dimethylformamide anhydrous (DMF, 99.8%, SIAL), Mangan
(II) nitrate hydrate (99.99%, Aldrich), and iron (III) nitrate nano
drate [99.9%, Kento] are of analytical grade and were used as precur
materials without further purification.

2.2. Synthesis of CNF/$MnFe_2O_4$ composite nanostructures

In brief of materials preparation, 1.8 g of PAN powders in 25 ml
DMF solvent was used as polymer source, whereas Mn and Fe nitr
with molar ratio of 1:2 in 5 mL of DMF was used as metal source. B
sources precursor were mixed thoroughly by stirring overnight,
lowed by sonication for 1 h for solubility. The electrospun of C
$MnFe_2O_4$ was obtained by using our home-made electrospinning syst
under an applied voltage of 10 kV, a feeding rate of 0.5 mlh^{-1}, a
tance from syringe nozzle to collector of 10 cm, and drum rotating
700 rpm. After dried at 60 °C for 48 h in vacuum, the electrospuns w
stabilized at 250 °C for 4 h in air atmosphere to prevent the fibers fr
fusing during final heat treatment. In this process, a ladder structur
C-N bond rings by the dehydrogenation and cyclization process. Fina
the stabilized fibers were carbonized at 500, 550, 600 and 700 °C
mixed of air and argon atmosphere to obtain CNF/$MnFe_2O_4$ compo
nanostructures. In this process, the heteroatoms like nitrogen
eliminated and the aromatic structure grows. A schematic diagram

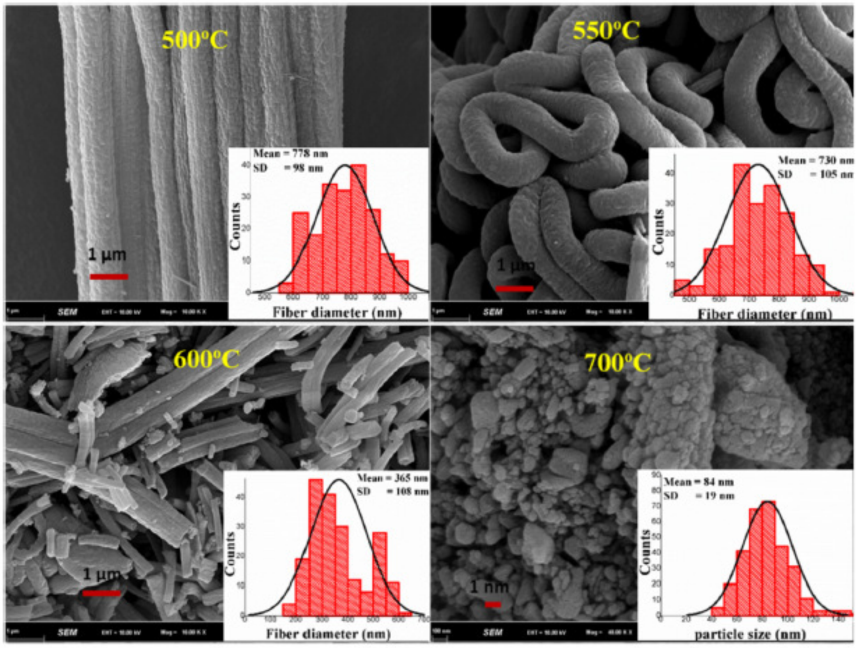

Fig. 3. FE-SEM images of the CNF/$MnFe_2O_4$ composite nanostructure carbonized at 500–700 °C.

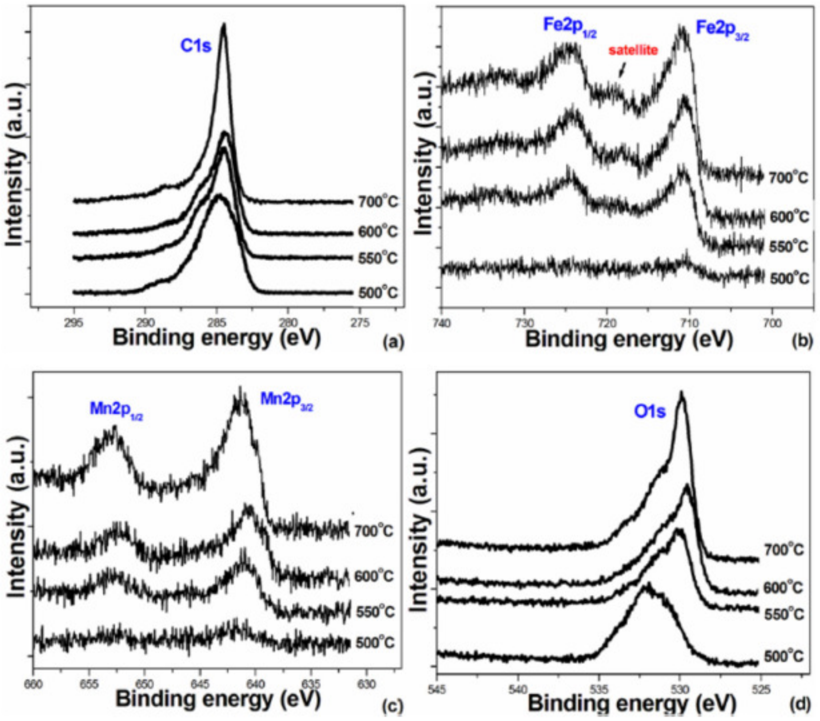

Fig. 4. XPS spectra for all CNF/$MnFe_2O_4$ composite nanostructure at (a) C1s, (b) Fe2p (c) Mn2p and (d) O1s.

the formation of CNF/$MnFe_2O_4$ composite nanostructures are presented in Fig. 1.

2.3. Physical characterization

The crystal structure of CNF/$MnFe_2O_4$ nanostructures was identified using X-ray diffraction (XRD, Bruker D2 advance) with a Cu-Kα radiation source ($\lambda = 0.15406$ nm). The morphological was examined by field emission scanning electron microscopy (FE-SEM, Carl Zeiss, Auriga). The oxidation state of metal atoms at surface was conducted at X-ray photoemission spectroscopy station (XPS, BL5.2, 1.2 GeV, bending magnet, SLRI, Thailand). The caions distribution was studied by extended X-ray absorption fine structure (EXAFS) (BL5, XAS, 1.2 GeV, SLRI, Thailand). The surface area was obtained by Brunauer-Emmett-Teller method (BEL SORP MINI II, JAPAN). To estimate the residual content of carbon and manganese ferrite, the thermal gravimetric analyzer (TGA, METTLER TOLEDO STARe) was used.

2.4. Electrochemical measurements

To evaluate the electrochemical performance of prepared samples, cyclic voltammetry (CV), galvanic static charge/discharge (GCD), and electrochemical impedance spectroscopy (EIS) techniques were performed using an electrochemical tested system (PG STAT 302N, The Netherlands) with a three electrodes system in 2 M KOH electrolyte. A platinum wire was used as the counter electrode, while an Ag/AgCl was used as the reference electrode. The working electrode was prepared by coating a slurry containing active material, acetylene black polyvinylidene difluoride (with a weight ratio of 8:1:1) in DMF solvent on 1 cm^2 Ni foam. Coated samples were heat at 200 °C over 2 h to remove the polymer binder. The CV measurements were conducted from − 1.2 to 0.1 V with scan rates ranging from 2 to 200 mVs^{-1}. The galvanostatic charge/discharge between the selected potential windows was measured with a current density of 5 Ag^{-1}. The EIS measurement were performed by using the frequency range of 0.01–10^5 Hz.

3. Result and discussion

Fig. 2 shows the XRD pattern of CNF/$MnFe_2O_4$ nanostructures carbonized at 500, 550, 600 and 700 °C. After carbonization process, PAN nanofibers are converted into CNFs, while metal source is reduced to form manganese ferrite. The peaks at 2θ of 18.318°, 30.183°, 35.579°, 43.134°, 53.684°, 57.12°, and 62.789° are indexed to the (111), (220), (311), (400), (422), (511), and (440) planes, respectively, of face-centered cubic structure of $MnFe_2O_4$ in the standard data no. 10–0319. The diffraction peak (311) became narrower with increasing temperatures indicating the increase of crystallite size. Based on the Scherrer equation [19], the crystallite size are in the range of 13–69 nm. The corresponding lattice constant and d-spacing are slightly decreased with increase of carbonization temperature (Table 1). The broad peak at 25.2° and 42.6° corresponding to the graphitic crystallite planes of (002) and (100) in JCPDS card no. 75–1621, respectively [20].

Fig. 3 shows Fe-SEM images of CNF/$MnFe_2O_4$ composite nanostructures carbonized at different temperatures (500–700 °C). The increasing of carbonization temperature plays an important role to change morphology from nanofibers to nanoparticles. At low temperature of 500 and 550 °C (Fig. 3 (a)-(b)), the fibers revealed long, smooth and uniform in cross-section with the average diameter of

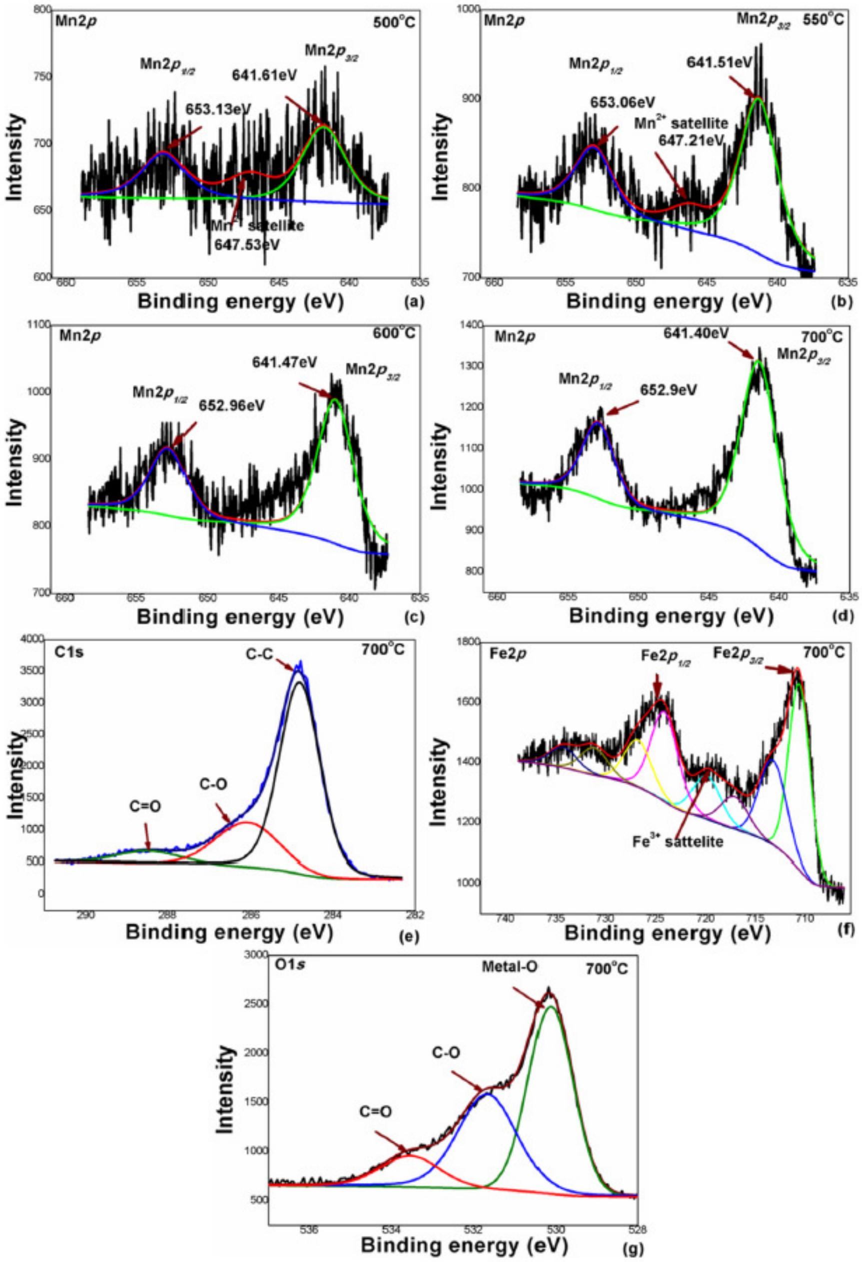

Fig. 5. Fitted XPS spectra of Mn2p for CNF/$MnFe_2O_4$ carbonized at 500, 550, 600 and 700 °C (a–d) and fitted XPS spectra of C1s, Fe2p, and O1s, respectively for CNF/$MnFe_2O_4$ carbonized at 700 °C (e–g).

~730 and 780 nm, respectively. The fibers became to shrink and fracture with diameter of ~360 nm at 600 °C (Fig. 3 (c)) and reduced to be particles with average size of 84 nm after being carbonized at 700 °C (Fig. 3 (d)). Normally, CNFs used in electrochemical cell have a diameter less than 1 μm [21]. It is expected that, small diameter of prepared samples offers shortens length for charge diffusion.

Fig. 4 represented the XPS spectra of C1s (a), Fe*2p* (b), Mn*2p* (c), and O*1s* (d) for all C/$MnFe_2O_4$ composite nanostructure. To describe the binding energy peaks, the spectra were fitted and some of them are presented in Fig. 5. All fitted data are listed in Table 2. The Mn*2p* spectra (Fig. 5(a–d)) show two main peaks at ~641 and ~653 eV, which are attributable to Mn*2p*3/2 and Mn*2p*1/2, respectively of Mn^{2+}

Table 2
XPS fitting data of C1s, Fe2p, Mn 2p and O1s of all CNF/$MnFe_2O_4$ composite nanostructures.

samples	C1s	Fe2p	Mn2p	O1s
500 °C	284.27 C-C	710.76	641.61	530.84 M-O[a]
	285.75 -C-O	724.13	653.13	531.93 C-O
	288.34 -C=O	(Fe^{3+})	(Mn^{2+})	533.38 C=O
550 °C	284.64 C-C	711.61	641.51	530.41 M-O[a]
	286.31 -C-O	724.26	653.06	531.61 C-O
	288.30 -C=O	(Fe^{3+})	(Mn^{2+})	533.46 C=O
600 °C	284.78 C-C	711.12	641.47	530.27 M-O[a]
	286.59 -C-O	725.32	652.96	531.46 C-O
	288.68 -C=O	(Fe^{3+})	(Mn^{2+})	533.38 C=O
700 °C	284.81 C-C	711.25	641.40	530.19 M-O[a]
	286.08 -C-O	723.7	652.90	531.67 C-O
	288.46 -C=O	(Fe^{3+})	(Mn^{2+})	533.55 C=O

[a] M is metal (Fe or Mn).

Table 3
Lists of coordinate number (N), amplitude reduction (So^2), and interatomic distances (R) from EXAFS fitting.

Sample	Shell	N	So^2	R(Å)	Shell	N	So^2	R(Å)
Mn K-edge_500 °C					Fe K-edge_500 °C			
A site	Mn-O	4	0.538	1.9276	Fe-O	4	0.445	1.8335
	Mn -Mn	6	0.538	3.1633	Fe -Mn	6	0.445	3.4475
	Mn -Fe	4	0.538	3.8417	Fe -Fe	4	0.445	3.6008
B site								
	Mn -O	6	0.462	2.1419	Fe -O	6	0.462	1.9916
	Mn -Fe	3	0.462	2.9014	Fe -Fe	6	0.462	3.3331
	Mn -Fe	6	0.462	3.3455	Fe -O	6	0.462	3.4921
Mn K-edge_550 °C					Fe K-edge_550 °C			
A site	Mn-O	4	0.573	1.9417	Fe -O	4	0.499	1.9507
	Mn -Mn	6	0.573	3.1895	Fe -Mn	6	0.499	3.6678
	Mn -Fe	4	0.573	4.0713	Fe -Fe	4	0.499	3.8309
B site								
	Mn -O	6	0.427	2.1311	Fe -O	6	0.487	2.0997
	Mn -Mn	3	0.427	3.0052	Fe -Mn	3	0.487	2.9968
	Mn -Fe	6	0.427	3.4229	Fe -Fe	6	0.487	3.5140
Mn K-edge_600 °C					Fe K-edge_600 °C			
A site	Mn-O	4	0.686	1.9321	Fe -O	4	0.520	1.9634
	Mn -Mn	6	0.686	3.5128	Fe -Mn	6	0.520	3.6916
	Mn -Fe	4	0.686	3.7653	Fe -Fe	4	0.520	3.8558
B site								
	Mn -O	6	0.314	2.1366	Fe -O	6	0.464	2.1338
	Mn -Fe	3	0.314	2.8883	Fe -Mn	3	0.464	3.0455
	Mn -Mn	3	0.314	3.0052	Fe -Fe	6	0.464	3.5711
Mn K-edge_700 °C					Fe K-edge_700 °C			
A site	Mn-O	4	0.707	1.9450	Fe -O	4	0.522	1.9573
	Mn -Mn	6	0.707	3.5134	Fe -Mn	6	0.522	3.6801
	Mn -Fe	6	0.707	3.6932	Fe -Fe	4	0.522	3.8438
B site								
	Mn -O	6	0.293	2.0970	Fe -O	6	0.485	2.1192
	Mn -Fe	3	0.293	2.8615	Fe -Mn	3	0.485	3.0246
	Mn -Mn	3	0.293	3.0052	Fe -Fe	6	0.485	3.5466

[22]. The separation between these two peaks of 11.52, 11.55, 11.49 and 11.52 eV were observed for the sample carbonized at 500, 550, 600 and 700 °C, respectively. The obtained values are approximately equal to 11.5 eV for Mn^{2+} [23]. Peak fitting of the C1s spectrum exhibits three main components arising from C–C (~284 eV), C–O (~286 eV) and C=O (~288 eV) bonds (Fig. 5 (e)) [24,25]. XPS fitted spectra of Fe2p were composed of multiple peaks (Fig. 5 (f)). Two main peaks at ~710 and ~725 eV are ascribed to the Fe2p3/2 and Fe2p1/2 of Fe^{3+}, respectively [26]. The distinct satellite peaks at about 8 eV above the main peak confirmed the presence of Fe^{3+} in the prepared samples [27,28]. Fig. 5 (g) shows three main peaks of O1s fitted spectra. The main peak at ~530 eV was attributed to the lattice oxygen of the metal oxides (Fe–O or Mn–O of $MnFe_2O_4$). The higher binding peak energy at ~532, and ~533 eV were compatible with the oxygen groups bonded with carbon atoms (C-O or C=O).

To further verify the cations distribution and local environment around the absorber in the spinel structure, the EXAFS spectra at Mn and Fe K-edge were fitted. The Fourier transform ($\chi(R)$) in R space and the $k^3\chi(k)$ weighted in k space from experiment (black line) and fit results (red dash) are shown in Fig. 6. The non-linear least square fitting data are given in Table 3. The $k\chi^3(k)$ values at both Mn and Fe K-edges (Fig. 6 (c) and (d)) are similar for all prepared samples, indicating similarity of the local environment around the absorber Mn and Fe ions.

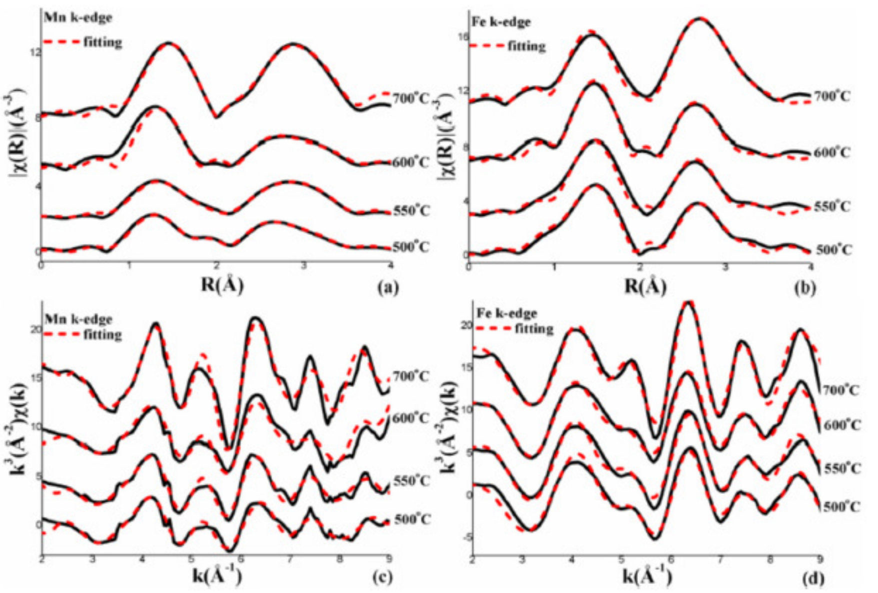

Fig. 6. Fourier transform at Mn and Fe K-edge (a, b), and the corresponding $k^3(\chi(k))$ plots (c, d) from experiment (solid line) and fitting (dash line).

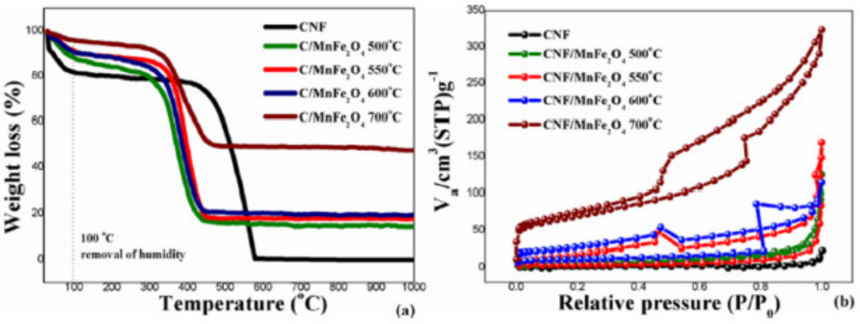

Fig. 7. (a) TGA curves and (b) adsorption-desorption isotherms of CNF/MnFe$_2$O$_4$ carbonized at 500–700 °C.

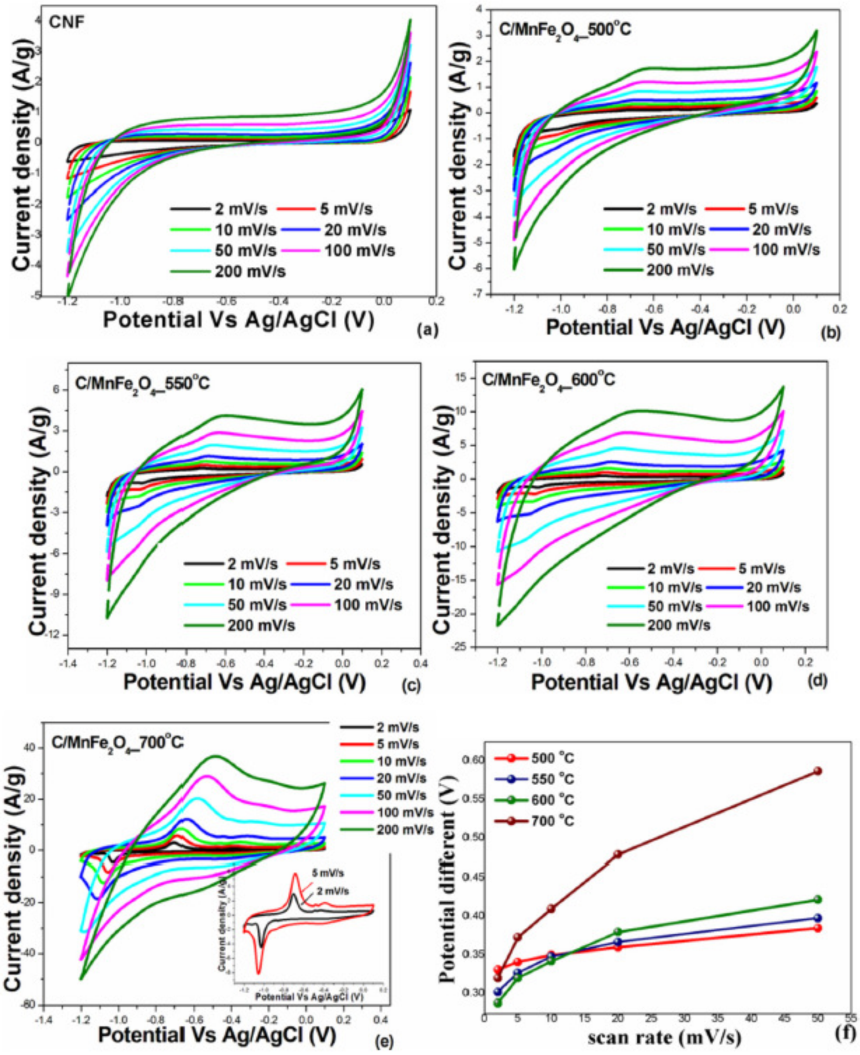

Fig. 8. (a–e) CV curves at various scan rate of 2–200 mVs^{-1} and (d) potential different of CNF/MnFe$_2$O$_4$ carbonization at 500–700 °C.

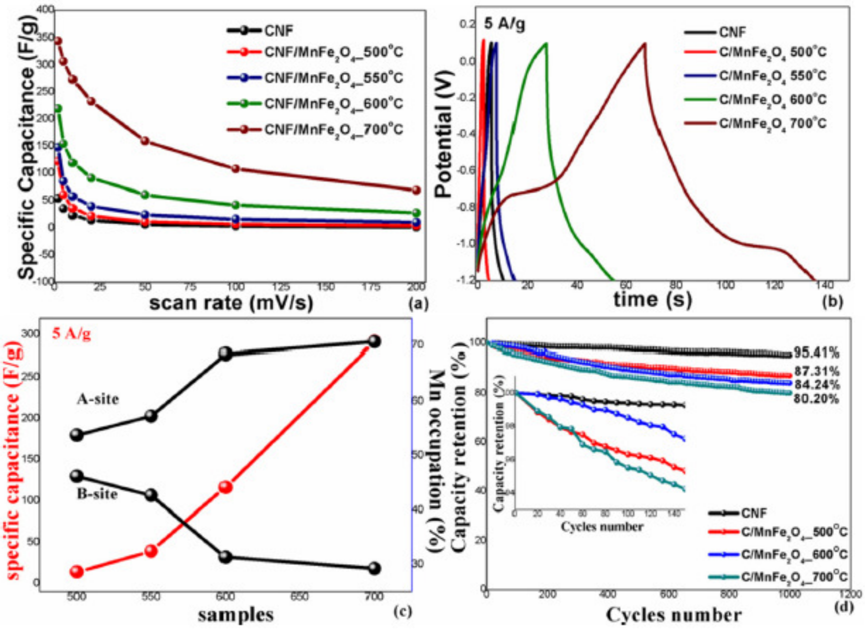

Fig. 9. (a) The specific capacitance as function of scan rate from CV (b) galvanostatic charge/discharge spectra at 5 Ag^{-1} (c) the discharge specific capacitance (red line) and the percentage of Mn occupied in A and B-sites (black line), and (d) the capacity retention at 1000 cycles.

The cations distribution can be explained by a degree of inversion between A and B-sites (as seem by S_0^2). Typically, in an inverse spinel the Mn^{2+} ions are all located in B-sites, while half of the Fe^{3+} ions preferentially occupy A-site and the rest fill B-sites [29]. According to the fitting data, all prepared samples exhibit partially inverse spinel structure that is both sites contain a fraction of Mn^{2+} and Fe^{3+} cations. The portion of Mn ions in A and B site of about 53.8 and 46.2%, 57.3 and 42.7%, 68.6 and 31.4%, and 70.7 and 29.3% were observed for CNF/$MnFe_2O_4$ carbonized at 500, 550, 600 and 700 °C, respectively. Interestingly, the higher carbonization temperature can switch Mn cations from B to A-sites. Moreover, the percentage of Mn in A-site at 700 °C very closely to previous report on bulk $MnFe_2O_4$ [30]. In the speinel ferrite structure, the substitution cations to change their valence state are critical for offering pseudocapacitance [31]. In our work, the distribution of Fe^{3+} ions in A and B sites are nearly similar proportion. So, the different distribution of Mn over A and B-site may leads to different electrochemical properties.

Fig. 7 (a) shows the weight loss spectra as a function of temperature for all C/$MnFe_2O_4$ composite nanostructure. The dramatic weight losses in the temperature range of 300–580 °C was related to the decomposition of metal nitrates along with the degradation of PAN polymer chain. The weight percentage of $MnFe_2O_4$ was determined from residue weight loss at 1000 °C. The value of 14.3, 17.8, 19.5 and 47.6% were observed for the samples 500, 550, 600 and 700 °C, respectively. The corresponding contents of carbon are 73.6%, 73.5%, 70.1% and 48.3%, respectively. As known that, EDLC is the source of energy storage for carbonaceous materials, while pseudocapacitance being for metal oxide systems. Therefore, high residual content of $MnFe_2O_4$ supporting pseudocapacitance. Fig. 7 (b) shows the adsorption and desorption isotherms for all prepared samples. The isotherms exhibit IUPAC type IV pattern, indicating the existence of mesoporous. It was found from Table 1 that the surface area and total pore volume increased with increasing of carbonization temperature, meanwhile the mean pore diameter decreased possibly due to the growth of crystallite size of $MnFe_2O_4$. The increasing of surface area supporting large number of reaction sites, resulting in an improved electrical double layer capacitance (EDLC).

To study the electrochemical properties of the prepared electrodes, the cyclic voltammetry (CV) was used. Fig. 8 shows CV curves over a wide voltage range of −1.2–0.1 V at various scan rates. The potential windows are slightly higher to the theoretical decomposition voltage of water (1.23 V). However, for the application of energy storage in aqueous supercapacitors, the operating voltage can be enlarged due to the existence of over-potential under the gas evolution. No any redox peaks were observed for pure CNF (Fig. 8 (a)), which is a characteristic of EDLC of carbon-based materials [32,33]. The composite electrodes (Fig. 8 (b)-(e)) show redox peaks implying to pseudo-capacitive behavior of $MnFe_2O_4$. The peaks in positive and negative current region known as anodic and cathodic peaks, respectively. Normally, the redox process of $MnFe_2O_4$ is described as the following equation [34].

$$MnFe_2O_4 + H_2O + 2e^- \leftrightarrow 4MnO + FeO + 2OH^- \tag{1}$$

Among all electrodes, C/$MnFe_2O_4$_700° has the largest capacitive area with sharpest peak (as inset of Fig. 8 (e)). At 2 mV/s, the sharp cathodic peak of −1.1 V might be due to the reduction of $MnFe_2O_4$ to metallic Mn and Fe, while the anodic peak appeared at about −0.7 V can be assigned to the oxidation of metallic Mn to MnO or Fe to Fe_2O_4. The potential separation between two peaks (ΔE_{pp}) increase with increasing of potential scan rate (Fig. 8 (f)) indicating their irreversible behavior. This may arise from the effect of resistance or the increase of over potentials [35]. According to CV spectra, the specific capacitances (Fg^{-1}) was evaluated via eqs. $Cs = \int IdV/mvV$ [36,37], where I is the current density, V is the potential, v is the scan rate potential, and m is the active mass. The obtained results are shown in Fig. 9 (a). It was found that, the C_S value decreased with increases of potential scan rate possibly due to insufficient time for accessible of the electrolyte ions into the inner pores or the gaps between the uniform nanoparticles [38]. Moreover, the C_S value at all scan rate increases with increasing of

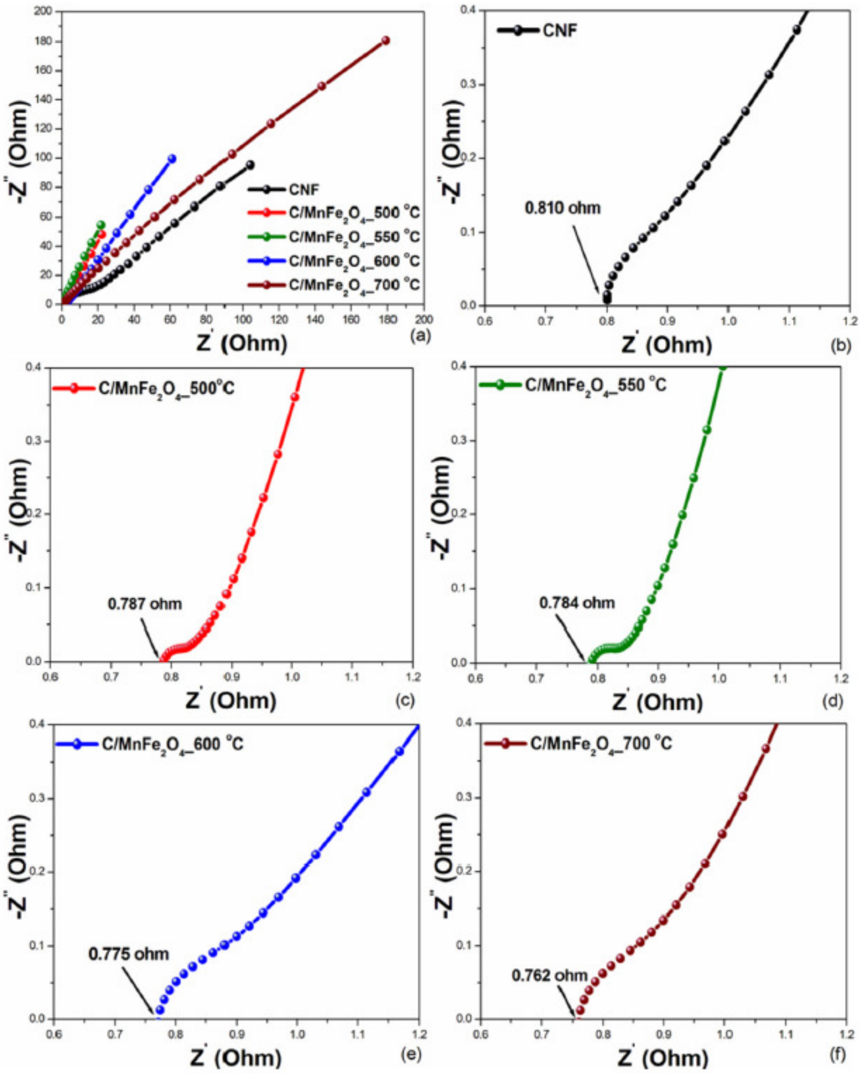

Fig. 10. Nyquist plots for CNF, C/MnFe$_2$O$_4$ carbonized at 500, 550, 600 and 700 °C (a) and their portion zooming at high frequency, respectively (b–f).

carbonization temperature. The maximum value is offered by the sample carbonized at 700 °C (345 Fg^{-1} at 2 mV/s), in which nearly consistent to 313 Fg^{-1} (at 5 mVs^{-1}) of MnFe$_2$O$_4$ thin film electrode in the same electrolyte [39]. The C$_S$ value was also evaluated from the constant current discharge technique at 5 Ag^{-1} (Fig. 9 (b)). The non-linear discharge curves indicate the capacitive behavior of prepared samples [40]. No voltage drop was observed, indicating fast I-V response and low internal resistance of prepared electrodes. The C$_S$ value can be obtained by eqs. $C_S = I\Delta t/m\Delta V$, where I is constant discharge current, t is discharge time, V is discharge voltage window, and m is the mass of active electrode material. It was found from Fig. 9 (c) that, the C$_S$ value increased with increasing of carbonization temperature, here also the same trend to previous reported [31]. The maximum C$_S$ value of 291.9 Fg^{-1} (at 5 Ag^{-1}) is nearly consistent to 293.5 Fg^{-1} (at 1 mAcm^{-2}) of MnFe$_2$O$_4$ thin film electrode [39]. High capacitance of CNF/MnFe$_2$O$_4$_700 °C possibly due to highest degree of graphitization [21,41], smallest fibers diameter, largest crystallite size, highest residual content of MnFe$_2$O$_4$, and maximum surface area of CNF. Moreover, it was found from Fig. 9 (c) that more Mn in A-sites leads to higher capacitance, indicating their dominant contribution. However, no systematic mechanistic investigation has been carried out and still cannot be clearly explained.

Fig. 9 (d) shows plot of the capacitance retention after repeated CV at a scan rate of 100 mV/s over 1000 cycles. The values of 95.41, 87.31, 84.24 and 80.20% were observed for CNF, C/MnFe$_2$O$_4$ carbonized at 500, 600, and 700 °C electrodes, respectively. All electrodes show over 80% indicating their long term cycling stability. The best cycle life of CNF electrode may due to the network structure restricts the change of electrode during charge/discharge process. The stability of C/MnFe$_2$O$_4$ electrodes drop significantly with increasing of carbonization temperature. Such behavior mainly attributed to either the decreasing of CNF working as elastic buffer or redox reaction arising from $MnFe_2O_4$ nanoparticles caused damage the structure. Moreover, it was found from the Nyquist plot (Fig. 10) that, the length spectra at low frequency for C/$MnFe_2O_4$ carbonized at 500 °C is shorter than those of 600 °C and 700 °C, respectively indicating the electrolyte ion just surface being accessed. As a consequence, low volume changes during charge/discharge caused long term cycling stability. The deeper penetrating of electrolyte ion through pores, cracks, inter-crystalline gap, etc. for C/$MnFe_2O_4$ carbonized at 600 °C and 700 °C, respective may leading to high volume changes caused short term cycling stability, respectively.

To understand the electrical behavior of prepared electrode, the EIS measurement were performed by using the frequency range of $0.01–10^5$ Hz. The Nyquist plots for all prepared electrodes are shown in Fig. 10. All curves having almost inclination of 45° with imaginary axis and is related to the frequency dependent diffusion resistance of electrolyte ions [42]. At high frequency region, the Nyquist plot of C/$MnFe_2O_4$ electrode carbonized at low temperature (500 and 550 °C) show a semicircle related to charge transfer resistance (R_{ct}). While, the semicircle diameter decrease almost vanish for the samples carbonized at higher temperature (600 and 700 °C) demonstrates the enhanced electrochemical behavior. The intercept at x-axis refer to the equivalent series resistances (R_s). The values of 0.810, 0.787, 0.784, 0.775 and 0.762 Ω were observed for CNF and the sample carbonized at 500, 550, 600 and 700 °C, respectively (Fig. 10 (b)-(f)). As expected, the R_s values were lower for higher carbonization temperatures samples, signifying the higher current density. The results confirm the electrochemical capacitive properties of the as synthesized electrode.

4. Conclusions

CNF/$MnFe_2O_4$ composite nanostructures were fabricated by electrospinning followed by carbonization process. The effect of carbonization temperature on the structural, morphological, and electrochemical properties were investigated. By varying the carbonization temperature (500–700 °C), the crystallite size, surface area, residual content of $MnFe_2O_4$, and Mn ions in A-site increased with increasing of carbonization temperature. These values reach a maximum at 700 °C, giving rise to a superior capacitance to those in others. The maximum C_S value of 345 Fg^{-1} at 2 mV/s (using CV scan) and 291.9 Fg^{-1} at 5 Ag^{-1} (using galvanostatic discharge) are achieved. The superior capacitance may arise from (i) the presence of the largest crystallite size appears dramatically to alter the surface area and electroconductivity (ii) the maximum surface area supported a large number of sites for electrolyte ions penetration, resulting in an improved EDLC (iii) the smallest size of prepared fibers offers shortens charge diffusion length for electrons/ions diffuse into the matrix of CNFs (iv) the highest residual content of $MnFe_2O_4$ offer high pseudocapacitance through Faradaic reactions (v) lower equivalent series resistances giving rise to higher current density. Moreover, the occupation of Mn cations in A-site may significant dominant contribution in determining the pseudocapacitive performance of $MnFe_2O_4$.

Acknowledgement

This work was supported by Thailand Research Fund and Synchrotron Light Research Institute (Public Organization) (TRF-SLRI) [grant number TRG5980001]. The authors are thankful to the department of Applied Physics Rajamagala University of Technology Isan (RMUTI), the Advanced Material Physics Laboratory (AMP) at Suranaree University of Technology (SUT), and the Center for Scientific and Technological Equipment, Suranaree University of Techanolgy, for all facilities.

References

[1] Y.Q. Zhao, M. Lu, P.Y. Tao, Y.J. Zhang, X.T. Gong, Z. Yang, G.Q. Zhang, H.L. Li, Hierarchically porous and heteroatom doped carbon derived from tobaccorods for supercapacitors, J. Power Sources 307 (2016) 391–400.

[2] X. Cui, R. Lv, R.U.R. Sagar, C. Liu, Z. Zhang, Reduced graphene oxide/carbon nanotube hybrid film as high performance negative electrode for supercapacitor, Electrochim. Acta 169 (2015) 342–350.

[3] G. Wang, L. Zhang, J. Zhang, A review of electrode materials for electrochemical supercapacitors, Chem. Soc. Rev. 41 (2012) 797–828.

[4] Y. Wei, C.W. Ryu, K.B. Kim, Improvement in electrochemical performance of V_2O_5 by Cu doping, J. Power Sources 165 (2007) 386–392.

[5] D. Han, P. Xu, X. Jing, J. Wang, P. Yang, Q. Shen, J. Liu, D. Song, Z. Gao, M. Zhang, Trisodium citrate assisted synthesis of hierarchical NiO nanospheres with improved supercapacitor performance, J. Power Sources 235 (2013) 45–53.

[6] Y. Xiao, C. Hu, M. Cao, High lithium storage capacity and rate capability achieved by mesoporous Co_3O_4 hierarchical nanobundles, J. Power Sources 247 (2014) 49–56.

[7] D. Carta, M.F. Casula, A. Falqui, D. Loche, G. Mountjoy, C. Sangregorio, A. Corrias, A structural and magnetic investigation of the inversion degree in ferrite nanocrystals MFe_2O_4 (M = Mn, Co, Ni), J. Phys. Chem. C 113 (2009) 8606–8615.

[8] L. Wu, P.O. Jubert, D. Berman, W. Imaino, A. Nelson, H. Zhu, S. Zhang, S. Sun, Monolayer assembly of ferromagnetic $Co_xFe_{3-x}O_4$ nanocubes for magnetic recording, Nano Lett. 14 (2014) 3395–3399.

[9] S. Nilmoung, P. Kidkhunthod, S. Pinitsoontorn, S. Rujirawat, R. Yimnirun, S. Maensiri, Fabrication, structure, and magnetic properties of electronspun carbon/cobalt (C/$CoFe_2O_4$) composite nanofibers, Appl. Phys. A 119 (1) (2015) 141–154.

[10] H. Zhu, S. Zhang, Y.X. Huang, L. Wu, S. Sun, Monodisperse $MxFe_{3-x}O4$ (M = Fe, Cu, Co, Mn) nanoparticles and their electrocatalysis for oxygen reduction reaction, Nano Lett. 13 (2013) 2947–2951.

[11] S. Nilmoung, T. Sinprachim, I. Kotutha, P. Kidkhunthod, R. Yimnirun, S. Rujirawat, S. Maensiri, Electrospun carbon/$CuFe_2O_4$ composite nanofibers with improved electrochemical energy storage performance, J. Alloy. Comp. 688 (2016) 1131–1140.

[12] S.L. Kuo, N.L. Wu, Electrochemical capacitor of $MnFe_2O_4$ with NaCl electrolyte, Electrochem. Solid State Lett. 8 (2005) A495–A499.

[13] M. Taei, F. Hasanpour, F. Basiri, N. Tavakkoli, N. Rasouli, Highly selective differential pulse voltammetric determination of warfarin in pharmaceutical and biological samples using $MnFe_2O_4$/MWCNT modified carbon paste electrode, Microchem. J. 129 (2016) 166–172.

[14] S.L. Kuo, N.L. Wu, Electrochemical characterization on $MnFe_2O_4$/carbon black composite aqueous supercapacitors, J. Power Sources 162 (2006) 1437–1443.

[15] B. Li, Y. Fu, H. Xia, X. Wang, High-performance asymmetric supercapacitors based on $MnFe_2O_4$/graphene nanocomposite as anode material, Mater. Lett. 122 (2014) 193–196.

[16] A. Frenot, I.S. Chronakis, Polymer nanofibers assembled by electrospinning, Curr. Opin. Colloid Interface Sci. 8 (2003) 64–75.

[17] J. Wu, N. Wang, Y. Zhao, L. Jiang, Electrospinning of multilevel structured functional micro-/nanofibers and their applications, J. Mater. Chem. A1 (2013) 7290–7305.

[18] P. Zhou, X. Yang, L. He, Z. Hao, W. Luo, B. Xiong, X. Xu, C. Niu, M. Yan, L. Mai, The Young's modulus of high-aspect-ratio carbon/carbon nanotube composite microcantilevers by experimental and modeling validation, Appl. Phys. Lett. 106 (2015) 111908.

[19] H.P. Klug, L.E. Alexander, X-ray Diffraction Procedures for Polycrystalline and Amorphous Materials, second ed., Wiley-Interscience, New York, 1974.

[20] W. Wang, P. Liu, M. Zhang, J. Hu, F. Xing, The pore structure of phosphoaluminate cement, Open J. Compos. Mater. 2 (2012) 104–112.

[21] B. Zhang, F. Kang, J.M. Tarascon, J.K. Kim, Recent advances in electrospun carbon nanofibers and their application in electrochemical energy storage, Prog. Mater. Sci. 76 (2016) 319–380.

[22] Y.J. Yao, Y.M. Cai, F. Lu, F.Y. Wei, X.Y. Wang, S.B. Wang, Magnetic recoverable $MnFe_2O_4$ and $MnFe_2O_4$ -graphene hybrid as heterogeneous catalysts of peroxymonosulfate activation for efficient degradation of aqueous organic pollutants, J. Hazard Mater. 270 (2014) 61–70.

[23] C.V. Ramana, M. Massot, C.M. Julien, XPS and Raman spectroscopic characterization of $LiMn_2O_4$ spinels, Surf. Interface Anal. 37 (4) (2005) 412–416.

[24] M. Zong, Y. Huang, H.W. Wu, Y. Zhao, S.Q. Wang, N. Zhang, W. Zhang, Facile synthesis of RGO/Fe_3O_4/Ag composite with high microwave absorption capacity, Mater. Lett. 111 (2013) 188–191.

[25] J. Xiao, G. Xu, S.G. Sun, S. Yang, MFe_2O_4 and MFe@Oxide core–shell nanoparticles anchored on N-doped graphene sheets for synergistically enhancing lithium storage performance and electrocatalytic activity for oxygen reduction reactions, Part. Part. Syst. Char. 30 (2013) 893–904.

[26] B.J. Li, H.Q. Cao, J. Shao, M.Z. Qu, Enhanced anode performances of the Fe_3O_4-Carbon-rGO three dimensional composite in lithium ion batteries, Chem. Commun. 47 (2011) 10374–10376.

[27] M. Vijayaraj, C.S. Gopinath, On the "Active spacer and stabilizer" role of Zn in $Cu_{1-x}Zn_xFe_2O_4$ in the selective mono-N-methylation of aniline: XPS and catalysis study, J. Catal. 241 (1) (2006) 83–95.

[28] D.D. Hawn, B.M. DeKoven, Deconvolution as a correction for photoelectron inelastic energy losses in the core level XPS spectra of iron oxides, Surf. Interface Anal. 10 (1987) 63.

[29] L.L. Hench, J.K. West, Principles of Electronic Ceramics, John Wiley and Sons, New

York, 1990.

[30] J.M. Hastings, L.M. Corliss, Neutron diffraction study of manganese ferrite, Phys. Rev. 104 (1956) 328.

[31] C. Wei, Z. Feng, M. Baisariyev, L. Yu, L. Zeng, T. Wu, H. Zhao, Y. Huang, M.J. Bedzyk, T. Sritharan, Z.J. Xu, Valence change ability and geometrical occupation of substitution cations determine the pseudocapacitance of spinel ferrite XFe_2O_4 (X = Mn, Co, Ni, Fe), Chem. Mater. 28 (2016) 4129–4133.

[32] Z.B. Wen, Q.T. Qu, Q. Gao, Z.H. Hu, Y.P. Wu, X.W. Zheng, Y.F. Liu, X.J. Wang, An activated carbon with high capacitance from carbonization of a resorcinolformaldehyde resin, Electrochem. Commun. 11 (2009) 715–718.

[33] Q.T. Qu, B. Wang, L.C. Yang, Y. Shi, S. Tian, Y.P. Wu, Electrochemical performance of MnO_2 nanorods in neutral aqueous electrolytes as a cathode for asymmetric supercapacoitors, Electrochem. Commun. 10 (2008) 1625–1655.

[34] B. Bashir, W. Shaheen, M. Asghar, M.F. Warsi, M.A. Khan, S. Haider, I. Shakir, M. Shahid, Copper doped manganese ferrites nanoparticles anchored on graphene nano-sheets for high performance energy storage applications, J. Alloy. Comp. 695 (2017) 881–887.

[35] W. Tang, L.L. Liu, Y.S. Zhu, H. Sun, Y.P. Wu, K. Zhu, An aqueous rechargeable lithium battery of excellent rate capability based on a nanocomposite of MoO_3 coated with PPy and $LiMn_2O_4$, Energy Environ. Sci. 5 (2012) 6909.

[36] B.E. Conway, Electrochemical Supercapacitors: Scientific Fundamentals and Technological Applications, Plenum Press, New York, 1999.

[37] C. Long, T. Wei, J. Yan, L. Jiang, Z. Fan, Supercapacitors based on graphene supported iron nanosheets as negative electrode materials, ACS Nano 7 (2013) 11325–11332.

[38] J. Li, D.B. Le, P.P. Ferguson, J.R. Dahn, Lithium polyacrylate as a binder for tin–cobalt–carbon negative electrodes in lithium-ion batteries, Electrochim. Acta 55 (2010) 2991.

[39] Manohar K. Zatea, Vijaykumar V. Jadhava, Shyam K. Gorea, Janardhan H. Shendkara, Satish U. Ekare, Ahmed Al-Ostaa Mu. Naushadc, Rajaram S. Mane, Structural, morphological and electrochemical supercapacitive properties of sprayed manganese ferrite thin film electrode, J. Anal. Appl. Pyrol. 122 (2016) 224–229.

[40] X. Liu, L. Zhou, Y. Zhao, L. Bian, X. Feng, Q. Pu, Hollow, spherical nitrogen-rich porous carbon shells obtained from a porous organic framework for the supercapacitor, ACS Appl. Mater. Interfaces 5 (2013) 10280–10287.

[41] B. Zhang, Y. Yu, Z.L. Xu, S. Abouali, M. Akbari, Y.B. He, F. Kang, J.K. Kim, Correlation between atomic structure and electrochemical performance of anodes made from electrospun carbon nanofiber films, Adv. Energy Mater. 4 (2014) 1301448.

[42] S.G. Khandalkar, H.M. Lee, H. Chae, C.K. Kim, Structural, morphological andelectrical characteristics of the electrodeposited cobalt oxide electrode for-supercapacitor applications, Mater. Res. Bull. 46 (2011) 48–51.